Considerations for In-Process Ultrasonic Phased Array Inspection and Monitoring of Fusion Welding Processes

Nina E. Sweeney

Department of Electronic and Electrical Engineering

University of Strathclyde

A thesis submitted for the degree of

Engineering Doctorate

December 2023

Copyright

This thesis is the result of the author's original research. It has been composed by the author and has not been previously submitted for examination which has led to the award of a degree.

Signed: 

Date: 15th December 2023

Acknowledgements

Throughout my academic career, I have received an incredible amount of support and encouragement. I would firstly like to thank my supervisor, Professor Charles MacLeod. I will be the first to say that I won the supervisor lottery. A more hard-working, considerate and supportive mentor would be hard to come by. I would also like to extend my gratitude to the wider team within the Search Lab, particularly Harris and Dave for their continued technical support and advice.

This work was funded by the Research Centre for Non-Destructive Evaluation (RCNDE) on behalf of PEAK NDT Ltd., through the Engineering and Physical Sciences Research Council (ESPRC) Centre for Doctoral Training in Future Innovation in Non-Destructive Evaluation (FIND CDT) (EP/S023275/1). I would like to thank both the staff and students within FIND CDT for creating such a supportive and collaborative organisation. I would also like to thank my industrial supervisor, Simon Parke, and the wider team at Peak NDT for recognising my abilities and continuing to support me in finding my niche between academia and industry.

I am always grateful for my small but loyal circle of friends, particularly Jackie and Claire. Thank you for making space for me within your mad little family when I needed it most.

I would be remiss if I did not acknowledge the canine and feline friends who have helped during this journey. I am convinced Gizmo and Ash have contributed more to this thesis through their keyboard wandering than I have done intentionally…

I am most thankful for my family, especially my father, Gordon. My confidant and long-suffering best friend. Thank you for teaching me the two most important lessons in life: perseverance and patience. (The welding came in handy too…)

Finally, for my late mother, Mary, because I would not be the person I am today if not for the time that we had, and the time that we lost.

Abstract

Welding is an integral part of manufacturing and plays an important role in many sectors such as transport, energy and defence. Recent global events including the Covid-19 pandemic and ongoing war in Ukraine have placed significant pressures and challenges on the global manufacturing sector. Furthermore, increased focus is being placed on a move towards net-zero operations in light of the climate crisis. Challenging environments are often catalysts for adaptation and innovation, which is exactly what has been seen within manufacturing sectors worldwide. Motivation to remain globally competitive within a changing global landscape has placed advanced manufacturing at the forefront of future investment plans.

Many industrial sectors employ Non-Destructive Evaluation (NDE) as a means of ensuring the integrity of welded components post-build and throughout their service life. In recent years there have been increasing economic and industrial drivers for the development of real-time NDE delivered at the point of manufacture. Real-time inspection and monitoring of welding processes can help to reduce fabrication costs by detecting defects as they occur, enabling more efficient and cost-effective builds whilst also supporting the assurance of asset integrity throughout the component life cycle.

This thesis presents significant advancements in the field of in-process ultrasonic inspection and monitoring of fusion welding processes. The challenges associated with deployment of ultrasonic NDE during fusion welding are non-trivial. Therefore, considerable research has been required to fully understand the extent of these challenges

and enable the development of techniques to address and overcome them. As a result, a system capable of ultrasonic phased array inspection during fusion welding has been realised to allow the detection of defects as they occur, thus reducing rework, repair time and helping to delivering high-quality welds right, first time. For the first time, phased array ultrasonic testing has been used to successfully interrogate the molten weld pool during deposition of gas tungsten arc welds, further reducing defect detection time. There is also significant opportunity to leverage this technique for in-process control of welding processes to prevent and reduce defect occurrence.

Contents

List of Figures

List of Tables

List of Acronyms

Acronym	Description
AVC	Arc Voltage Control
CAD	Computer Aided Design
CTWD	Contact Tip to Work Distance
DOF	Degree of Freedom
EBW	Electron Beam Welding
ECT	Eddy Current Testing
EDM	Electrical Discharge Machining
EMAT	Electromagnetic Acoustic Transducers
EMI	Electromagnetic Noise Interference
FE	Finite Element
FMC	Full Matrix Capture
FT	Force Torque
GMAW	Gas Metal Arc Welding
GTAW	Gas Tungsten Arc Welding
HAZ	Heat-Affected Zone
HDR	High Dynamic Range
HVM	High-Value Manufacturing
ID	Internal Diameter
IR	Infrared
LIPA	Laser Induced Phased Array
LOF	Lack of Fusion
LORF	Lack of Root Fusion
LORP	Lack of Root Penetration
LOSWF	Lack of Sidewall Fusion
LU	Laser Ultrasonics
MIG	Metal Inert Gas
MMA	Manual Metal Arc
MT	Magnetic Particle Testing
NDE	Non-Destructive Evaluation
NDT	Non-Destructive Testing
OD	Outer Diameter
PAUT	Phased Array Ultrasonic Testing
PAW	Plasma Arc Welding
PCS	Probe Centre Separation

PT	Penetrant Testing
PZT	Lead Zirconate Titanate
ROI	Region of Interest
RT	Radiographic Testing
RW	Resistance Welding
Rx	Receiver
SAW	Submerged Arc Welding
SDH	Side-Drilled Hole
SMAW	Shielded Metal Arc Welding
SNR	Signal-to-Noise Ratio
SS	Steady State
TFM	Total Focusing Method
TIG	Tungsten Inert Gas
TOF	Time of Flight
TOFD	Time of Flight Diffraction
Tx	Transmitter
UT	Ultrasonic Testing
VT	Visual Testing

Chapter 1

Introduction

1.1. Industrial Motivation

The UK remains a global leader within the manufacturing sector, repeatedly being ranked amongst the top 10 countries alongside China, the USA and Germany [1], with the outlook remaining positive for the remainder of 2023 and into the future [2]. It is undeniable that recent global events have placed significant pressures and challenges on the manufacturing sector worldwide. Covid-19 highlighted the volatility of global supply chains and their inflexibility to the major disruption caused by the pandemic [3]. As a result, reshoring and onshoring have become frequent topics of conversation, with countries, including the UK, recognising their dependence on overseas components, goods and workers [4–6]. Global supply chains are being tested once again, with the ongoing war in Ukraine placing substantial strain on the supply of raw materials and, most critically, oil and gas [7–9]. Furthermore, increased focus is being placed on the way that energy is consumed with a move to net-zero operations seen as critical in light of the climate crisis [10].

These global events, although challenging, have also been a catalyst for change and development. Innovation has become an imperative, with industrial sectors and businesses being forced to adapt and evolve at speed to a continuously changing global landscape. This drive towards innovation can be seen clearly within UK industrial sectors such as transport, energy and defence, where the motivation to remain globally competitive aims to place advanced manufacturing at the forefront of future investment plans [11–13].

Welding is an integral part of manufacturing and plays an important role in almost all aspects of everyday life. The rise in productivity found within the welding sector can largely be attributed to process automation which was first seen in the 1960's with the industrial application of a welding robot within the automotive industry [14]. However, it was not until the 1980's that robotic welding began gaining traction within other industries as the benefits of robotic deployment became clear [15]. Robotic welding is now a major application area for industrial robots [16], with articulated robots continuing to replace manual operations particularly in areas of High-Value Manufacturing (HVM) where joint strength and safety are of critical importance.

Many industrial sectors employ Non-Destructive Evaluation (NDE) as a means of ensuring the integrity of welded components at manufacture and throughout their service life. Often, these welded components are composed of thick sections which necessitate the need for high-integrity welding processes with multi-pass weld deposition strategies. As a general rule, NDE of multi-pass welds occurs as a final step in the manufacturing timeline, on the cold component and once a sufficient time period has lapsed so as to

detect delayed defects, such as hydrogen cracking, in accordance with international testing standards [17,18]. This greatly complicates the rework procedure, resulting in increased cost, particularly where defects are present in early weld runs, as a significant amount of work is required to excavate the defective area before repair and retesting. The NDE sector has not seen the same rate of uptake in automation as manufacturing sectors, with the majority of NDE operations continuing to be performed manually. As a result, inspection is often considered a major bottleneck within production environments.

In recent years, there have been increasing industrial and economic drivers to reduce manufacturing costs, particularly as the energy sector is being called upon to play a significant role in the delivery of low-carbon energy production in the future [19]. One way in which the NDE community can help to reduce this bottleneck and improve schedule certainty is to provide faster and more flexible NDE techniques capable of earlier defect detection without interrupting the welding and manufacturing process. The application of innovative in-process weld inspection and process monitoring techniques makes it possible to detect the formation of defects early, to enable quicker and more cost-effective action and repair. Furthermore, the valuable data gathered through in-process monitoring of welding processes may be used to control and optimise the process in real-time to reduce the overall rate of defect formation.

1.2. Research Goals

The research goals of the work in this thesis are:

I) Understand existing weld inspection techniques and their current applications.

II) Determine the state of the art in in-process weld inspection and monitoring techniques.

III) Identify the main challenges and complexities associated with in-process weld inspection and monitoring.

IV) Investigate the use of modelling techniques to predict the thermal gradients present within the weld volume with respect to in-process weld inspection.

V) Investigate the quantitative performance of a phased array ultrasonic inspection system providing in-process inspection during fusion welding of multi-pass welds.

VI) Investigate the application of traditional phased array ultrasonics for real-time monitoring of fusion welding processes through imaging of the molten weld pool.

1.3. Contributions to Knowledge

This thesis presents various unique and novel contributions with direct academic and industrially focused applications.

I) The development of experimentally validated thermal modelling techniques to predict the thermal gradients created by a Gas Tungsten Arc Welding (GTAW) process. (Chapter 3)

II) The development of a repeatable method for artificial defect embedding within weld volumes to provide known size reflectors for process verification. (Chapter 3)

III) The successful deployment of a phased array ultrasonic testing system capable of providing ultrasonic inspection at the point of manufacture. (Chapter 4)

IV) Utilising phased array ultrasonics to interrogate and image the molten weld pool in real time as a progression towards ultrasonic monitoring and control of the welding process. (Chapter 5)

V) The work presented in this thesis has had direct impact on further research into the development of in-process phased array ultrasonic weld inspection through various academic and industrially relevant projects.

1.4. Industrial Engagement

PEAK NDT Ltd., are a high-end technology company specialising in the development, production and support of multichannel and phased array ultrasound controllers for the NDE industry. PEAK NDT have long recognised the role of universities and academia to enable the development and implementation of their equipment within innovative NDE approaches. The systems PEAK NDT provide are based on an open

architecture platform, making them flexible and adaptable to the end user's requirements and the perfect building block for academic research and development.

As with a majority of the NDE community, PEAK NDT are noticing the effects of a global NDT skills shortage caused primarily by an aging workforce [20–22]. This is causing difficulties in recruitment, as it is becoming difficult to find candidates who are both skilled technically and also have the relevant commercial instinct. With the NDE market size projected to continue in growth throughout the period 2023 to 2030 [23], it is expected that the problems faced as a result of the aging workforce and skills gap is likely to intensify without changes being made. This has spurred PEAK NDT to look for new methods of recruitment through knowledge transfer partnerships [24] and student sponsorship.

Throughout this project, there has been a significant amount of collaboration with the industrial sponsor, PEAK NDT Ltd. This has included:

- Collaboration with NDE system integrators such as Transform NDT and The Welding Institute (TWI) to develop and provide impactful demonstrations and systems.
- Engagement with end-user companies by leading hardware and software demonstrations for companies both in the UK and abroad. Such companies include Babcock International Group plc, Altrad Babcock, BAE Systems, NOV, Northrop Grumman & Hitachi.
- Dissemination at conferences and exhibitions including the British Institute of Non-Destructive Testing (BINDT), the American Society of

Non-Destructive Testing (ASNT) & the European Conference for Non-Destructive Testing (ECNDT).

- Development and testing of High Dynamic Range (HDR) & high speed acquisition systems to facilitate the work presented in this thesis.
- Professional development through BINDT's Personnel Certification in Non-Destructive Testing (PCN) training and certification scheme to obtain Level 2D Ultrasonic Testing (UT) 3.1 & 3.2 (Plate & Pipe).

1.5. Thesis Structure

This thesis is structured as follows:

Chapter 2 records the relevant background theory which underpins this work, including a review into various fusion welding processes and the common defect types which may arise from them. A thorough review is given of various NDE techniques, with particular emphasis placed on the use of UT. Finally, an outline of current weld process monitoring techniques is given.

Chapter 3 discusses how the extreme temperatures and thermal gradients generated by the welding process affect the deployment of an in-process Phased Array Ultrasonic Testing (PAUT) weld inspection system. Experimentally verified thermal models are developed which are used to predict the thermal gradients within the weld volume in the plane of inspection. These thermal models have been used to develop thermal compensation strategies which were vital to the successful deployment of an in-process ultrasonic weld inspection system as presented in Chapter 4 of this thesis. Furthermore,

an artificial defect embedding strategy is introduced which allows for repeatable insertion of defects with known size, shape and length within the weld volume. This is of critical importance for the verification of in-process ultrasonic weld inspection systems and is also used within Chapter 4 of this thesis.

Chapter 4 introduces the use of phased array ultrasonics to provide inspection at the point of manufacture. The system concept is presented along with the associated technical challenges and opportunities. The effectiveness of established techniques developed to overcome these challenges is critically analysed and quantified. The successful deployment of the system is quantified and compared against traditional post-weld inspection techniques.

Chapter 5 explores the use of phased array ultrasonic testing technologies to monitor and analyse the molten weld pool during deposition of multi-pass gas tungsten arc welds. Analysis of the received ultrasonic signals are shown to contain information relating to key physical transitions within the welding process, namely the melting and solidification of the weldment. Significant signal changes are also shown to occur in the presence of a non-optimal or defective weld.

Chapter 6 documents the potential future work and concludes the main findings of this thesis.

1.6. Lead Author Publications Arising from this Thesis

1.6.1. Journal Papers

- ***Sweeney NE***, Lines D, Loukas C, Vithanage R, Vasilev M, MacLeod CN, Mohseni E, Parke S, Burnett A, Murray C, Symington M, Holt A, *"In-process ultrasonic inspection during fusion welding"*, Journal of Manufacturing Processes, submitted and under review
- ***Sweeney NE***, Lines D, Parke S, Loukas C, Vasilev M, Pierce SG, MacLeod CN, *"In-process phased array ultrasonic weld pool monitoring",* NDT and E International, Volume 137 (2023) 102850, doi: 10.1016/j.ndteint.2023.102850, July 2023

1.6.2. Conference Papers

- ***Sweeney NE***, Lines D, Parke, S, Loukas C, Vasilev M, Pierce SG, MacLeod CN, *"Towards real time quantitative monitoring and control of weld pool dimensions using phased array ultrasonics",* Proceedings of the American Society for Non-Destructive Testing (ASNT) 31st Research Symposium, June 2023

1.6.3. Conference Presentations

- Oral presentation at the American Society for Non-Destructive Testing (ASNT) annual conference (October 2023) *"In-Process Ultrasonic Inspection During Fusion Welding"*

- Oral presentation at the European Conference on Non-Destructive Testing (ECNDT) (July 2023) titled *"In-process monitoring and control of multi-pass fusion welding using phased arrays"*
- Oral presentation at the American Society for Non-Destructive Testing (ASNT) annual Research Symposium (June 2023) titled *"Towards real-time quantitative monitoring and control of weld pool dimensions"*
- Oral presentation at the American Society for Non-Destructive Testing annual conference (October 2022) titled *"Towards ultrasound driven, in-process monitoring and control of GTA welding of multi-pass welds for defect detection & prevention"*
- Oral presentation at the American Society of Mechanical Engineering Quantitative Non-Destructive Evaluation (QNDE) conference (July 2022) titled *"Towards real-time ultrasound driven inspection and control of GTA welding processes for high-value manufacturing"*
- Oral presentation at the American Welding Society Advances in Welding and Additive Manufacturing Research Conference (June 2022) titled: *"Towards ultrasound driven, in-process gas tungsten arc welding inspection and process control"*

1.7. Co-Author Publications Arising from this Thesis

1.7.1. Journal Papers

- Foster E, ***Sweeney NE***, Nicolson E, Singh J, Rizwan MK, Lines D, Pierce SG, Mohseni E, Gachagan A, Tant K, MacLeod CN, *"Thermal compensation of ultrasonic transmit and receive data for steel welded plates at the point of manufacture"*, NDT and E International Volume 137 (2023) 102812, doi: 10.1016/j.ndteint.2023.102812, July 2023
- Mohseni E, Javadi Y, ***Sweeney NE***, Lines D, Macleod CN, Vithanage RKW, Qui Z, Vasilev M, Mineo C, Lukacs P, Foster E, Pierce SG, *"Model-assisted ultrasonic calibration using intentionally embedded defects for in-process weld inspection"*, Materials & Design, Volume 198 (2021) 109330, doi: 10.1016/j.matdes.2020.109330, January 2021
- Vithanage RKW, Mohseni E, Qui Z, MacLeod CN, Javadi Y, ***Sweeney NE***, Pierce SG, Gachagan A, *"A phased array ultrasound roller probe for automated in-process/interpass inspection of multipass welds"*, IEEE Transactions on Industrial Electronics, 68 (2021) 12781-12790, doi: 10.1109/TIE.2020.3042112, December 2021
- Javadi Y, ***Sweeney NE***, Mohseni E, Macleod CN, Lines D, Vasilev M, Qui Zhen, Vithanage RKW, Mineo C, Stradoudaki T, Pierce SG, Gachagan A, *"In-process calibration of a non-destructive testing system used for in-process inspection of multi-pass welding"*, Materials & Design, Volume 195 (2020) 108981, doi: 10.1016/j.matdes.2020.108981, October 2020

- Javadi Y, ***Sweeney NE***, Mohseni E, MacLeod CN, Lines D, Vasilev M, Qui Z, Mineo C, Pierce SG, Gachagan A, *"Investigating the effect of residual stress on hydrogen cracking in multi-pass robotic welding through process compatible non-destructive testing"*, Journal of Manufacturing Processes, Volume 63 (2020) 80-87, doi: 10.1016/j.jmapro.2020.03.043, April 2020

1.7.2. Conference Papers

- Javadi Y, Hutchison A, Zimmerman R, Lines D, ***Sweeney NE***, Vasilev M, Mohseni E, Vithanage RKW, MacLeod CN, Pierce SG, Mehnen J, Gachagan A, *"Development of a phased array ultrasonic system for residual stress measurement in welding and additive manufacturing"*, Proceedings of the ASME 2022 Pressure Vessels & Piping Conference, July 2022

Chapter 2

Research Background

2.1. Fusion Welding Processes

Fusion welding is the process by which heat is used to join two or more materials [25]. The heat is commonly provided by an electrical arc struck between the welding electrode and the workpiece creating a localised heat source resulting in a small pool of molten material [26]. In most cases, extra material of the same type as the parent material is added to this pool by a filler rod or wire [27]. In general, a shielding gas is supplied around the weld site to prevent atmospheric contamination during the molten state [28,29], which can lead to the introduction of defects. The following sub-sections discuss some common fusion welding processes.

2.1.1. Manual Metal Arc Welding

Manual Metal Arc (MMA) Welding, also known as Shielded Metal Arc Welding (SMAW) or most commonly as stick welding, is the oldest and simplest fusion welding process. MMA uses consumable electrode rods, which are wire rods coated in a mixture of substances such as silicate binders, carbonates, metal alloys and other minerals [29], known as flux.

The electrode coating has several roles to play:

- It acts to stabilise the electrical arc.
- As the coating is heated, it produces vapours which act as a shield to protect the weld from atmospheric contaminants.
- It breaks down as it is heated to produce a protective coating, known as “slag”, which covers the weld, protecting it as it cools. The slag layer is then cleaned away once the weld is complete.
- Depending on its constituent materials, it can provide a source of alloying elements to aid in compatibility of the weld metal to the parent material.

These factors make MMA welding more suitable than other arc welding processes for use outdoors, as the protection provided by the flux makes an MMA weld less likely to be affected by atmospheric contamination. For other processes, which rely heavily on the external supply of a gas “shroud” to protect the weld, wind can blow the gas away, resulting in heavily contaminated welds [30]. Furthermore, as there is no need for an external gas supply, the equipment for MMA is significantly simpler and easily portable.

2.1.2. Gas Metal Arc Welding

Gas Metal Arc Welding (GMAW), or Metal Inert Gas (MIG) welding, has remained one of the leading industrial welding processes since the 1970’s [31]. GMAW uses a consumable filler wire as the electrode, which is continuously fed from a reel through flexible hosing to the welding torch. This makes GMAW more economical with fewer stop-starts than MMA where the electrodes require frequent replacement. GMAW

also differs from MMA as the shielding gas is supplied from an external source to create the protective shroud around the welding arc. The choice of shielding gas is most commonly mixtures of argon with some carbon dioxide (CO_2) and sometimes some oxygen (O_2) [32]. Where CO_2 is included, the welding process is referred to as Metal Active Gas (MAG) welding.

GMAW is a particularly flexible method, with applications in welding both thin and thick materials. The heat input can be made low to help minimise distortion and deformation of thinner sheet materials while its high deposition rate results in greater productivity when welding thick sections [29,33]. Furthermore, GMAW is suitable for use with a variety of materials including mild, low-alloy and stainless steels, aluminium and its alloys, copper, nickel and galvanized materials [31].

2.1.3. Submerged Arc Welding

Submerged Arc Welding (SAW) is similar to GMAW in that the electrode is also consumable and forms the filler material. However, SAW differs from other welding processes in that the arc and molten material are buried under granular flux which is fed continuously into the weld joint [29]. Therefore, the arc is not visible to the naked eye, resulting in an improved working environment when compared to other arc welding processes [34]. The granular flux provides the protective gas shield over the molten pool and a slag covering on the solidified weld bead and may also be providing supplementary alloying elements into the weld zone [29,35]. SAW is used primarily for thicker weld sections due to its high deposition rate and deep weld penetration which allows the necessary amount of filler material to be reduced [34]. Generally, SAW is an automated

process where either the weld head or the workpiece movement is mechanised, often through the use of gantry or column and boom units [34,36].

2.1.4. Gas Tungsten Arc Welding

Gas Tungsten Arc Welding (GTAW), or Tungsten Inert Gas (TIG) welding, uses a non-consumable tungsten electrode to generate the electrical arc between itself and the metal workpiece [37]. The term non-consumable means that the tungsten itself does not melt and become part of the weld. Tungsten is used because it has the highest melting point of all metals at 3410°C [38] meaning that it can carry very high welding currents without melting. In comparison with other welding processes, where the filler material also acts as the electrode, GTAW creates a more precise and stable arc making the weld more controllable [37] which helps to reduce the Heat-Affected Zone (HAZ) of the weld. GTAW, if performed correctly, produces no sparks or spatter, as there is limited metal transfer across the arc, producing welds of a superior quality [29]. In a similar manner to GMAW, the gas supply is external and the composition is chosen depending on the material being welded, with pure argon and argon-helium mixes being the most common for use with carbon steels [39]. Although the welds produced are significantly cleaner, GTAW has a significantly lower deposition rate than GMAW [29].

2.1.5. Plasma Arc Welding

Plasma Arc Welding (PAW) is an extension of the GTAW process with key differences being found in its heat source and applications [29]. As the name suggests, PAW uses a high-temperature ionised gas, known as plasma, as the required heat source.

A tungsten electrode is used to strike an electrical arc with the workpiece. This electrical arc heats the surrounding plasma gas to create the plasma which is then forced through a constricted copper nozzle to increase the flow rate and energy density [40]. Shielding gas is delivered through an outer nozzle from a separate supply. Filler material may be added in a similar manner to GTAW. Figure 2.1 shows a cross section schematic of a PAW torch, indicating the inner and outer nozzles and arc constriction.

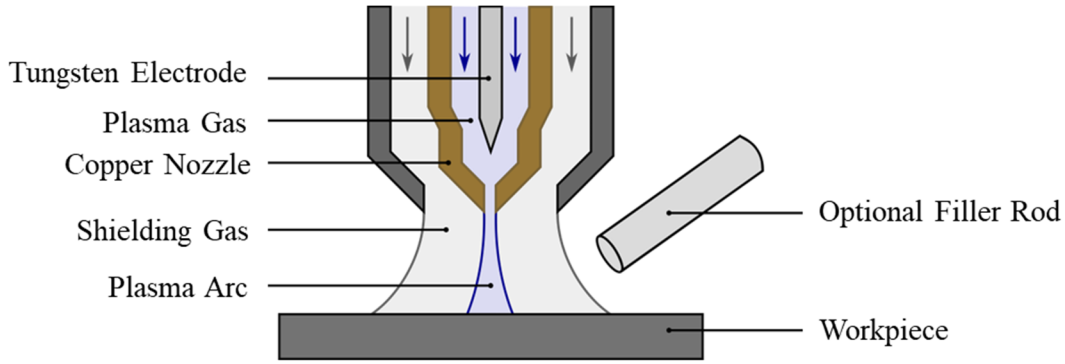

Figure 2.1. Sectional schematic view of a plasma arc welding torch

The higher energy concentration of this method results in some significant advantages [29]. PAW is able to achieve higher welding speeds using lower currents than alternative processes. Furthermore, PAW results in lower shrinkage and distortion of the finished part. The equipment needed to perform PAW is highly specialised and, therefore, it is typically found in industrial settings where its capabilities can be leveraged fully.

2.1.6. Electron Beam Welding

Electron Beam Welding (EBW) is a highly specialised fusion welding process whereby a stream of high energy electrons is focused on the workpiece using magnetic fields [41]. As the beam of electrons impact the surface of the material their kinetic energy

is converted to heat which causes the material to melt and form a weld pool. The presence of gases in the welding environment causes scattering and absorption of the electron beam and therefore, the process must be performed in a vacuum environment [42]. EBW is a versatile welding process, with applications for both thin sheet materials and thick section butt joints over 200 mm in thickness [42]. Its high penetration power means that it is capable of welding thick section material in significantly fewer passes than alternative arc welding processes, with 50 mm thick welds requiring only one or two passes [43]. EBW provides high welding speeds and deposition rates. However, when considering the overall productivity rate it is important to also consider the time taken to create the vacuum welding environment [42].

2.1.7. Resistance Welding

Resistance Welding (RW) is a process by which materials are joined together through the application of pressure and high electrical currents [44]. The most common application of this welding process is Resistance Spot Welding where copper electrodes are used to provide the clamping force and the electrical current to join thin sheet metal panels. As electrical current is passed through the base metal via the copper electrodes, a maximum point of resistance is experienced at the interface between the two plates which raises the temperature in this region to the point of plasticity [45]. This results in the formation of an elliptical shaped weld referred to as a "nugget". Figure 2.2a shows a schematic of the spot welding process. In an analogous process, known as resistance seam welding, the copper electrodes are in the form of wheels which rotate as the workpiece is rolled between them creating a continuous seam weld. Resistance seam welding is

commonly used in the production of gas- and fluid-tight joints such as those found in fuel tanks [44] and nuclear waste canisters [46]. A schematic showing resistance seam welding is shown in Figure 2.2b.

2.2. Weld Joint Geometry

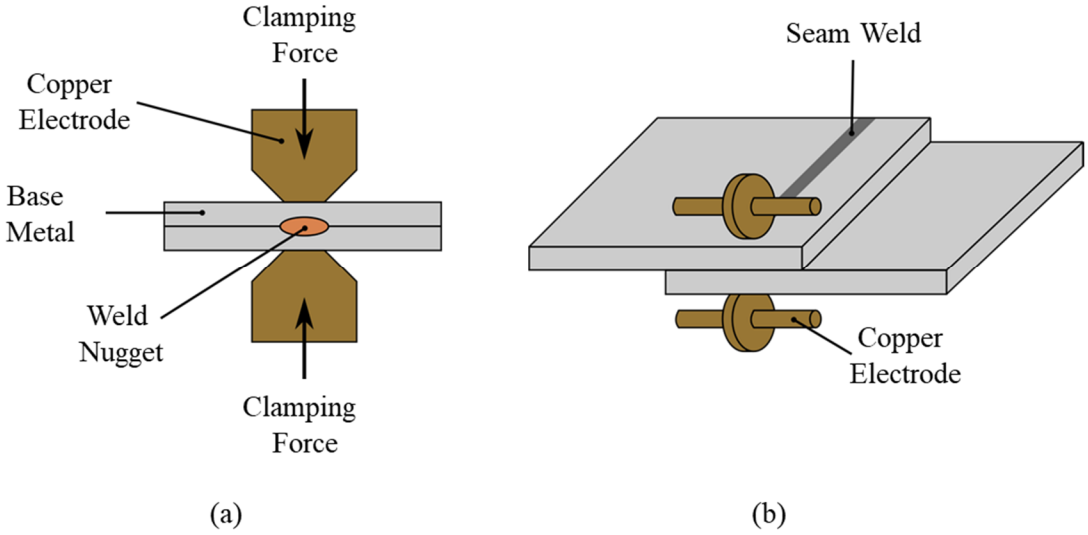

Figure 2.2. Schematics of (a) resistance spot welding and (b) resistance seam welding

The joint configuration, meaning the geometry and placement of a weld within a structure, is vital to ensuring that the loads within the structure are distributed correctly. Many factors dictate the choice of joint configuration, including accessibility for welding and inspection, welding process selection and the type of loading [47]. The basic joint configurations are shown in Figure 2.3 and include butt, corner, tee, lap and edge joints [48].

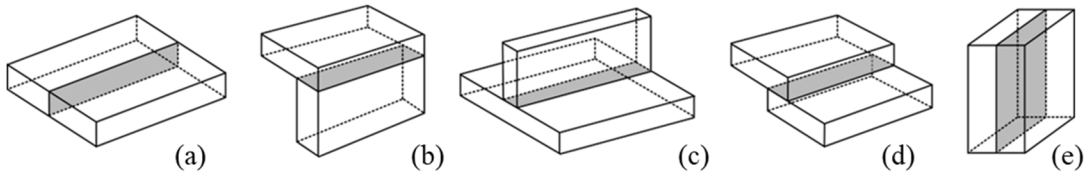

Figure 2.3. Basic weld joint configurations including (a) butt (b) corner (c) tee (d) lap and (e) edge

Depending on the weld properties required and the dimension of the weld site, the joint may be subject to a form of edge preparation on one or both of the pieces [49]. This is to allow appropriate access for the welding torch and to achieve even heat input and weld penetration. Figure 2.4 shows common joint preparations for thick butt welded joints including (a) single-V, (b) double-V, (c) single-J and (d) double-J.

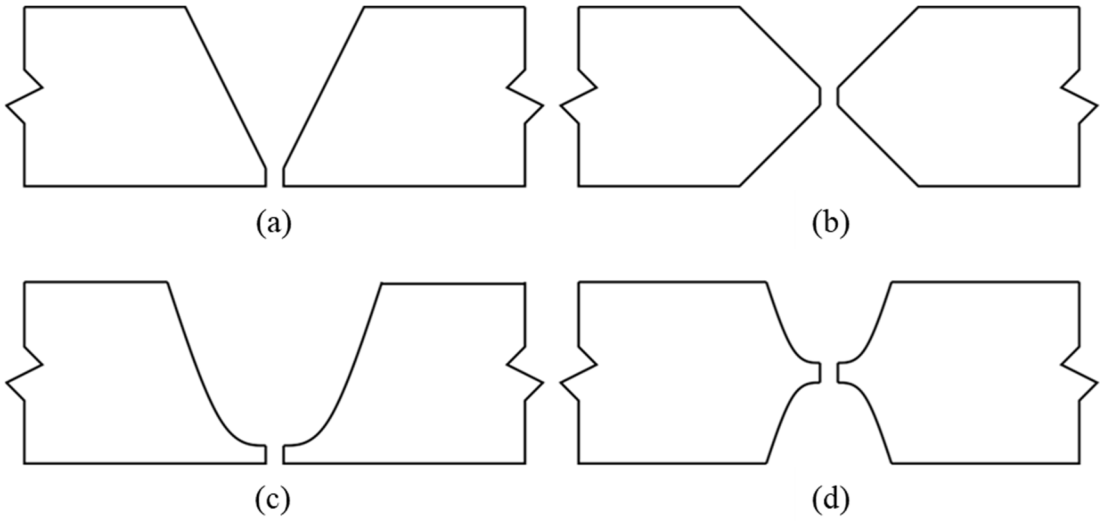

Figure 2.4. Common edge preparations for butt joints including (a) single-V, (b) double-V, (c) single-J and (d) double-J

Figure 2.5a introduces the terminology relating to a single-V butt weld with an open root gap. The addition of a root gap helps to ensure proper fusion and penetration of the weld through the bottom surface of the plate. Often a vertical face is left at the root of

the weld, known as the root face, this helps to control the penetration and prevent burn through from excessive heat. Figure 2.5b shows further terminology associated with a completed weld where the weld toes are indicated as the junction between the weld face and the parent material. The HAZ of the weld is also highlighted referring to the area of the parent metal which is not melted during the welding process but does experience microstructure and grain structure alterations due to the input of heat [27].

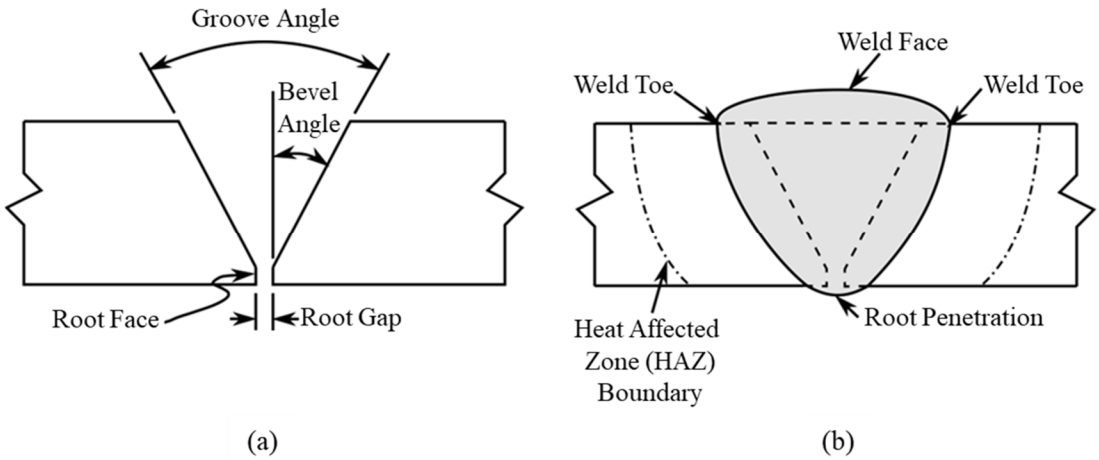

Figure 2.5. (a) Nomenclature relating to single-v edge preparations and (b) associated weld penetration indicating important terminology including the Heat Affected Zone (HAZ)

2.3. Multi-Pass Welding Nomenclature

When welding thicker sections, as is common within many industries such as Nuclear, Defence, Marine and Oil & Gas, a single weld bead is not sufficient to fill the weld joint volume [50]. Therefore, a multi-pass weld deposition strategy is necessary, where several weld passes are laid down in layers to fill the weld volume. Figure 2.6 shows the terminology used when referencing a standard multi-pass welding procedure for a single-V butt weld. The root pass is the initial pass used to join the two sections

together. The hot pass is the second weld pass performed, used to reshape the root pass and ensure sufficient penetration of the previous pass. Fill passes serve to fill the remaining weld volume to the top of the weld groove. Cap passes are then used to provide reinforcement and give the weld site a clean weld face to finish.

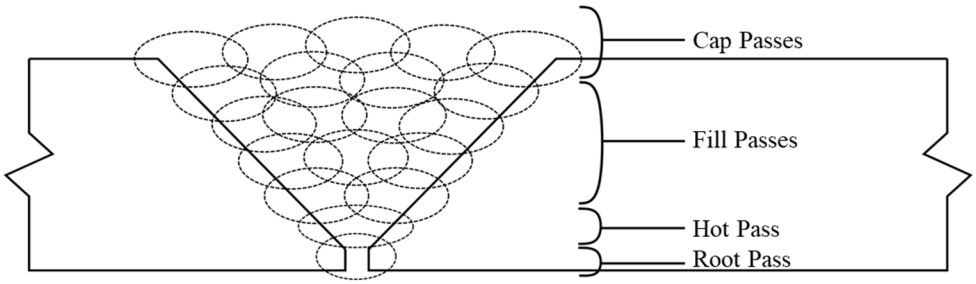

Figure 2.6. Single-V groove geometry with multi-pass weld terminology highlighted

2.4. Common Welding Defects

Weld defects are flaws which affect the quality and integrity of a welded joint. Different welded joints may have varying expected or necessary quality standards depending on the service requirements, as defined by internal company standards [51]. Defects may form due to discontinuities formed during welding, where the welding procedure has not been optimum or may be a direct result of improper welding parameters. Discontinuities may amplify stress distributions and alter the mechanical or chemical properties of the weld or HAZ. Figure 2.7 shows some common welding defects as classified by BS EN ISO 6520-2:2013 [52].

Porosity refers to areas of entrapped gas, usually occurring as a result of insufficient shielding gas flow or contamination of the material surface before welding [53]. Gas pores are generally spherical in shape, however, may be elongated forming

"worm-hole porosity" [54]. In general, porosity is not deemed a serious threat during normal loading conditions and therefore has reasonably lenient acceptance criteria [51].

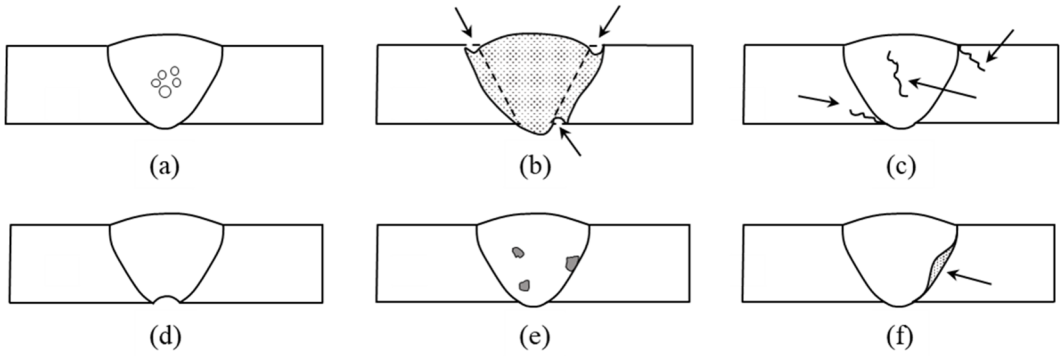

Figure 2.7. Common welding defects including (a) porosity, (b) undercut, (c) cracking, (d) lack of root penetration, (e) inclusions and (f) lack of sidewall fusion

Undercut is a geometrical imperfection characterised by a groove running parallel to the weld length along the toe of the weld or between weld passes [55]. It is associated with improper welding technique and excessive currents. Undercut creates a sharp transition in weld geometry, resulting in a stress concentration point and subsequently reducing fatigue properties [51]. Due to it being a common defect, most acceptance criteria do allow for some level of undercut [56].

Cracks occur where localised stresses exceed the tensile stress of the material [51] and are often associated with areas of stress concentration around geometrical discontinuities, such as undercut. Cracking within welds can be further divided into categories relating to their initiation and propagation. Hot cracks develop during welding or just prior to solidification of the weld pool at elevated temperatures [51,57]. They are associated with insufficient molten material being present to fill the space between the solidified material resulting in excess shrinkage strains which cause the weld to tear.

Generally, hot cracks form at the centreline of welds, where shrinkage strains are at their highest, and propagate between grain boundaries [58]. Cold cracks are often delayed and associated with hydrogen embrittlement as a result of diffusion of hydrogen within the material [59,60]. Toe cracks initiate and propagate from the toes of the weld where residual stresses are higher. They are a result of thermal shrinkage in the HAZ material [51].

Lack of Root Penetration (LORP) occurs where the weld bead has not fully bonded the fusion faces at the root of the weld [51,61]. Lack of Root Fusion (LORF) occurs where the weld bead fails to fuse one side of the joint only. This can occur due to improper fit-up or joint design, inadequate heat input or improper welding parameters.

Solid inclusions refer to solid foreign substances trapped within the weldment such as slag or tungsten inclusions. Slag inclusions can form when improper removal procedures are adopted, generally when access to the joint is limited [51]. Tungsten inclusions can form where the tungsten electrode has been unintentionally dipped into the molten weld pool or where excessive current has been used which results in the melting of the electrode tip [51,62].

Lack of Sidewall Fusion (LOSWF) occurs when the weld material does not fuse properly with the bevel of the edge preparation, resulting in the formation of a gap. This is caused by improper welding technique and parameters, restricted joint access or poor cleaning of the base material prior to welding [63].

2.5. Non-Destructive Evaluation

Non-Destructive Evaluation (NDE) is a generic term for a group of non-invasive techniques used to quantitatively investigate the properties of a material or component without causing damage. The term NDE is often used interchangeably with Non-Destructive Testing (NDT), however, NDE describes a more quantitative method where measurements are taken either to do with defects found (size, shape, orientation) or the material properties. The term NDE will be used throughout the remainder of this thesis.

NDE plays a critical role in the safety of many products, infrastructure and engineering systems, helping to ensure their integrity both at the point of manufacture and throughout their service life. The importance of NDE within industries such as nuclear, defence and aerospace cannot be overstated as it is used to predict and prevent catastrophic failures.

2.5.1. Visual Testing Techniques

Visual Testing (VT) is the most basic and inexpensive NDE technique. Nevertheless, it plays an important role in detecting surface-breaking defects. Often, defects which will have the most detrimental effect on the strength and safety of the component are surface-breaking and visible to the human eye with careful inspection [64,65]. This can allow for immediate rejection or repair of a component without the need for the use of other more expensive and time-consuming inspection techniques.

VT techniques can be further enhanced with the use of Penetrant Testing (PT) or Magnetic-Particle Testing (MT). In many cases, cracks can be particularly deep with only

a very small opening visible on the surface of the material and therefore are particularly difficult to detect under normal visual inspection [66]. The basic principle of PT is that a liquid dye is added to the surface of the material which is then drawn into the volume of the crack. Excess liquid is removed and a developer is then added to the surface to draw the trapped dye out [67,68]. The added contrast of the developer and the dye makes surface breaking defects significantly easier to detect. Figure 2.8 shows the application of PT to a small-bore circumferentially welded pipe, highlighting its use in adding contrast to surface-breaking flaws.

(a) (b)

Figure 2.8. (a) Dye penetrant added to the surface of a small-bore circumferential pipe weld and (b) developer added, highlighting surface-breaking porosity. These images were taken by the author during a practical NDT course at Lavender NDT Intl.

MT is a quick and simple inspection technique suitable for the detection of flaws within ferromagnetic materials [69]. The material under test is magnetised either locally, by applying a magnetic yoke across the area, or entirely by passing an electrical current through the part and inducing a magnetic field. This introduces a magnetic flux within the material, which can be used to detect any flaws which will disrupt its otherwise uniform shape and density. In a sound material, without discontinuities, the magnetic flux will be contained within the material and of uniform shape and distribution. However, the

presence of a discontinuity will distort the shape of the magnetic field resulting in some flux leakage around the discontinuity. This flux leakage is made visible by applying fine iron particles, either dry or as part of a liquid suspension, to the surface of the material. The iron particles will collect around regions where there is magnetic flux leakage present indicating a discontinuity [69]. Figure 2.9 shows MT applied to a carbon steel plate weld, highlighting the presence of a surface-breaking crack.

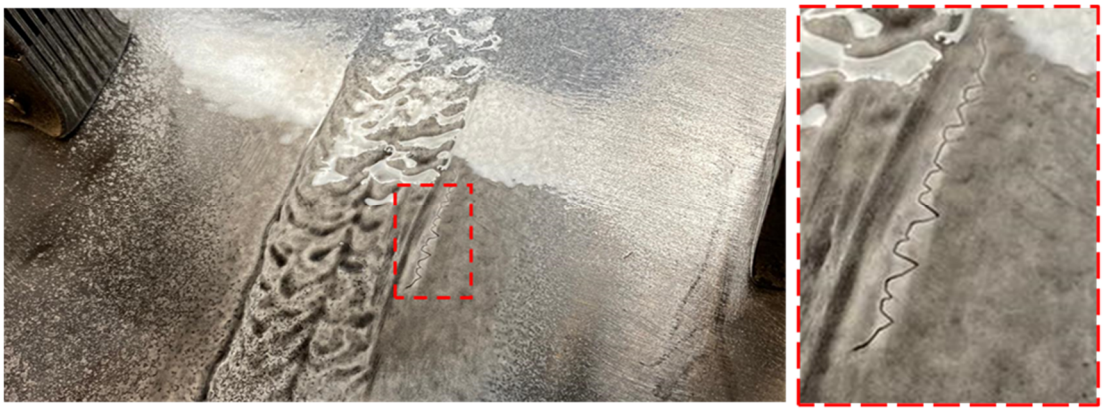

Figure 2.9. Magnetic Particle Testing (MT) applied to a carbon steel plate weld. These images were taken by the author during a practical NDT course at Lavender NDT Intl.

2.5.2. Eddy Current Testing

Eddy Current Testing (ECT) is an NDE technique which uses the principle of electromagnetic induction to detect and characterise both surface-breaking and sub-surface flaws [70,71]. ECT is a technique which can be applied only to electrically conductive materials such as metals, graphene and concrete [72]. ECT has the advantage of being suitable for use on painted and coated surfaces, with little effect on the results, since no direct electrical contact is necessary. This makes ECT a useful technique for

accurately measuring and monitoring the thickness of coatings [73] e.g. anti-corrosive coatings used to prevent rusting of safety-critical components.

2.5.3. Radiographic Testing

Radiographic Testing (RT) is a volumetric inspection technique, most commonly associated with medical imaging. However, the same underlying principle is also applied for the imaging of industrial components and structures to monitor their health and integrity [74,75]. Traditional physical film based RT is a time-consuming procedure owing to the exposure time necessary, which is dependent upon the material type and thickness. Digital RT is a faster and more flexible option but is less common within industrial environments. A high-level of skill is required to interpret the final images, which do not indicate depth of any flaws, only size and location [75]. RT has significant limitations in terms of applicability on thicker materials [76] and the need for radiation safety management [77].

2.5.4. Ultrasonic Testing

Ultrasonic Testing (UT) is the application of ultrasonic waves into objects or materials for characterisation or for flaw detection. Ultrasonic waves are sound waves with frequencies above the range of human hearing, > 20 kHz, with common frequencies for NDE applications being in the range of 1 to 10 MHz. UT is the most common NDE technique within a variety of industries owing to its versatility, high penetration power, allowing for flaw detection deep within components, and its ability to locate, size and characterise both planar and volumetric defects with high sensitivity [78,79].

2.5.4.1. Wave Propagation Principles

Since ultrasonic waves are mechanical vibrations of the particles within the material rather than electromagnetic radiation, the wave propagation can be characterised by its interaction with the material particles [79] as shown in Figure 2.10.

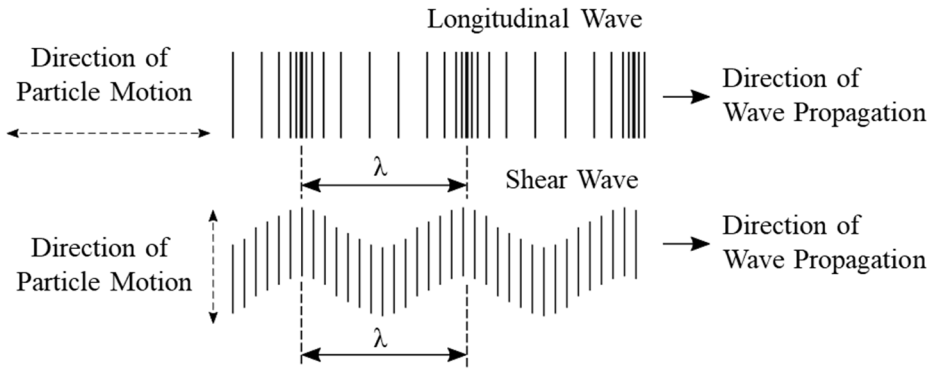

Figure 2.10. Ultrasonic wave modes relative to material particle motion: longitudinal (top) and shear (bottom)

If the particle motion is along the same line as the direction of wave propagation, the wave is known as a longitudinal, or compression, wave. Here, the particles are being compressed and expanded along the axis of propagation. If the particle motion is perpendicular to the direction of wave propagation, the wave is known as a shear, or transverse, wave. There are other modes of wave propagation, such as Rayleigh and Lamb waves, however longitudinal and shear are the most common within industrial NDE applications. While longitudinal waves can propagate in solids, liquids and gases, the transmission of shear waves is limited to solids as liquids and gases have no shear strength with which to support the transverse movement of particles [79]. As a general rule, the shear wave velocity in a material is approximately half that of the longitudinal velocity resulting in a shorter wavelength (λ) [79]. The wavelength of the ultrasonic wave is related

to the wave speed (c) and the frequency (f) through the well-known formula given in Equation (2.1).

$$f = \frac{c}{\lambda} \tag{2.1}$$

2.5.4.2. Attenuation

As ultrasonic waves propagate through media, they are subjected to energy loss through scattering and absorption [80]. This loss of energy is known as attenuation and is highly dependent on both material structure (grain size and orientation) and the frequency of the ultrasonic wave within the material. Higher frequency waves experience higher attenuation due to their short wavelength [79]. Attenuation of ultrasonic waves can be generalised using Equation (2.2).

$$A = A_o e^{-\alpha d} \tag{2.2}$$

Where A is the amplitude of the wave after some distance, d, has been travelled, A_o is the initial amplitude and α is the attenuation coefficient and is a function of frequency.

2.5.4.3. Ultrasonic Waves at Boundaries

When an ultrasonic wave meets a boundary between two different materials, part of the acoustic energy is transmitted across the boundary while the rest is reflected [79,81]. The amount of energy transmitted is dependent on the *acoustic impedance* of the materials either side of the boundary. Acoustic impedance in a lossless, isotropic material can be calculated from Equation (2.3).

$$Z = \rho c \tag{2.3}$$

Where Z is the acoustic impedance (kg/m^{2}s or Rayl), ρ is the material density (kg/m^3) and c is the ultrasonic wave velocity within the material (m/s).

For two materials of different acoustic impedances, Z_1 and Z_2, the percentage of transmitted energy (E_T) and reflected energy (E_R) can be calculated using Equation (2.4) and Equation (2.5) respectively.

$$E_T = \frac{4Z_1Z_2}{(Z_1 + Z_2)^2} \times 100 \tag{2.4}$$

$$E_R = \left(\frac{Z_1 - Z_2}{Z_1 + Z_2}\right)^2 \times 100 \tag{2.5}$$

In the simplest case, the ultrasonic wave is incident on the boundary perpendicularly, as shown in Figure 2.11a, where the incident, reflected and transmitted waves are denoted i, r and t respectively. In the case where the ultrasonic wave is incident at some angle other than normal, the waves will be transmitted and reflected at different angles. The transmitted wave will undergo some *refraction*, where the direction of propagation changes, as shown in Figure 2.11b. The angle of refraction can be calculated using *Snell's Law*, a simple relationship given by Equation (2.6).

$$\frac{\sin\alpha}{\sin\beta} = \frac{c_1}{c_2} \tag{2.6}$$

Where α and β are the angles of incidence and refraction respectively and c_1 and c_2 are the ultrasonic wave velocities in materials 1 and 2 respectively.

Additionally, when an ultrasonic wave is incident on a boundary at an angle, the wave undergoes *mode conversion* upon reflection and refraction, meaning that both longitudinal and shear waves are produced. This only occurs in materials where both longitudinal and shear waves can be supported, i.e. solids. Figure 2.11c shows a shear wave incident upon a solid-to-solid boundary and the resultant mode converted waves.

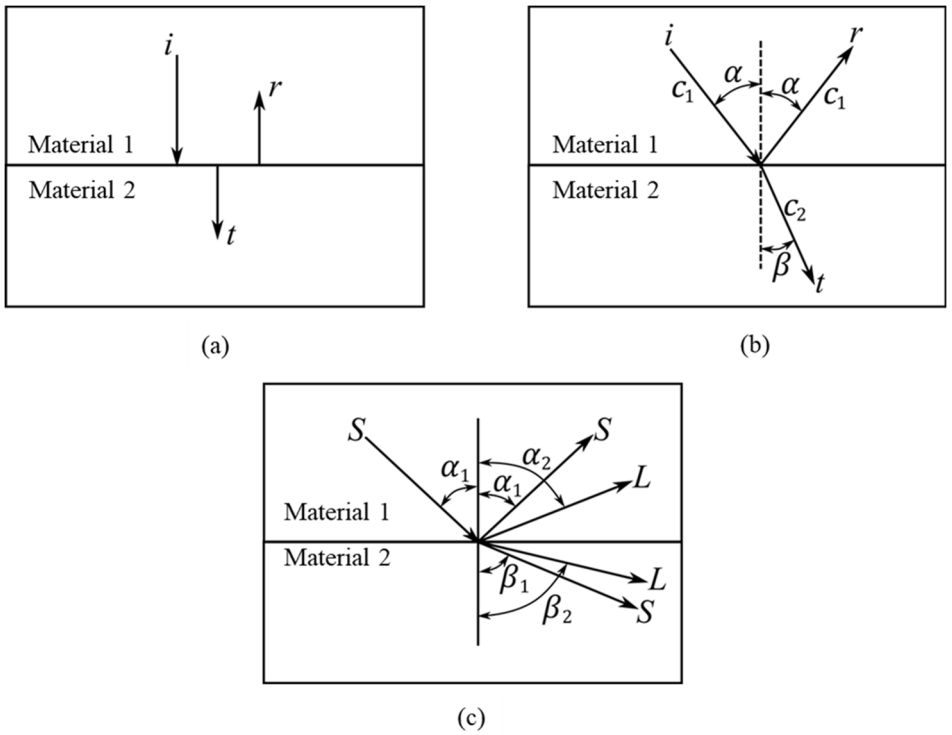

Figure 2.11. Ultrasonic waves incident on boundaries (a) planar incidence, (b) oblique incidence and (c) oblique incidence with mode conversion highlighted. S - shear wave mode, L – longitudinal wave mode

When the order of relative acoustic impedances across a boundary is from high to low (e.g. a boundary of steel to water), the reflected wave will undergo *phase reversal* [81], where it is 180° out of phase with the incident wave, as shown in Figure 2.12.

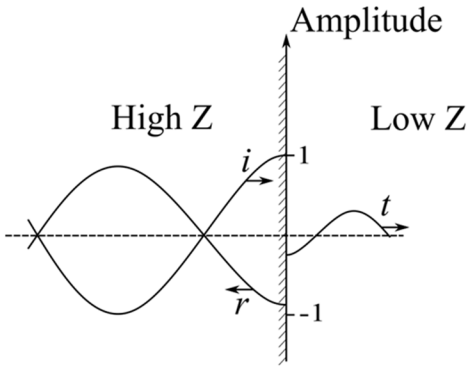

Figure 2.12. A plane wave incident upon a high-Z to low Z boundary

2.5.4.4. Beam Spread

The particles within a material do not transfer 100% of the acoustical energy in the direction of propagation. This results in what is referred to as beam spread, where the sound field from a transducer diverges from the expected path. Figure 2.13 shows a simplified Two Dimensional (2D) diagram indicating the diminished beam energy as it expands further from a central axis.

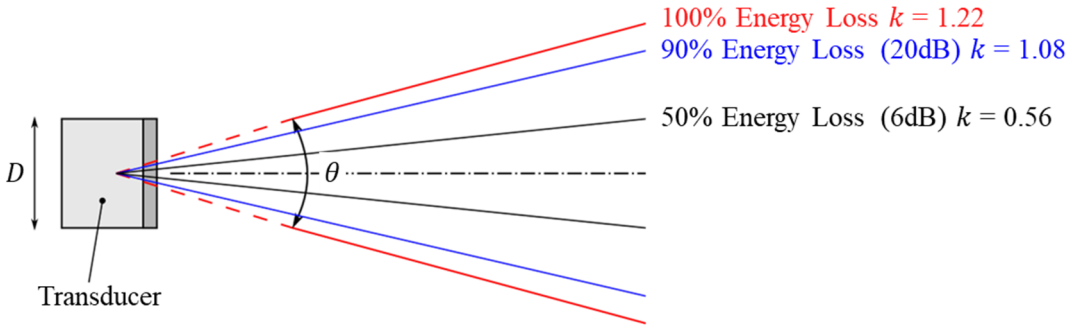

Figure 2.13. Beam spread characteristics for varying energy losses

The beam spread for a given ultrasonic transducer can be calculated using Equation (2.7).

$$\sin\left(\frac{\theta}{2}\right) = \frac{k\lambda}{D} = \frac{kc}{Df} \tag{2.7}$$

Where θ is the angle of the beam spread around the central axis of the beam, as show in Figure 2.13, D is the element diameter and k is a constant used to calculate the beam spread values for various energy losses.

2.5.4.5. Generation Methods

There are a number of methods for generating ultrasonic waves, with the primary method for industrial applications utilising the *piezoelectric effect* [82]. A piezoelectric material has the property by which it generates an electrical charge in response to applied mechanical stress. The inverse of this is also true, in that if an electrical current is applied across a piezoelectric material, it will deform. These phenomena form the basis for the generation and reception of ultrasonic waves where ultrasonic transducers utilise elements made from piezoelectric materials such as Barium-Titanate and Lead Zirconate Titanate (PZT).

Laser ultrasonics is a non-contact method for ultrasound production, where the piezoelectric transducer and detectors are replaced by a laser and optical system [83]. The generation of ultrasound by this technique utilises the thermoelastic properties of the material. By exposing the surface of a material to a pulsed laser beam, rapid heating and cooling of the material causes local expansion and contraction, resulting in the generation of ultrasonic waves within the material [84].

Electromagnetic Acoustic Transducers (EMATs) utilise the electromagnetic-acoustic phenomena to generate ultrasonic waves within components without the need to be in direct contact with the material surface [79]. A flat coil of current

carrying wire and permanent magnet are used to induce eddy-currents within the material. The interaction of the static magnetic field and the eddy-current density within the material results in Lorentz forces which cause the generation of ultrasonic waves [85]. This method has the advantage of being non-contact, couplant-free and suitable for use within high-temperature environments [86].

2.5.4.6. Conventional Ultrasonic Testing

Conventional ultrasonic testing utilises single-element piezoelectric transducers for transmission and reception of ultrasonic signals. In most instances, the transducers are in direct contact with the surface of the material under test, with a thin layer of couplant in between which acts to reduce the impedance mismatch between the materials and increase transmission energy. Figure 2.14 shows a pulse-echo configuration, where a single transducer is used to both transmit (Tx) and receive (Rx) the ultrasonic signal. In the presence of a flaw, which could be a loss of wall thickness, delamination or inclusion, the ultrasonic energy is reflected back due to the acoustic impedance mismatch, resulting in additional echoes within the ultrasonic A-scan (amplitude display). The initial pulse shown in the A-scan is caused by the continued ringing of the piezoelectric crystal after transmission and can mask any near surface flaws. This can be eliminated by using a split-crystal probe with two separate, acoustically isolated crystals, where one is used to transmit and the other to receive. This is the standard set up for thickness measurement and the initial inspection of the parent material of a welded component. The thickness of the component can be determined by accurately knowing the acoustic velocity of the

material under test, and similarly the depth of defects or loss of wall thickness can be calculated.

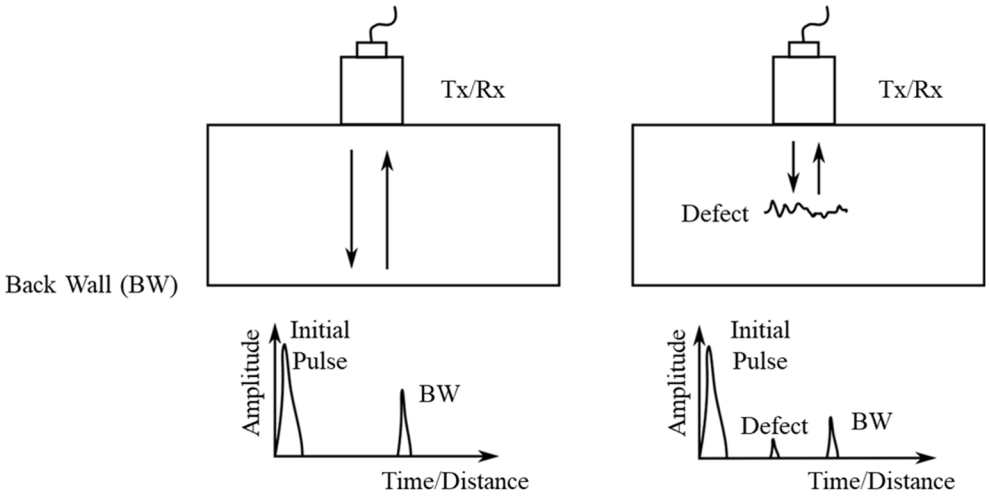

Figure 2.14. Pulse-echo ultrasonic testing with representative A-scans shown

2.5.4.7. Conventional Ultrasonic Testing of Welds

UT of welded components relies on the use of wedges, which are designed to utilise refraction to introduce shear waves at specific angles into the weld volume. This is known as *angled beam inspection*. Standard weld inspection probes are available in common angles of 45°, 60° and 70° although any angle is possible through correct wedge design. Standard wedge materials include Perspex and Rexolite, while specialised materials can be used to gain specific properties such as temperature resistance. Shear waves are used due to their shorter wavelength which results in increased sensitivity to smaller flaws within the material. As a general rule, the smallest detectable defect size is equal to half of the acoustic wavelength within the test material [87]. Figure 2.15a shows a standard pulse-echo, angled beam inspection of a weld where the resultant refracted

angle is denoted θ. Figure 2.15b shows how a flaw within the weld, such as a LOSWF, results in the ultrasonic wave being reflected.

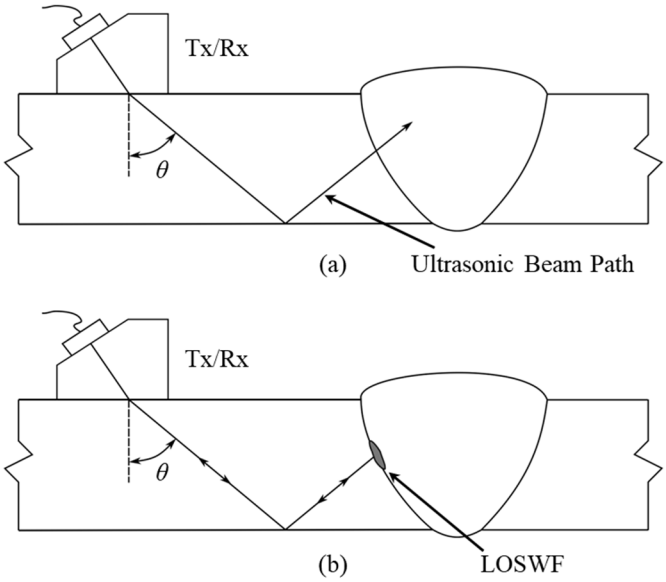

Figure 2.15. Angled beam inspection of a weld with (a) no flaws present and (b) a LOSWF present

2.5.4.8. Standard Phased Array Ultrasonic Testing

Phased Array Ultrasonic Testing (PAUT) has become increasingly popular in many NDE applications in recent years. Ultrasonic arrays are made up of a number of independently connected piezoelectric elements which can be individually controlled. This offers a higher degree of flexibility when compared with conventional and split-crystal piezoelectric transducers [88]. By individually controlling the firing times of each element, the shape and direction of the ultrasonic beam can be modified, this is known as *beam forming* [79]. Figure 2.16a shows a plane wave imaging approach where all elements are fired simultaneously while Figure 2.16b and Figure 2.16c show how different firing delays can be applied to generate focused and steered beams respectively.

Phased arrays therefore offer the ability to implement a large number of inspection modalities with a single transducer from a single inspection point, increasing coverage, inspection speed and sensitivity [89].

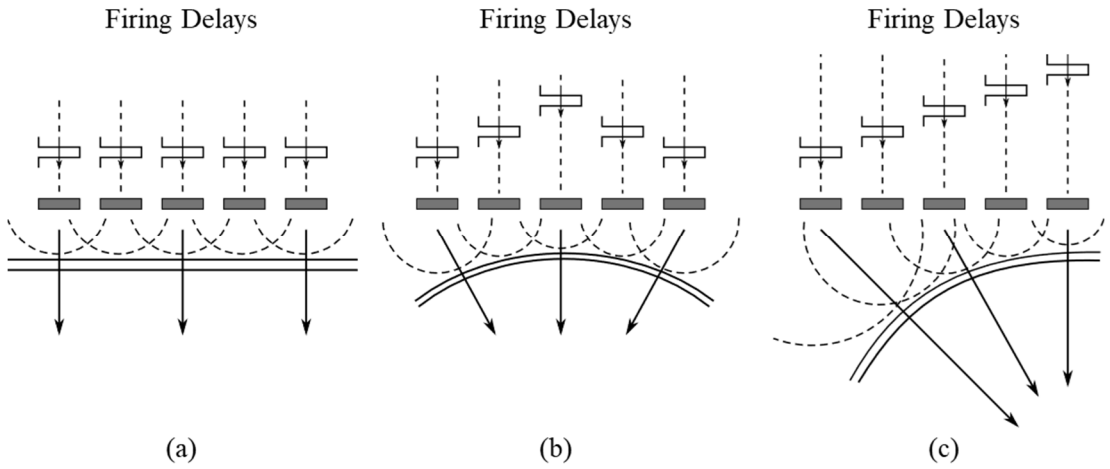

Figure 2.16. Phased array beam forming with respective firing delays for (a) plane wave, (b) focused, (c) steering and focusing

PAUT also enables the use of Full Matrix Capture (FMC) where all possible transmit-receive pairs are acquired. By capturing this data at the point of inspection, post processing allows for beam-forming to be applied retrospectively. FMC also facilitates the use of advanced post-processing techniques such as the Total Focusing Method (TFM) [90].

2.5.4.9. Data Presentation

Ultrasonic data can be displayed to the user in a variety of formats to aid in their understanding and interpretation. The three most common ultrasonic display formats within NDE are the A-scan, B-scan and C-scan. Each of these display formats offers a different way of looking at the material or component under test.

The raw ultrasonic data is collected as an amplitude vs. time trace displayed as an amplitude scan or A-scan as shown previously in Section 2.5.4.6. This is the simplest and most common method for displaying ultrasonic data and forms the basis for all other display formats. A-scan data can be displayed in its natural Radio Frequency (RF) form, as a fully rectified signal or either the positive or negative half of the RF signal, depending on the user's preference [91].

Aligning a series of A-scans along the axis of transmission results in a B-scan display, where amplitude is represented by a colour- or grey-scale. A B-scan is a plot of the ultrasonic data as a 2D cross-sectional view of the component under test [91]. B-scans are commonly used within PAUT testing of welds, where beam-steering is used to sweep the ultrasonic inspection beam through several angles, known as sectorial scanning. The resultant A-scan signals are stacked beside one another, maintaining their insonification angle, to produce a B-scan commonly referred to as a Sectorial Scan (S-scan). A standard manual PAUT setup is shown in Figure 2.17. Here, two Side Drilled Holes (SDHs) act as reflectors within the weld volume and can be seen as indications on the resultant B-scan image. Overlaying the weld geometry within the B-scan aids in interpretation of the ultrasonic data, particularly where multiple skips are performed during the inspection.

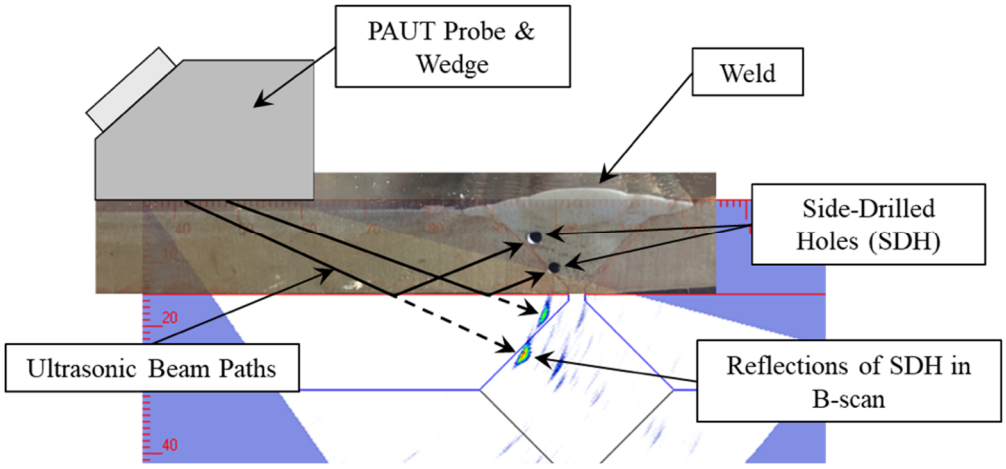

Figure 2.17. Ultrasonic B-scan for PAUT weld inspection showing full skip inspection of SDH's. This data was collected by the author.

A C-scan display format gives a 2D image in the plane parallel to the sample surface in a plan-type view [91]. They are produced by gating the corresponding A-scans to provide a single value for each imaged point, which can then be displayed using a colour- or grey-scale. C-scans are commonly used to display corrosion maps and can be modified to show quantitative measurements, such as the extent of wall thickness loss, in a way that is more intuitive to the user [92].

2.6. Weld Process Monitoring

The automation of welding processes has increased the necessity for providing efficient and capable monitoring techniques to help ensure weld quality. Monitoring of the welding process is one way in which the prevalence of defects and discontinuities can be managed and reduced. In its simplest terms, this can mean monitoring and controlling weld parameters, such as current and voltage, a technique offered by most modern welding power supplies. In GTAW, for example, the arc length is directly proportional to the arc

voltage. Therefore, by monitoring the arc voltage and comparing it to a preset desired parameter value, a control system may be implemented to regulate the arc length or torch height [93]. More advanced techniques use external sensors and multiple input sources to monitor and control the welding process.

One of the most important information sources which requires monitoring to help ensure weld quality is the weld seam [94]. Weld seam tracking has been successfully implemented using laser and active vision systems [95–98] which utilise structured light patterns and algorithms to provide information about the weld groove geometry. This information can be utilised to provide path planning and motion control of automated welding processes to ensure correct positioning of the welding torch [99]. Other methods of seam tracking utilise arc sensing technologies [97,100]. Arc-sensing relies on the relationship between the variation of the Contact Tip to Work Distance (CTWD) and the electrical arc signals (arc voltage and arc current) [101]. As the welding torch weaves and moves along the weld groove, changes in the distance between the tip of the electrode and the work-piece results in variations in the electrical arc signals. These signal variations can be used to interpret the geometry of the weld groove and update the motion of the welding torch. This is of significance to SAW, where there is no direct access for other vision sensing systems [101]. Ultrasonic sensing has been proposed as an alternative method of seam tracking [102–104], however, this has not seen widespread adoption.

Many weld monitoring techniques aim to imitate the function of human perception by utilising the same external information sources available to a manual welder. The auditory feedback available to manual welders during the process is vital to ensuring their

capability to maintain a high quality weld. The process stability, arc behaviour and droplet transfer mode can all be characterised within the acoustic emissions during welding and directly related to the overall weld quality [105]. Removal of the acoustical feedback to a manual welder has been found to drastically reduce their ability to compensate for changes within the welding process resulting in the formation of defects [106]. The same study found that delaying the acoustic feedback by as little as 400 milliseconds was enough to destabilise the control conditions of the human welders in the trials, resulting in erratic motion. Acoustic emission analysis during welding has, therefore, formed a significant research area in recent years [107]. Low frequency (0 – 100 Hz) air-borne acoustic signals have been used to monitor the generation of unwanted spatter during a GTAW process [108]. Measurement of acoustic signals has also been used to monitor the penetration depth of a GTAW process, with the suggestion made that the information contained in the signals was sufficient to form the basis of a control system [109]. Ultrasonic acoustic emission has also been considered as an information source for in-situ weld monitoring [110,111].

It is well recognised that visual perception is the primary source of information for humans, often receiving priority over auditory and tactile sources [112,113]. The visual information available during welding is key to understanding the stability of the process. Visual monitoring of the weld pool through the use of specialised High Dynamic Range (HDR) cameras is widely adopted within industry with many commercial systems available [114,115]. Figure 2.18 shows a still image taken from a commercial HDR weld monitoring camera during a GTAW welding process.

Figure 2.18. Image from commercial Cavitar welding camera during Gas Tungsten Arc Welding deposition. This image was taken by the author during preliminary tests of a Cavitar vision system.

Vision systems have been used to recognise and track the weld pool [117] and provide quantitative feedback on the weld pool geometry, such as weld pool width [118], length and overall shape and symmetry [119,120]. The surface convexity of the weld pool can also be measured, which is an important parameter for understanding weld penetration [121,122]. Infrared (IR) cameras have been used to monitor the temperature of molten weld pools which can also be related to the penetration depth [123,124].

2.7. Chapter Summary

This chapter has outlined the required background knowledge to fully appreciate and understand the subsequent chapters of this thesis. Various welding processes were detailed to highlight their differences and the variety of processes used within industry. Nomenclature relating to weld joint geometry, fit up and multi-pass welding were introduced along with important information regarding common welding defects and their causes and effects on overall weld integrity. An introduction to NDE techniques is given, providing information relating to a variety of testing techniques used within industry.

Specific emphasis was placed on the understanding of UT, from the basics of ultrasound production and propagation, through to complex beam forming and data presentation methods for PAUT. Finally, an introduction to weld process monitoring is given, highlighting the various techniques currently being researched and those which have made it through to industrial deployment. Finally, an introduction to weld process monitoring is given, highlighting the variety of information sources available which can be used to assist in maintaining correct process parameters. Emphasis is placed on parallels drawn between human operators and automated systems.

The following chapters of this thesis will draw on the fundamentals presented here when discussing the use of ultrasonic inspection techniques during welding for defect detection and process monitoring.

Chapter 3

In-Process Ultrasonic Weld Inspection Challenges and Opportunities

3.1. Introduction

Although most traditional ultrasonic inspections take place at room temperature, as per international standards [125,126], there are many situations where the material under test is at an elevated temperature. This is most common within process industries, such as oil & gas and nuclear, where efficiency is key and in-service and on-stream inspection and monitoring is necessary to prevent substantial losses in productivity and revenue [127–129]. Elevated material temperatures present unique challenges to the way in which ultrasonic inspections are performed.

From a deployment perspective, traditional ultrasonic probes are limited in their capabilities to perform inspections at elevated temperatures. Primarily due to limitations of the bonding materials and the effects of thermal expansion, the maximum tolerated temperature of conventional ultrasonic probes are ~60 °C [127]. This makes them impractical for situations where the material temperature exceeds these limits. Significant

advancements are being made to bring high-temperature ultrasonic probes to market with specialized materials and equipment [128–132].

The effect of temperature on the mechanical and material properties of steel and its alloys has been studied in depth [133–135]. A material's ultrasonic properties are intrinsically linked to its mechanical properties through the elastic constants; Poisson's ratio, Shear Modulus and Young's modulus. Figure 3.1 shows the elastic constants for mild steel for varying temperatures as derived by Scruby et al. [136].

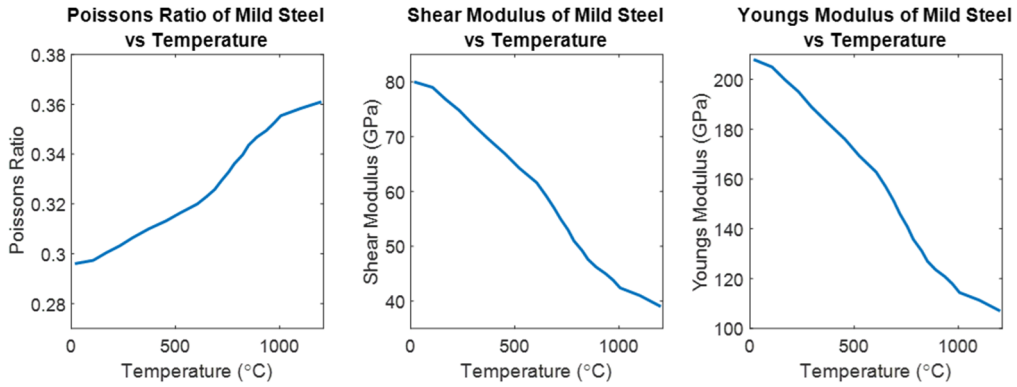

Figure 3.1. Elastic constants of mild steel versus temperature, Poisson's ratio, Shear modulus and Young's modulus [136]

Variations in these elastic constants result in changes to ultrasonic parameters such as attenuation and acoustic velocity [136–138]. Figure 3.2 shows how the longitudinal and shear wave acoustic velocities within mild steel change with temperature as derived by Scruby et al. [136].

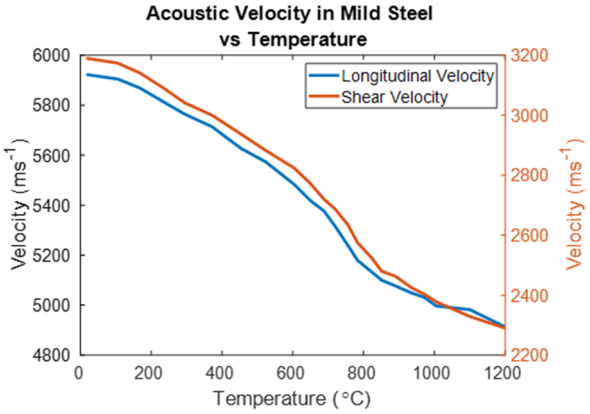

Figure 3.2. Acoustic velocity in mild steel versus temperature for both shear and longitudinal wave modes [136]

In situations where the material temperature is uniform, inspections can be carried out as normal with simple corrections made to the acoustic velocity and compensations made for the increased attenuation expected. However, the presence of thermal gradients within the material, particularly in the case of angled beam inspections, results in complex acoustic refraction where the ultrasonic beam will bend towards higher temperature regions within the material where the acoustic velocity is slower. This effect is shown visually in a simplified manner in Figure 3.3. Furthermore, in the case of PAUT where beam focusing has been implemented, the presence of thermal gradients causes beam defocusing which can affect the resolution and sensitivity of the inspection.

The consequences of these "beam bending" effects for ultrasonic inspection are well documented [132,139–143], resulting in positional misalignment of any potential signals of interest in the order of millimetres [139]. This makes in-process weld inspection a very challenging inspection scenario, as the localized heat source used during welding operations results in harsh thermal gradients within the material.

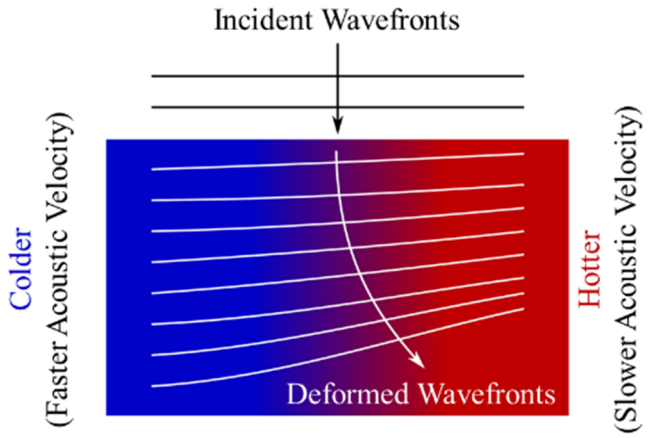

Figure 3.3. Diagram showing beam-bending effects of thermal gradients

The application of in-process ultrasonic weld inspection would likely place the ultrasonic probe as close to the welding torch as possible, while being at a safe operating distance, to inspect the deposited material. In order to overcome the negative effects of the thermal gradients present, it is vital to have an accurate understanding of how the material temperature changes in the inspection plane during welding. This prior knowledge would allow for compensation methods to be developed and applied to correct for the effects of beam bending and ensure that relevant indications are shown in their true position.

Thermal gradients also present challenges for the verification of PAUT inspection systems. Verification is crucial to ensure their accuracy and reliability in detecting flaws within components. Key aspects of the verification process are adversely affected by the introduction of thermal gradients. For example, calibration of phased array probes is necessary to ensure consistent beam angles and focal points. Probe calibration is typically performed at room temperature using reference calibration blocks with known geometries and reflectors [126]. These reference blocks are designed to simulate the conditions and

characteristics of the material under test and often contain artificial reflectors of different sizes, shapes and orientations. The beam bending and defocusing which occurs as a direct result of thermal gradients complicates this procedure, as it is challenging to accurately replicate the thermal gradients present during welding in such reference blocks. Strategies must be developed to limit the number of variables changing during in-process inspection to allow for accurate and repeatable verification of system performance in-process.

In this chapter, thermal models are produced and experimentally verified to accurately model the thermal gradients experienced during a multipass welding procedure. The development of these models has allowed analysis of the thermal gradients experienced during in-process inspection and provide the knowledge needed for thermal gradient compensation, which is discussed in Chapter 4. Furthermore, this chapter also explores the development of a method for introducing repeatable artificial defects into the weld volume. These artificial defects are of known size, shape and location enabling verification of the in-process PAUT weld inspection system developed in Chapter 4.

3.2. Thermal Gradient during Fusion Welding

To accurately understand and quantify the thermal gradients present within a weld joint at varying stages during a multipass welding procedure, Finite Element (FE) models were produced and experimentally verified. The geometry chosen for this study was a 15.8 mm thick carbon steel (S275) butt weld with a 90° included bevel preparation, as shown in Figure 3.4. This weld geometry has been used extensively during previous and subsequent projects and throughout the remaining chapters of this thesis, making it a

practical choice for this thermal analysis [139,140,144,145]. The welding process chosen for these trials was GTAW, as it is a common industrial welding process which is more precise and stable when compared with other fusion welding processes. The welding for this joint comprised a 21 pass, seven-layer procedure as shown in Figure 3.4.

The following sub-sections document the approach taken for the FE modelling and experimental validation respectively. Accuracy of the thermal models was established

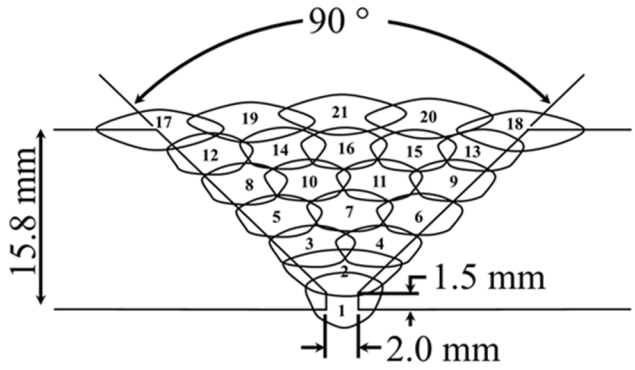

Figure 3.4. Schematic drawing of weld joint geometry highlighting the welding procedure, pass structure and relevant dimensions

through comparative error analysis.

3.2.1. Thermal Modelling

The commercial Finite Element (FE) package COMSOL [146] was used to generate thermal models representative of the GTA welding of the weld joint shown in Figure 3.4. It should be noted that this model is a balance between various complex electrical, mechanical and fluid dynamic interactions, with its primary aim being to better replicate the thermal gradients within the material during fusion welding. Comprehensive modelling of the welding process would require several additional considerations

including but not limited to heat and fluid modelling of the weld pool [147,148], arc-metal interaction [147] and microstructural changes [147,149].

Important information with regards to the geometry of the welded component was collected during welding of the validation component and used to update the thermal models to increase their accuracy. After each weld layer had been deposited, the geometry of the surface was collected using a 2910-100 Micro-Epsilon laser scanner [150]. These scanned geometries were used to generate accurate Computer Aided Design (CAD) models of each layer for the thermal modelling and are shown in Figure 3.5.

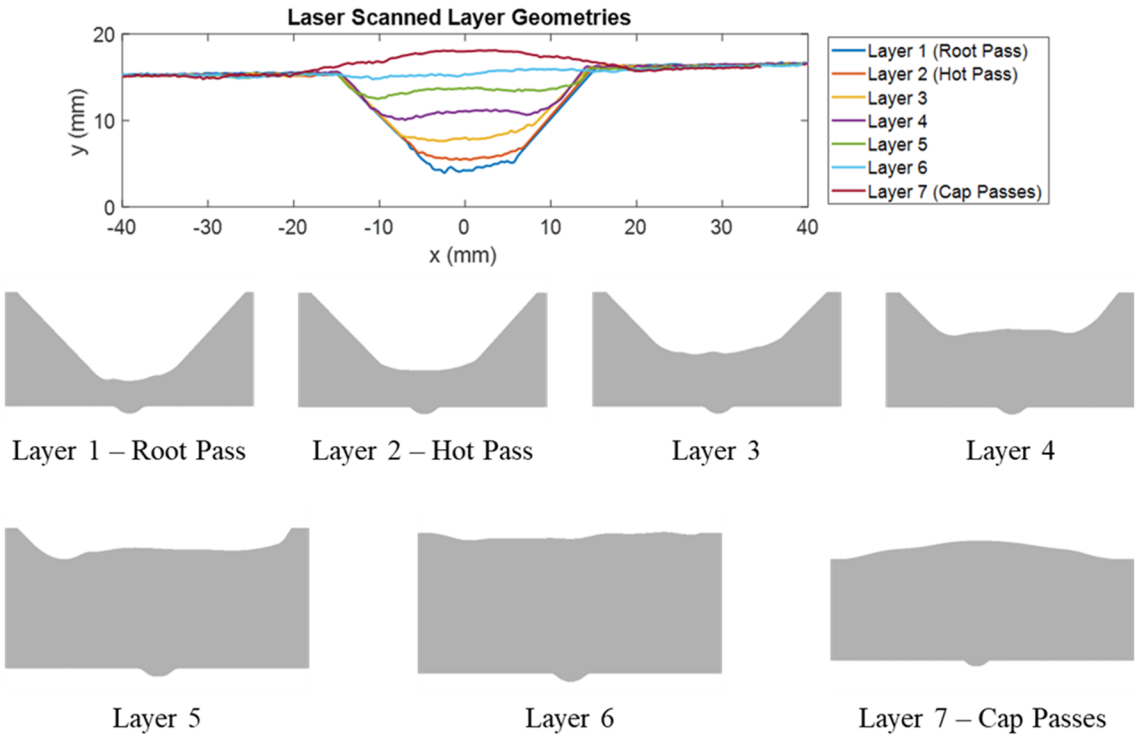

Figure 3.5. Laser profiles of each layer with associated 2D CAD geometries

Each CAD geometry was loaded into a separate thermal simulation, where each model domain was $16 \times 600 \times 400$ mm, comprised of ~ 15,600 tetrahedral elements. An example domain for the simulations is shown in Figure 3.6, with the co-ordinate system and welding path highlighted. An ambient boundary of 20°C was applied at each domain surface where conductive, natural convective and radiative heat transfer occurs. The steel was modelled with a thermal conductivity of $44.5 \frac{W}{mK}$ and a specific heat capacity of $475 \frac{J}{kgK}$, from the COMSOL material libraries.

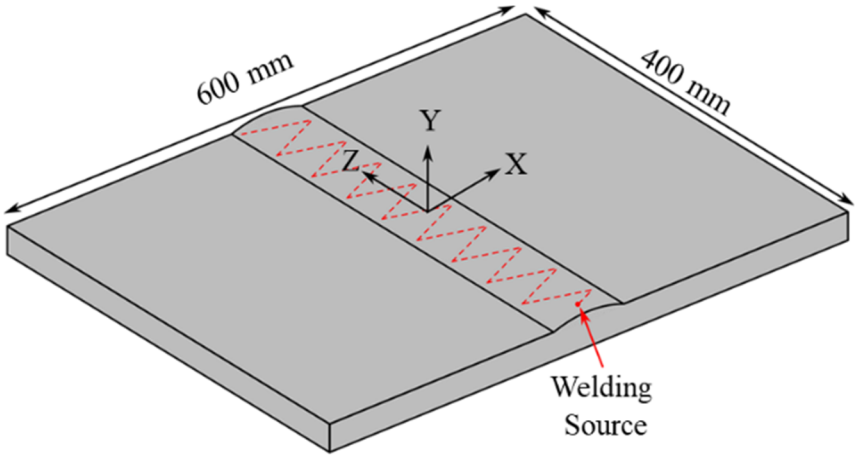

Figure 3.6. Diagram of COMSOL domain for a fully-filled weld with dimensions, co-ordinate system and welding heat source path indicated

The welding heat source within the FE models was modelled as a gaussian heat source [151–154] as defined in Equation (3.1), where φ_q is the heat flux in $\frac{W}{m^2}$, η is the process efficiency, V is the weld voltage, I is the weld current, r_{spot} is the arc radius, r_{focus} is the spatially and temporally dependant centre of the gaussian function, t is time and t_{pass} refers to the time to complete the weld pass. t_{pass} is a function of the linear

velocity of the weld torch and weave frequency and, therefore, will alter for different passes.

$$\varphi_q(x,z,t) = \frac{2\eta VI}{\pi r_{spot}^2} e^{-\left(\frac{2r_{focus}^2}{r_{spot}^2}\right)}, \qquad t < t_{pass} \tag{3.1}$$

Process efficiency is a complex variable dependent on a number of process parameters such as welding current, welding speed, parent material type, type of shielding gas used etc. [155,156]. Previous work has used calorimetric methods to evaluate the process efficiency of different welding processes [155,157] and published arc efficiency values report a wide range, from 0.36 to 0.90 [158–160]. A number of published studies have reduced this range and placed the average to be in the region of 0.77 ± 10% [155,158]. For the purposes of these models, an efficiency value of 0.70 was used and found to be accurate.

The arc spot size, r_{spot}, was determined through analysis of the experimental weld recordings taken using a XIRIS High-Dynamic Range camera. Here, the weld electrode diameter was used as a reference measurement to establish an approximate arc width of 3.0 mm.

With reference to the co-ordinate system indicated in Figure 3.6, equations describing the spatial and temporal variation of the gaussian heat source in dimensions x and z can be formed, given by x_{focus} and z_{focus} in Equations (3.2) and (3.3) respectively.

$$x_{focus}(t) = \frac{2A_x}{\pi}\sin^{-1}\left(\sin\left(\frac{2\pi}{p_x}\right)t\right) + x_{offset}, \qquad t < t_{pass} \qquad (3.2)$$

$$z_{focus}(t) = A_z - \left(\frac{2a_z}{\pi}\cos^{-1}\left(\cos\left(\frac{2\pi}{p_z}t\right)\right)\right), \qquad t < t_{pass} \qquad (3.3)$$

x_{focus} is a triangular waveform which describes the weaving of the weld torch in the x direction over time. The weave of the torch is described by its amplitude, A_x, and oscillation period, p_x, which correspond to welding variables used during the experimental validation. x_{offset} was used to adjust the central x position of the weave for scenarios where the weld pass is off-centre with respect to the centre of the weld preparation. z_{focus} is also a triangular wave used to describe the linear progression of the weld torch in the z direction over time. The amplitude of this triangular wave, A_z, corresponds to the maximum and minimum z displacements while the period, p_z, was set to be double the pass time, t_{pass}. The movement of the weld torch in x and z is shown in the diagram in Figure 3.6. x_{focus} and z_{focus} contribute to the vector sum, r_{focus}, given by Equation (3.4).

$$r_{focus}(x, z, t) = \sqrt{\left(x - x_{focus}\right)^2 + \left(z - z_{focus}\right)^2} \qquad (3.4)$$

With all of the welding parameters defined as per the experimental validation given in Section 3.2.2, each model was run for double the time of a weld pass to observe how the thermal gradient changed within the domain during and after welding as the substrate cools.

Figure 3.7 shows the final 3D thermal model for layer 7 of welding, highlighting the shape of thermal dissipation behind the welding heat source. For clarity, the

temperature colour scale has been restricted to below 500°C although the maximum temperature extends to 4800°C in the centre of the gaussian heat source.

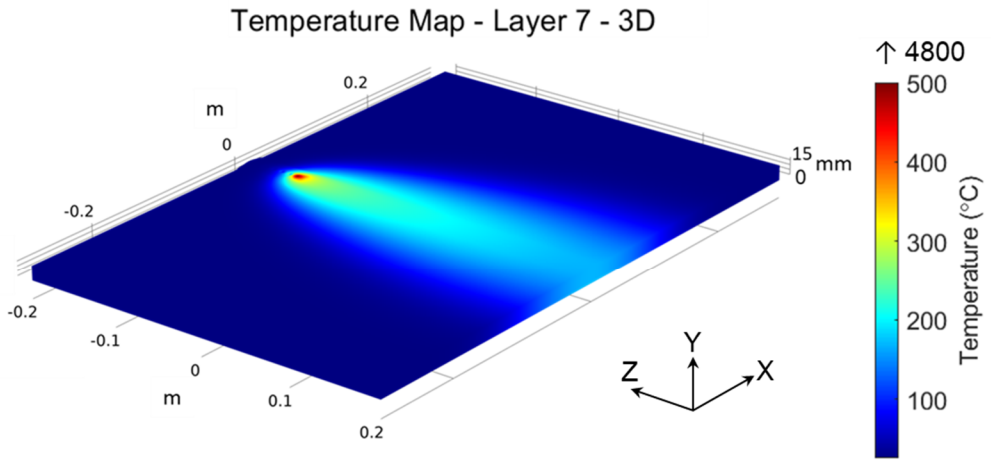

Figure 3.7. 3D temperature map taken from thermal model for layer 7 of welding showing dissipation of heat behind welding heat source

3.2.2. Experimental Validation

Experimental validation of the simulations was carried out in parallel, to provide the appropriate information to the thermal models, including the initial domain temperatures and geometries.

Two steel plates with the same dimensions and joint geometry as used in the modelling were welded, as shown in Figure 3.8a [139]. The pass structure of the welding procedure is shown again in Figure 3.8b for convenience. Pass 1 and 2 refer to layers 1 and 2 respectively, while passes 3-4, 5-7, 8-11, 12-16 and 17-21 refer to layers, 3, 4, 5, 6 and 7 respectively.

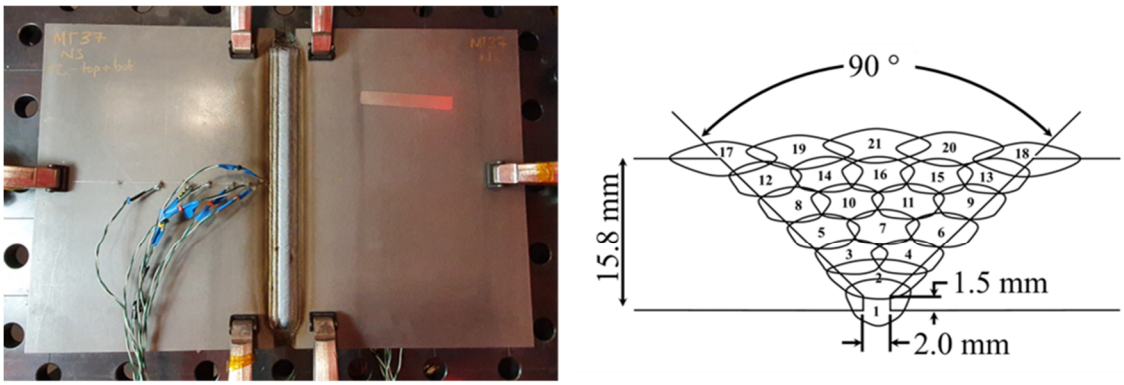

Figure 3.8. (a) A photograph showing completed welded assembly [139] and (b) a schematic of the joint geometry highlighting the welding pass structure

A robotic cell as described in previously published work was used to perform the welding [161,162]. Figure 3.9 shows the robotic cell hardware, while Figure 3.10 shows the high-level architecture and flow of data between components. The National Instruments (NI) cRIO 9038 real-time controller was the building block for control of the hardware components shown [162]. A KUKA KR5 robotic manipulator was used to facilitate GTAW using a JÄCKLE/TPS ProTIG 350A AC/DC welding power supply. A 2910-100 Micro-Epsilon laser scanner is fitted to the welding head to capture weld geometry data after each layer of weld, while a XIRIS XVC 1100 high dynamic range camera is used to provide visual feedback of the welding process. This robotic cell was configured to allow both robotic welding and inspection, however the inspection capability was not required for these experiments.

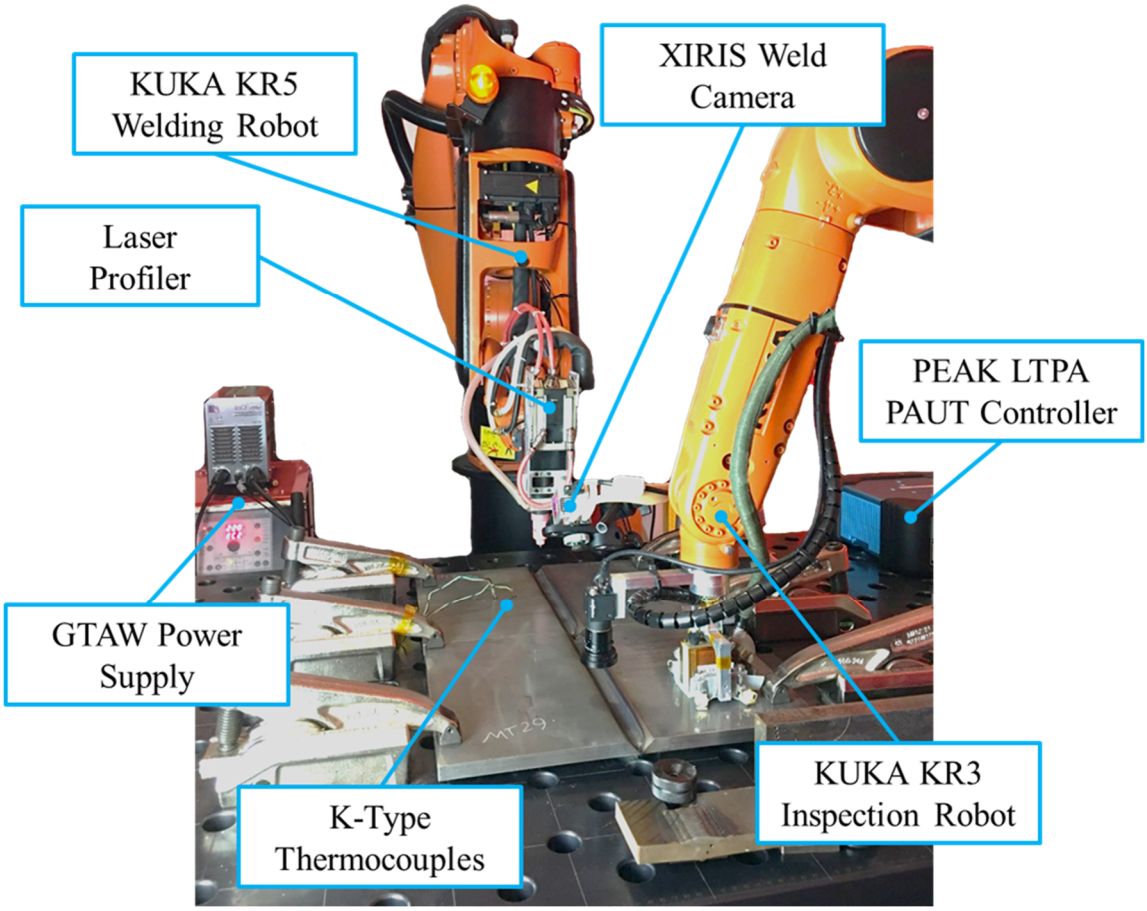

Figure 3.9. Robotic welding cell hardware showing robotic welding head with additional laser profiler and HDR camera, GTAW power supply, thermocouple attachment for temperature monitoring and NDT robotic deployment.

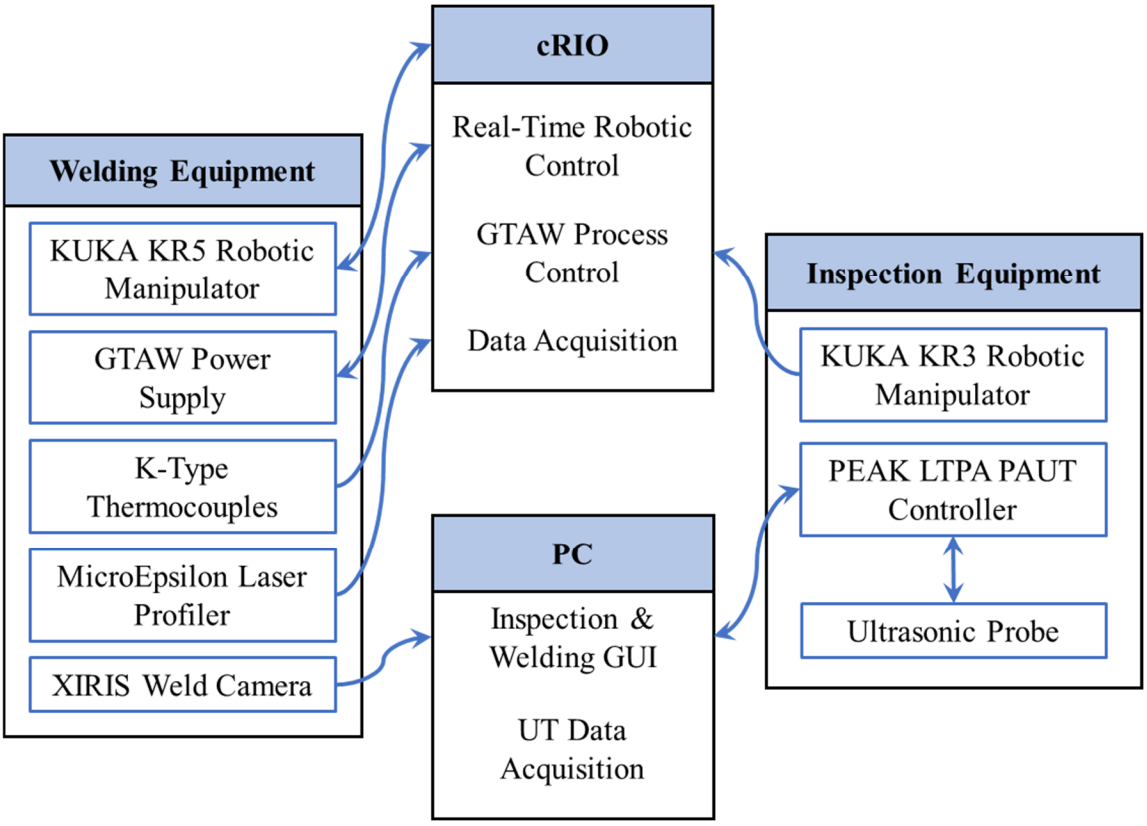

Figure 3.10. Robotic welding and inspection cell block diagram with data flows highlighted

To monitor the temperature distribution and give points of comparison to validate the thermal models, 13 K-type thermocouples were attached to the plates prior to welding. Seven were attached to the upper surface of the left-hand plate and six were attached to the bottom surface of the right-hand plate as shown in Figure 3.11. The data from these thermocouples was logged through the NI 9214 Thermocouple Module at 1 Hz frequency throughout welding of the final pass within each layer and for a period after the welding had finished to a total of 380 s. It should be noted that during welding,

thermocouple 13 became detached from the plate surface and could not be reattached, therefore no readings were collected for this thermocouple.

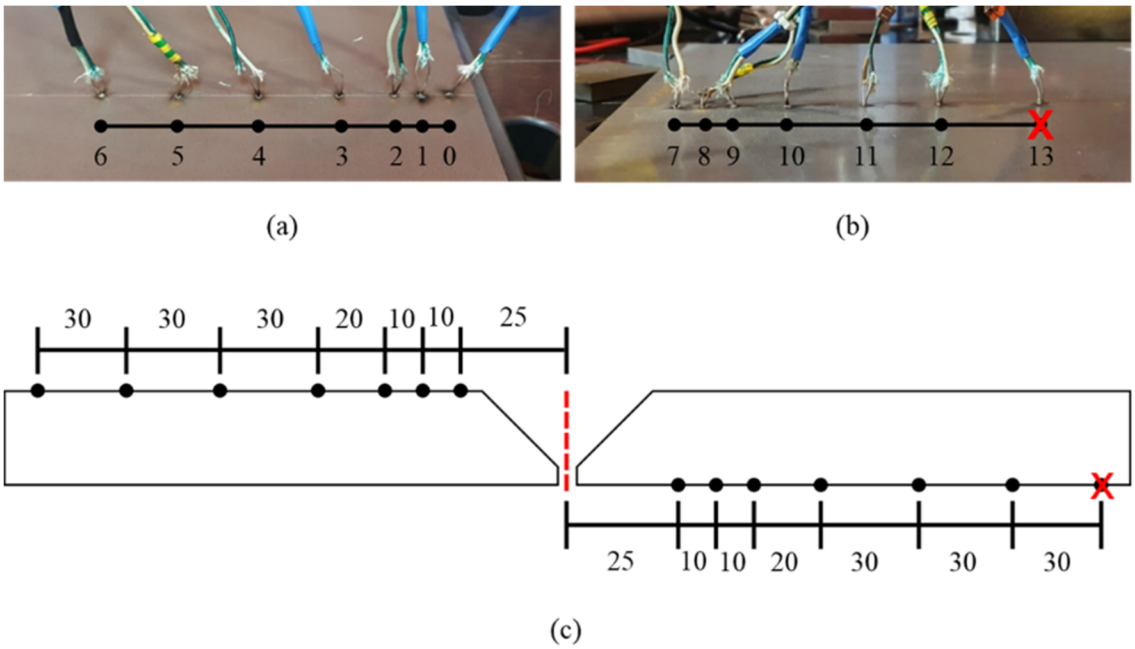

Figure 3.11. Thermocouple placement on (a) top surface of left-hand plate and (b) bottom surface of right-hand plate. (c) Thermocouple placement measurements taken from centre of weld preparation in millimetres (not to scale). [139]

The welding procedure, including all welding parameters, is given in Table 3.1.

*Table 3.1. Welding Parameters *Arc Voltage Control (AVC)*

Pass Number	AVC* (V)	Current (A)	Travel Speed (mm/min)	Wire Feed Speed (mm/min)	Weave Amplitude (mm)	Weave Frequency (Hz)
1	12	120	50	910	2	0.3
2	13.5	220	100	1225	4	0.6
3 to 16	13.5	210	120	1470	3	0.55
17 to 21	13.5	240	100	1225	4	0.6

After deposition of each layer, the plates were allowed to cool until a consistent temperature throughout the component was reached, taking on average a period of 1.0 to 2.0 hours. A uniform temperature was confirmed both by continuous monitoring of the thermocouple outputs and with a contact thermocouple at multiple points on the plates surface. The starting temperature after each layer was also fed back in to the thermal simulations to increase their accuracy.

3.2.3. Results

The simulation and experimental data could be compared directly by extracting temperature data from the COMSOL simulations at points corresponding to the placement of the thermocouples in the experiment (see Figure 3.11). Comparisons of thermocouples for various layers are shown in Figure 3.12. Full comparison results for each layer are

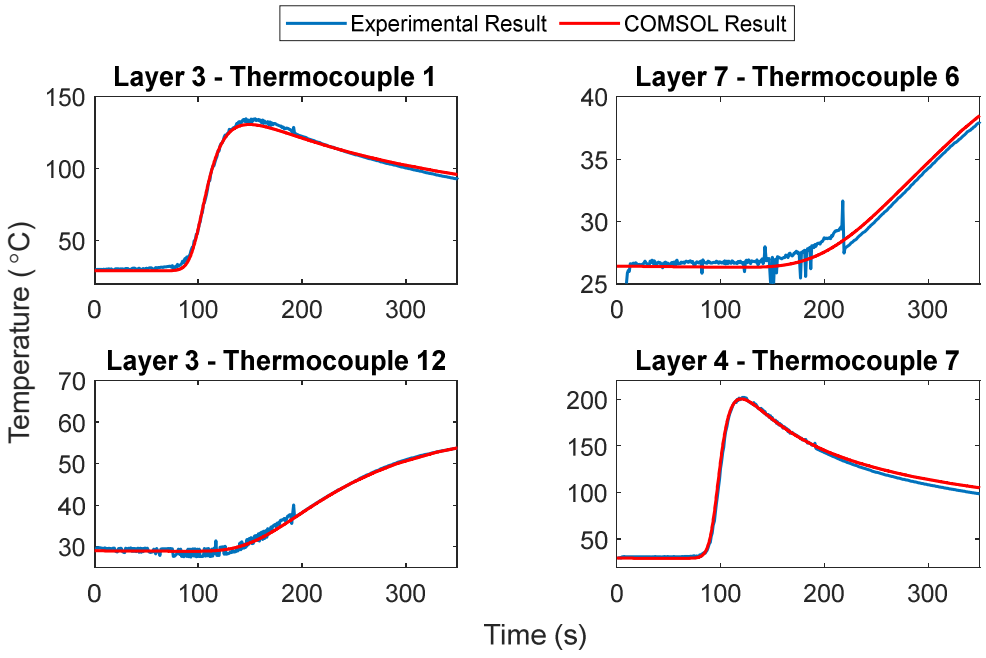

Figure 3.12. Comparison of experimental and COMSOL data for thermocouples for various layers and thermocouple numbers

given in Appendix A. Some noise is present in the experimental data as a result of the high frequency component of the welding process and is therefore only visible during the period where the welding process is active.

Some variation in these datasets is expected due to the inherent variability in the experimental process. For example, there may be slight differences in the material properties between the experiment and simulation. During welding, the Arc Voltage Control (AVC) value was altered instinctively at various points to maintain a high quality weld, which is difficult to recreate in a simulation environment. The effects of experimental variability are seen most clearly in the comparison results of thermocouple ten, shown in Figure 3.13. Thermocouple ten consistently read lower than the COMSOL result for all layers, despite all other thermocouple readings being in strong agreement with the simulation. This could indicate an error in the placement the thermocouple or a poor connection formed during the mounting process (spot welding). Although great care was taken to mount the thermocouples in exact positions, there is likely some positional error involved. For this reason, thermocouple 10 was discounted from any further analysis.

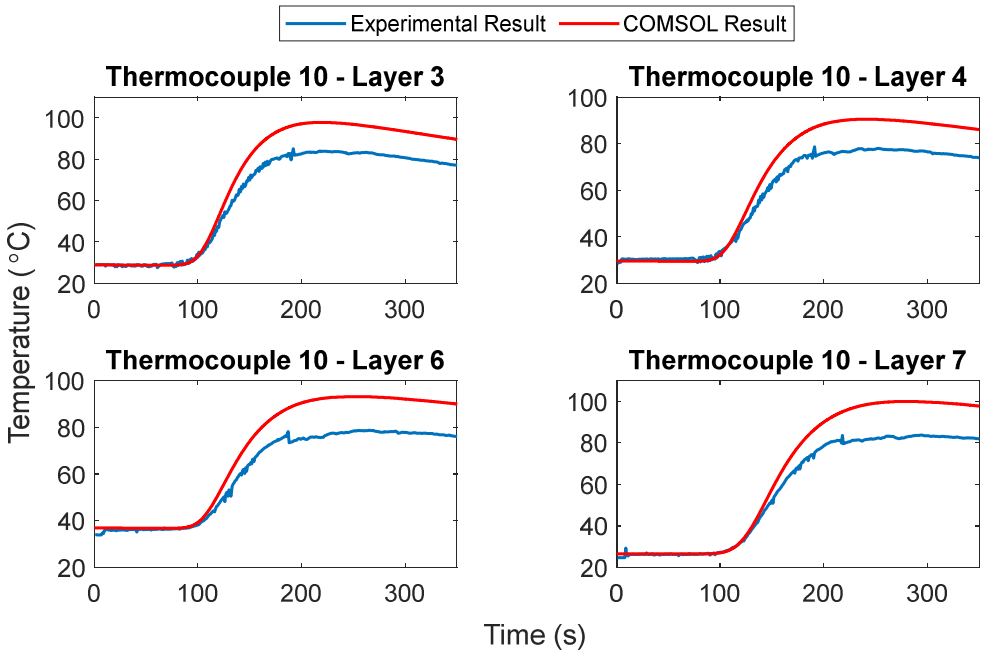

Figure 3.13. Comparison of experimental and COMSOL results of thermocouple 10 for various layers

Error analysis of these results confirmed strong agreement between the simulation and experimental results. Absolute and percentage errors for each thermocouple were calculated for all data points in the time series. Percentage errors were calculated using Equation (3.5). Where the true value is taken as the experimental result.

$$\%\ error = \frac{\overline{(simulated\ value - true\ value)}}{true\ value} \times 100 \qquad (3.5)$$

The results from the error analysis of layer 3 are shown in Table 3.2. The measurement error associated with the K-type thermocouples used is ±2.2°C or ±0.75%, whichever is greater [163,164]. These results show the largest errors correspond to the two thermocouples closest to welding groove (thermocouple 0 and 7). Since data is collected throughout the entirety of the welding process, this includes the point where the weld pool is directly in line with the thermocouple positions. This is the point where the

maximum temperature readings were collected and where this maximum error occurs. As previously stated, these models are not intended to be accurate in modelling the weld pool itself and therefore the temperature gradient in the plane bisecting the weld pool is likely to be the least accurate. Calculated error values for all subsequent layers are given in Appendix A.

Table 3.2. Error analysis - layer 3

Thermocouple Number	Maximum Absolute Error (°C)	Average Absolute Error (°C)	Maximum % Error	Average % Error
0	14.70	4.57	17.71	4.36
1	5.80	1.76	15.47	2.90
2	6.89	2.14	9.50	2.88
3	7.00	2.26	8.60	3.66
4	5.21	1.45	10.00	3.29
5	3.22	0.93	8.70	2.75
6	2.42	0.61	7.52	2.06
7	12.68	2.69	12.98	2.72
8	8.96	1.82	11.50	2.06
9	4.44	2.16	6.91	2.50
11	2.59	0.79	5.40	1.95
12	3.37	0.60	8.43	1.87

From these validated models, cross-sectional temperature maps were extracted from planes at varying distances from the welding heat source (datum), as shown diagrammatically in Figure 3.14.

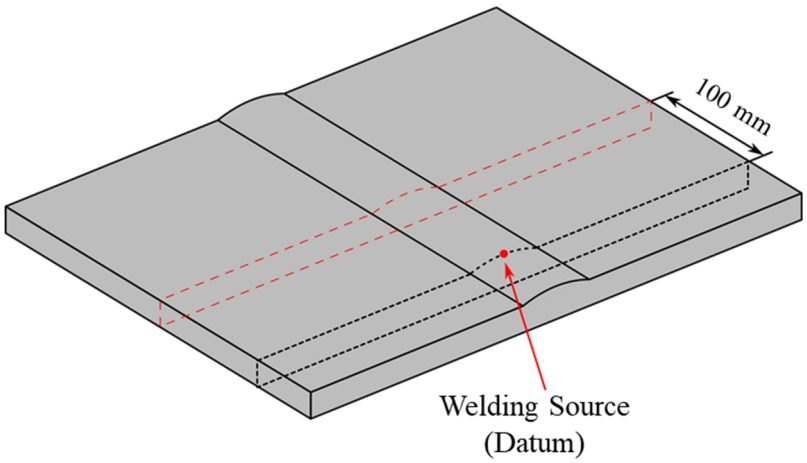

Figure 3.14. Diagram indicating cross-sectional temperature maps taken with respect to a datum point (welding heat source)

Examples of these temperature maps are shown in Figure 3.15. Figure 3.15a and Figure 3.15b illustrate how the thermal distribution changes for the final weld layer for inspection planes at varying distances behind the welding heat source. The thermal distribution is seen to change rapidly from a highly localised region to an almost one dimensional gradient within the inspection plane as close as 110.0 mm behind the welding heat source. Figure 3.15c illustrates the thermal distribution for the final pass within layer 3 of welding. The thermal distribution can be seen to be skewed to the right, which is realistic given that the final pass in layer 3 includes an offset in x.

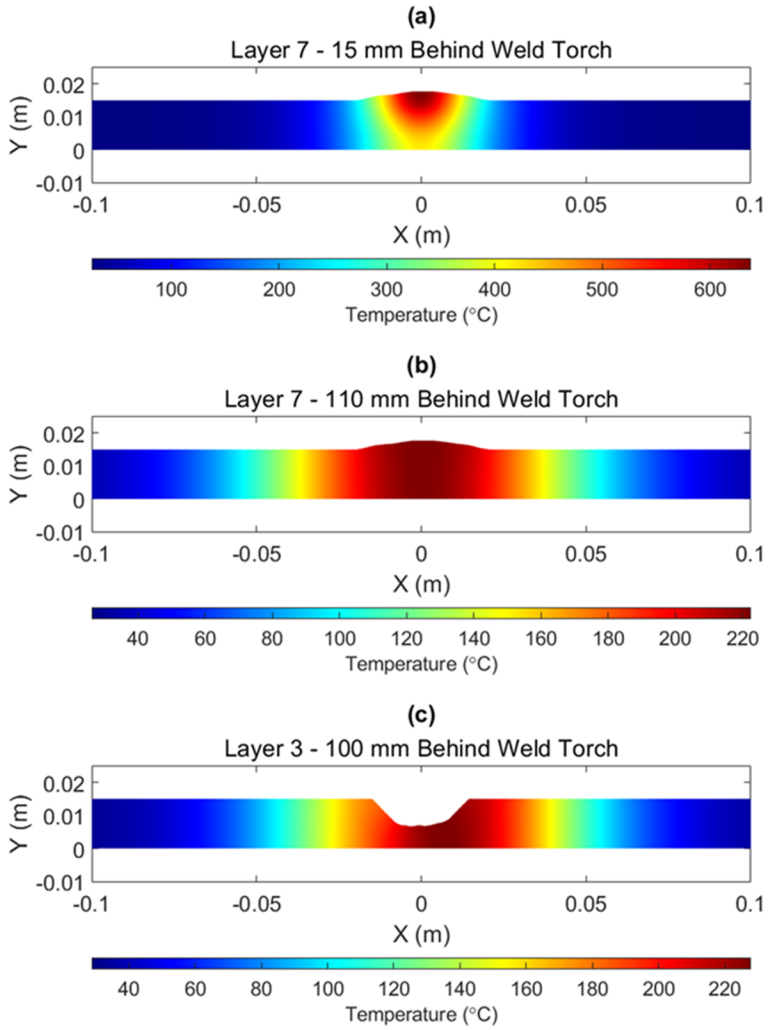

Figure 3.15. Temperature maps taken from experimentally validated COMSOL models showing cross sections taken through various planes relative to the heat source. (a) Layer 7, 15 mm behind datum, (b) Layer 7, 110 mm behind datum, (c) Layer 3, 100 mm behind datum

The development of these thermal models has provided vital information regarding the thermal gradients experienced during in-process weld inspection. Furthermore, these validated results have been used to develop compensation techniques to counteract the negative effects of thermal gradients within the inspection volume during in-process weld inspection. These thermal maps have been used in conjunction with the

well-defined material properties of steel with respect to temperature to develop a novel compensation strategy for TFM imaging of welds in the presence of thermal gradients [165]. Real-time PAUT imaging compensation methods utilising these thermal maps as the required prior knowledge have also been developed and are discussed and analysed in more detail in Chapter 4.

3.3. In-Process Weld Inspection Defect Verification Strategies

As previously discussed, a robust method for verifying the performance of an in-process PAUT inspection system must be developed to overcome the challenges associated with thermal gradients. This method must be flexible yet repeatable, producing defects of known size and location, to eliminate as many changing variables as possible.

3.3.1. Artificial Defect Embedding Strategies

The manufacture of specimens with artificial or intentionally embedded defects is common. Such specimens are employed for training to ensure that students are exposed to a wide variety of flaws during their training. In this educational scenario, it is vital that these artificial defects are representative of any real defects which will be encountered by students during their future career. These specimens are also useful for the development of new NDE techniques and qualification of testing procedures. There are various methods utilised within industry to manufacture reference test pieces, the most common of which are discussed below.

Real defects can be cut from previously operational components, inserted and welded into position within a new test piece [166,167]. With this method, there is flexibility in the types of defects which can be inserted and they are sure to be representative of real defects. However, ensuring a cohesive and continuous union between the test material and defect insert can be challenging. This can impact the effectiveness of the test piece for training purposes, as the mismatch between the insert and parent material can create artefacts indicating the presence of the insert and influencing the response obtained during inspection.

Deliberate alterations to the welding procedure (current, voltage, torch position etc.) can be made to induce real defects such as LOF, porosity and inclusions [166]. Material changes can also be made to better facilitate the formation of cracks i.e. using a hard-facing filler wire to increase brittleness within the weldment [140]. A significant disadvantage of this approach is that it is difficult to predict the size, shape and morphology of the resultant defect.

Representative defects can be obtained through machining, typically through spark erosion or Electrical Discharge Machining (EDM) [168,169]. Machined defects have the advantage of being highly controllable to obtain the desired dimensions. However, the performance of these types of machined defects in comparison to the real defects which they are representing is low. For example, EDM notches can be used to represent surface breaking cracks, however, they lack the complexity of a true crack's morphology. It is difficult to create EDM notches with the same branching, roughness and narrow width as would be expected with an real crack [170,171].

As an alternative to EDM notches, fatigue and heat cycling can be used to recreate representative in-service crack defects [166,172,173]. Often these methods require a slot to be added to the component to facilitate the formation of a crack in a specified place. The crack can then be generated through a sequence of heating and cooling cycles or through fatigue cycling [166].

When considering verification of an in-process NDE system, a flexible yet repeatable method for generating defects of known size, geometry and location at various stages of manufacture is vital. Machining of defects, while offering repeatability in terms of the defects shape and dimensions, is not practical in this scenario. While it is possible to machine a notch within lower layers of a multi-pass weld and cover it to create a sub-surface defect, it is challenging to then predict its final dimensions. Therefore, it is necessary to embed defects at the point of manufacture. Previous work has looked at inserting tungsten artefacts within the weldment [174]. Given tungsten's high melting point (~3414°C [175]), tungsten rods and balls can be inserted within the weld volume during welding without melting, to provide acoustic reflectors [174,176]. Further development of this technique resulted in a repeatable method for inserting tungsten tubes within the weld volume [145,177]. The tubes provide a volumetric air gap within the weld volume of known position, length and diameter, acting in the same manner as a SDH.

3.3.2. Tungsten Tube Embedding Procedure

The process for inserting tungsten tubes to act as ultrasonic reflectors within the weld volume consists of four main steps. This process is shown as a flow chart with accompanying photographs in Figure 3.16. First, a slot is machined within the weld volume in the desired place to fit the length and diameter of the tungsten tube snugly. The tungsten tube can then be fitted, with the addition of iron powder to fill any spaces left within the slot. The iron powder fuses during welding to eliminate air gaps which can interfere with the acoustic reflection. However, emphasis is placed on machining the slot to provide a close fit to reduce the volume of these air gaps as much as possible. The placement and orientation of the tungsten tube can be altered to replicate the position of various defects, i.e. LOSWF. Tack welding the tungsten tube in place prevents any unwanted movement during welding to maintain the desired position and orientation. This is especially important for fitment within pipe specimens where rotation of the pipe can cause the tube to become dislodged. Welding can then continue as per the welding schedule to completely cover the tungsten tube.

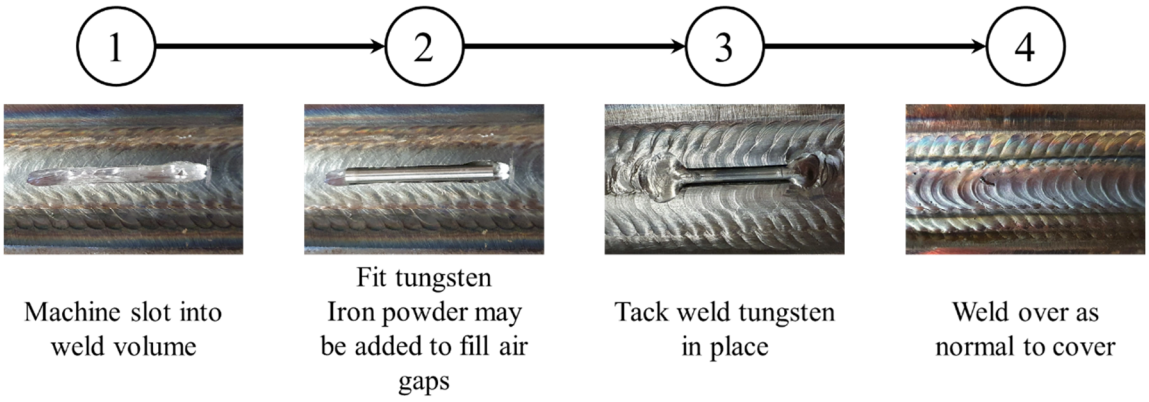

Figure 3.16. Artificial defect insertion process flow chart

3.3.3. Results

To analyse the effectiveness of this embedding process, completed welds were first ultrasonically tested, to ensure detection capability. Figure 3.17 shows the results of ultrasonic testing on an embedded tungsten tube with dimensions of 1.0 mm Internal Diameter (ID), 2.9 mm Outer Diameter (OD) and length 30.0 mm, placed in such a way as to replicate the placement of a LOSWF type defect. The resultant signal shows a clear acoustic response from the embedded defect with high Signal-to-Noise Ratio (SNR) of 35 dB. The response is specular and smooth as expected from a smooth, consistent air gap within the weld material, suggestive of complete fusion between the tungsten tube and the weld material.

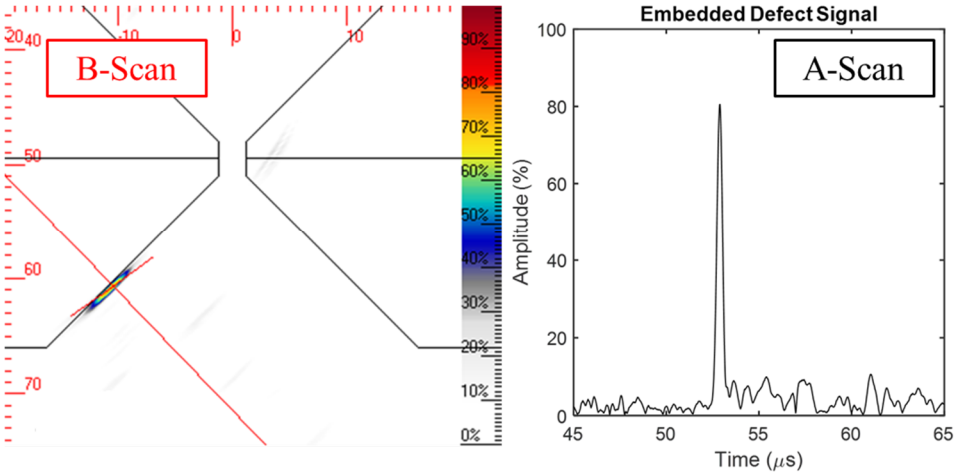

Figure 3.17. B-Scan (left) and A-scan (right) of embedded tungsten tube defect taken during cold ultrasonic testing for verification

To confirm fusion of the tungsten tube with the weld volume, completed welds were destructively examined [145]. Welded samples were divided and macrographs prepared of sections including the embedded tungsten tubes. Figure 3.18 [145] shows the resultant macrograph of a tungsten tube placed centrally within the weld volume. Subsequent microscopic examination, also shown, indicates complete fusion of the

tungsten pipe to the surrounding material without any dimensional change. In this sample, iron powder was added to fill small unwanted air gaps present underneath the tungsten pipe. This technique was found to be successful as all three materials (tungsten, iron powder, weld) can be identified through microscopic examination and are seen to be completely fused.

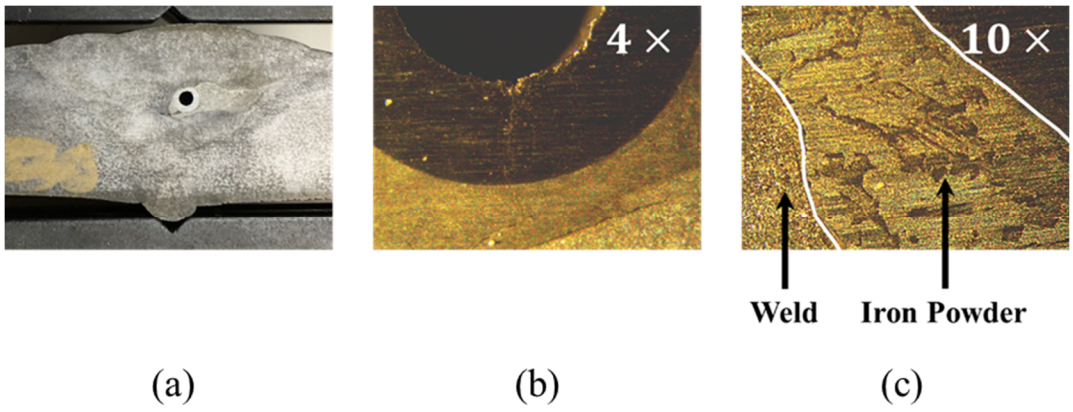

Figure 3.18. Destructive examination of welded sample with embedded tungsten tube including (a) macrographic and (b), (c) microscopic investigations [145]

3.4. Chapter Summary

This chapter has highlighted the challenges associated with the deployment and verification of in-process PAUT weld inspection systems due to the thermal gradients experienced during welding. Developing a robust understanding of these challenges and methods to overcome them was vital to the development of the PAUT inspection and monitoring systems discussed in subsequent chapters of this thesis (Chapter 4 and 5).

Thermal models were developed to gain a better understanding of the changing thermal gradients produced by a GTAW process on a relevant weld joint geometry. These models were experimentally validated to ensure their accuracy and the resultant

temperature maps obtained are used in Chapter 4 for the development of thermal gradient compensation strategies.

Additionally, a new method for producing artificial defects of known size, shape and position was introduced and implemented, which is vital to be able to verify the performance of an in-process ultrasonic weld inspection system as discussed in Chapter 5.

Chapter 4

In-Process Ultrasonic Phased Array Inspection During Fusion Welding

4.1. Introduction

High-integrity fabrications often found in the Nuclear, Defence and Energy sectors commonly require thick section multi-pass welds when joining multiple components together. Traditionally, the manufacture and inspection of these joints are performed as entirely separate processes which limits productivity and fabrication throughput along with increasing re-work when defects are detected post-build. There are, therefore, several tangible commercial and economic benefits which may be realised by introducing in-process inspection directly into the welding process.

As previously discussed, the welding environment poses significant challenges for traditional UT inspection hardware and imaging approaches. In general, material surface temperatures experienced in the region surrounding an active welding process far exceed the operating range of most contact ultrasonic inspection systems, especially when considering that many industrial components are subject to pre- and post-weld heat

treatments [178,179], which can be in the region of 200 °C or higher. Therefore, it is important that inspection sensors can tolerate these temperatures without negative effects. Furthermore, liquid coupling between the sensor and component, as is required for traditional UT, is not a viable option during in-process inspection as any liquid or gel couplant near the weld site runs the risk of contamination and the introduction of gross defects, such as porosity [143]. In this scenario, a non-contact inspection method could be leveraged.

Vision systems are used extensively within industry for weld monitoring and have been used for automatic inspection of welds, using feature extraction and, in some cases, machine learning to provide defect classification and sizing [180,181]. However, vision systems are only able to provide information on surface breaking defects and require direct line of sight to the weld which is not possible for some welding processes, such as SAW. A volumetric inspection technique would, therefore, be advantageous.

Laser Ultrasonics (LU) is a non-contact NDE method for the inspection of welded components [182,183]. Recently, there has been significant research into the use of Laser Induced Phased Arrays (LIPAs) as an alternative to traditional PAUT systems [184,185]. Laser ultrasonic systems require stringent safety measures to be in place for deployment within production environments and are currently significantly more expensive than conventional contact UT systems [186]. SNR for LU systems is also low when compared with contact UT alternatives [187].

Extensive research and development has been undertaken in recent years to implement ultrasonic inspection of multi-pass welds during deposition, to provide real-

time defect detection whilst the welding process is active. Initial developments utilised traditional liquid-coupled PAUT techniques to provide in-process weld inspection [143,188,189]. The inspection was performed after the deposition of a weld pass and while the material remained at temperatures in excess of 100°C. A novel PAUT NDE sensor has been developed to progress towards sensor deployment during weld deposition [132]. The high-temperature compliant roller-probe was found to be successful in detecting intentionally embedded defects in a multi-pass weld where the inspection was carried out between the deposition of each pass. However, this inspection system still required the use of liquid coupling to the surface of the component, making it inappropriate for use during welding.

When considering the aim of reducing bottlenecks and improving productivity, it is important to note that NDE of welds is still commonly performed manually, which is time-consuming, expensive and relies predominantly on the availability of highly-skilled operators. Automated deployment of inspection brings increased accuracy and repeatability of measurements [190,191], especially in cases where the inspection procedure is recurring and consistent. Removing manual operators from dangerous and hazardous environments such as those found during welding is a further incentive for automated inspection deployment [192].

The development of an in-process weld inspection system can be separated into three main research areas: (i) the sensor, (ii) the deployment strategy and (iii) the imaging algorithms. The requirements for each are dictated by the operating environment and associated challenges as shown in Figure 4.1.

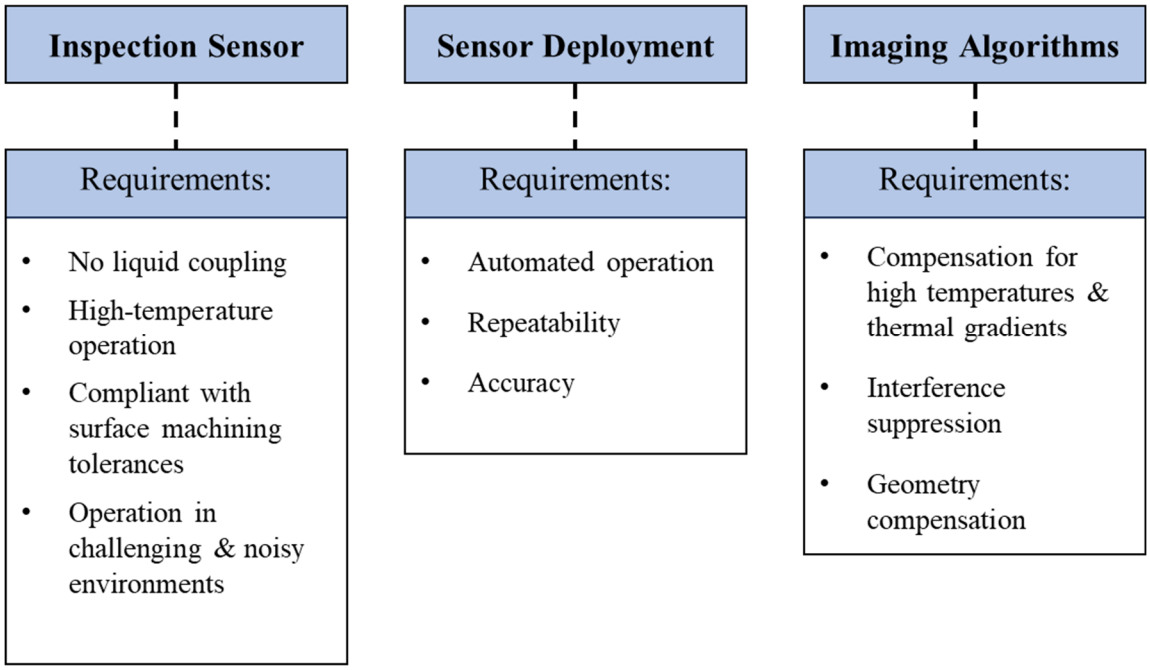

Figure 4.1. Block diagram indicating necessary components of an in-process weld inspection system. These requirements were established and co-developed with industrial partners to ensure their relevance for industrial deployment.

In this chapter, new sensor hardware, deployment strategies and novel imaging algorithms enable, for the first time, continuous PAUT during fusion welding. A high-temperature compliant automated weld inspection roller-probe is deployed alongside imaging algorithms to compensate for the effect of negative process parameters such as temperature gradients, partially-filled groove reflectors and Electromagnetic Noise Interference (EMI). The effectiveness of these imaging algorithms is evaluated and quantified. Results of this work are presented on carbon steel pipe demonstrators with intentionally embedded defects. The SNR of the imaging and inspection system is measured, evaluated and compared against traditional PAUT techniques. The in-process inspection system developed here shows SNR values comparable with that of traditional post-weld ultrasonic testing techniques, showing an average SNR value of 31.21 dB.

4.2. High Temperature PAUT Roller-Probe Sensor

The automated inspection of welded components during welding requires the use of specialised PAUT equipment. Previous work has developed a phased array ultrasound roller-probe for the inspection of welds [132,193]. This advanced roller-probe is configured to have a 5 MHz, 64-element piezo-composite linear phased array probe with 0.5 mm pitch to perform angled weld inspection using shear waves around a nominal refracted angle of 55°. The assembled roller-probe is shown in Figure 4.2.

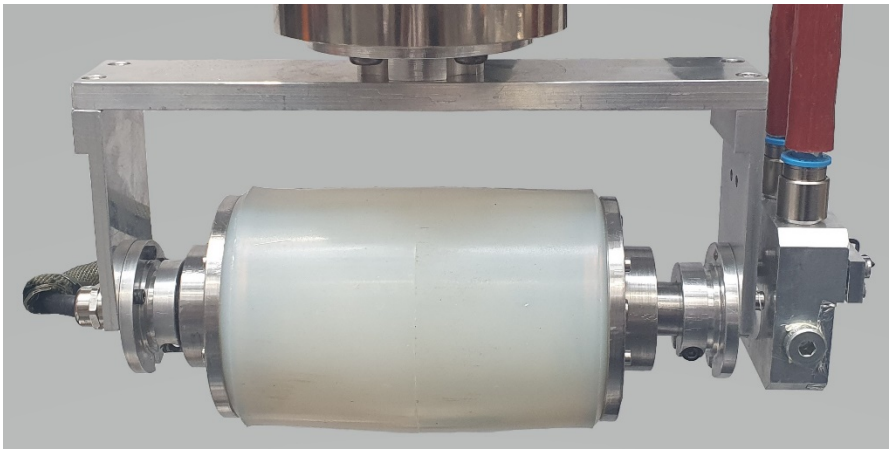

Figure 4.2. PAUT roller probe

As previously discussed, one of the key operating challenges related to the deployment of this hardware is the temperature limitations imposed by the use of ultrasonic arrays. The following sub-sections explore the approach undertaken to first understand the temperature limitations of the PAUT roller-probe and then the development of additional hardware to extend the operational duty-cycle through the addition of active-cooling.

4.2.1. Passive Operation Temperature Benchmarking

In order to better understand the effects of component surface temperature on the roller-probe itself, a thorough investigation of the temperature distribution within the roller-probe was conducted. The internal temperature distribution and inspection cycle of the roller-probe when traversing a heated surface was examined experimentally. A thermistor carriage was mounted to the roller-probe's internal chassis. This thermistor carriage was manufactured from a high-temperature polymer and contained seven immersion thermistors, which were bonded using precision water-resistant, conductive adhesive and calibrated. Internally, this carriage was positioned such that the thermistors were aligned to the vertical, central plane of the roller-probe to monitor the internal temperature distribution.

An experimental testbed was developed, as shown in the schematic of Figure 4.3, comprising the roller-probe with the thermistor carriage mounted to a six-axis KUKA KR10 R1100 articulated robot and a base plate placed over two ceramic heating blankets. The heating blankets were externally controlled through a closed-loop temperature controller. The robotic motion was programmed to perform a continuous back-and-forth motion across the heated base plate (1m length) at a velocity of 1.6 mm/s while the temperature of each thermistor was recorded at 2.0 Hz acquisition frequency. An internal temperature threshold of 55°C across all thermistors was set which, if exceeded, triggered the robot to retract the roller-probe to a safe position.

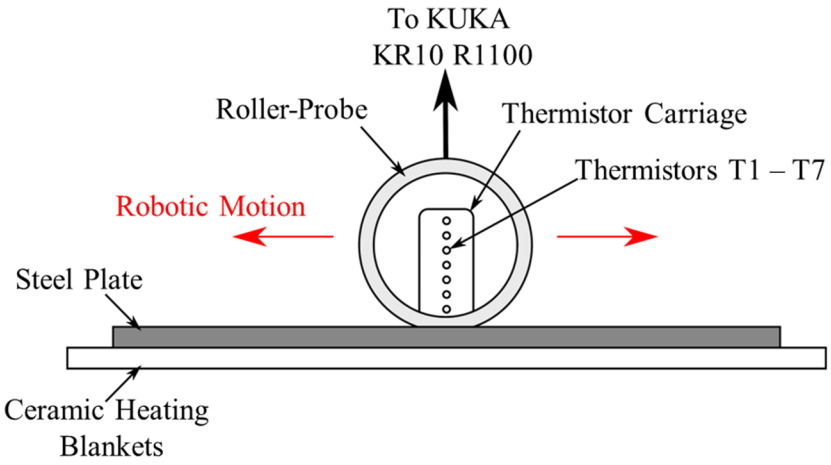

Figure 4.3. Experiment sectional schematic for PAUT roller probe passive operation temperature benchmarking

The duty cycle of the roller-probe was evaluated for five base plate temperatures between 150°C and 350°C. Figure 4.4 shows a plot of the mean internal temperature of the roller-probe against time for each base plate temperature. It was observed that the roller-probe could perform continuous travel for 32 minutes and 30 seconds before reaching the transducer operating limit of 50°C when the base plate was uniformly heated at 150°C. As expected, the inspection window decreased as the base plate temperature was raised, with a maximum inspection window of 11 minutes and 51 seconds with a base plate temperature of 350°C. These duty cycles are not sufficient for continuous inspection of industrial work pieces where the active weld time can be multiple hours.

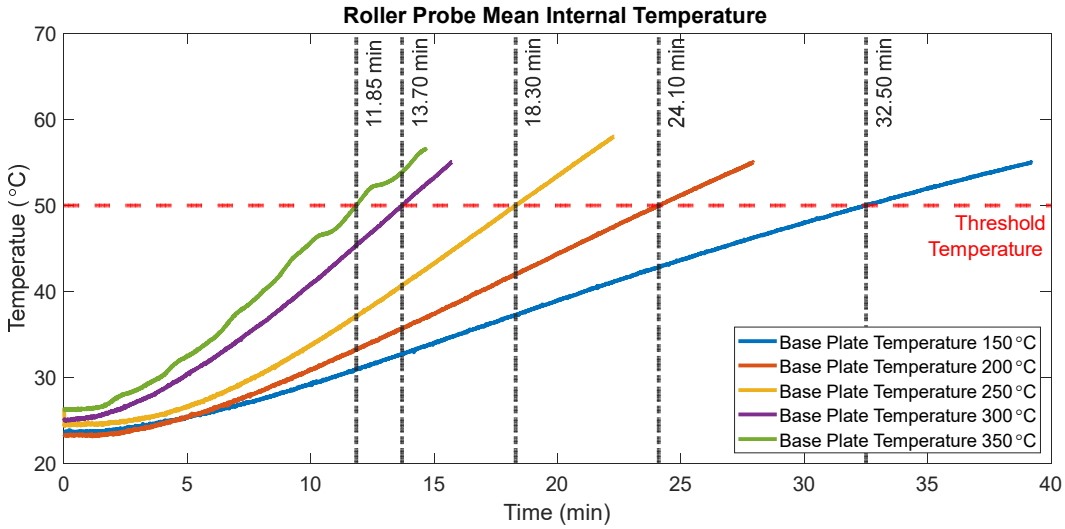

Figure 4.4. Mean internal roller probe temperatures for various base plate temperatures

4.2.2. Sensor Active Cooling

To ensure the safe operation of the NDE system, the internal temperature of the roller-probe must not exceed the operating limit of the ultrasonic array. One option for maintaining hardware devices within specific temperature operating ranges is active cooling, a technique which is common in industries such as welding (weld torches), computers (graphical card heatsinks) and optoelectronics (lasers) [194,195]. Active cooling of the roller-probe would, therefore, offer benefits in reducing the temperature within the probe to safe limits and enabling longer inspection duty cycles.

A bespoke active-cooling mechanism [196] was used to maintain the PAUT roller-probe's internal temperature below 50°C during an extended scan window. Figure 4.5 shows the schematic of the roller-probe active cooling system.

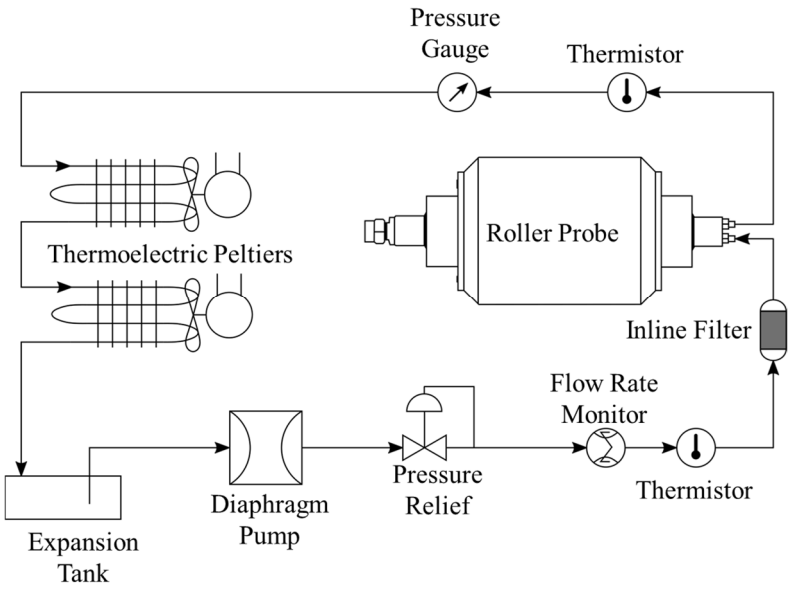

Figure 4.5. Block diagram of hydraulic active cooling system

To calculate the required mass-flow rate to maintain the roller-probe at a suitable operating temperature, a simplified system diagram was created to better understand the thermodynamics at play. The simplified control system and heat transfer diagrams are shown in Figure 4.6a and b respectively.

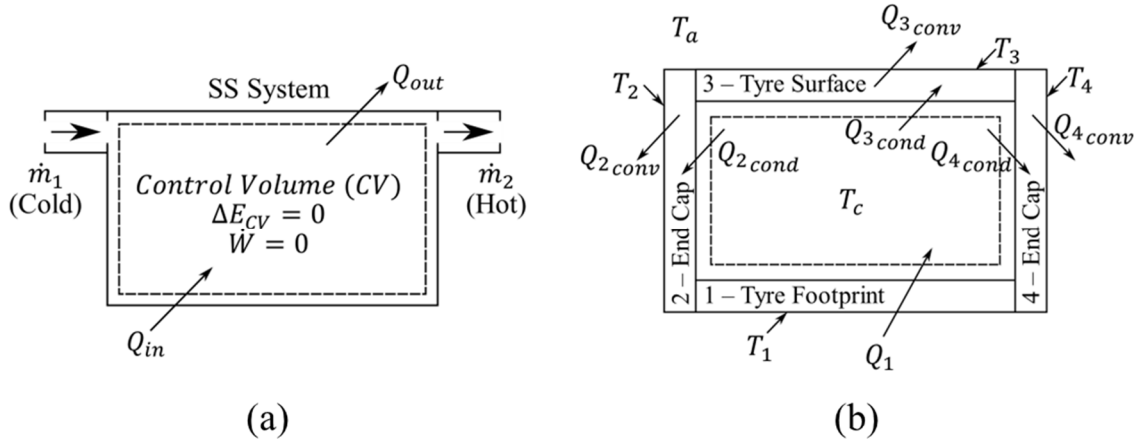

Figure 4.6. Simplified thermodynamic systems for PAUT roller-probe (a) control system and (b) heat transfer diagram

It was considered that the system is at a Steady-State (SS) and the mechanical work done at the control volume boundary is zero. The inlet flow temperature to the PAUT roller-probe is assumed to be fixed at a user-defined value. It was also assumed that the internal energy of the control volume is constant and $\sum \dot{m}_{in} = \sum \dot{m}_{out} = \dot{m}$. Additionally, it is assumed that the heat transfer in this system is dominated by conduction and convection, with the effects of radiation being considered negligible.

Based on Figure 4.6a, the energy-balance equation can be written as follows,

$$\dot{Q}_{in} - \dot{Q}_{out} = \dot{m}\left[(H_2 - H_1) + \left(\frac{{V_2}^2 - {V_1}^2}{2}\right) + g(Z_1 - Z_2)\right] \qquad (4.1)$$

Where subscripts 1 and 2 denote the inlet and outlet respectively, $\dot{Q}$ is the heat transfer rate, $\dot{m}$ is the mass flow rate, H is the enthalpy of the coolant fluid, V is the velocity of the coolant fluid, g is the gravitational constant and Z is the inlet/outlet height.

Assuming there is no significant change in inlet and outlet water density there will be no change in inlet and outlet velocity. Therefore, $A_1 = A_2 \rightarrow V_2 - V_1 = 0$, where A_1 is the cross-sectional area of the inlet, A_2 is the cross-sectional area of the outlet, V_1 is the inlet flow velocity and V_2 is the outlet flow velocity. Additionally, since there is no height difference between the inlet and outlet in the mechanical design, $Z_1 - Z_2 = 0$. Therefore:

$$\dot{Q}_{in} - \dot{Q}_{out} = \dot{m}(H_2 - H_1) \tag{4.2}$$

$$\dot{m} = \frac{\dot{Q}_{in} - \dot{Q}_{out}}{H_2 - H_1} \tag{4.3}$$

Considering the heat and flow boundaries shown in Figure 4.6b, expressions for the total heat transfer across each of the four boundaries can be found. It is assumed that $\dot{Q}_{in}$ is the total heat input to the roller-probe, $\dot{Q}_{out}$ is the total heat dissipated from the roller-probe, Q_1 is the heat input from component surface due to conduction, Q_2, Q_3 and Q_4 are the heat dissipated to the surroundings from the roller-probe due to the metal end-caps and rubber tyre through conduction and convection. For i = 1 to 4, T_i = outer surface temperature of face i, d_i = thickness of surface i and k_i is the coefficient of thermal conductivity of face i. Additionally, T_c is the coolant temperature, T_a is the surrounding atmospheric temperature and h is the co-efficient of convection of air.

$$Q_{in} = Q_1 = \frac{k_1 A_1 (T_1 - T_C)}{d_1} \tag{4.4}$$

$$Q_{out} = Q_2 + Q_3 + Q_4 \tag{4.5}$$

$$Q_2 = \frac{h A_2 k_2 (T_c - T_a)}{k_2 + d_2 h} \tag{4.6}$$

$$Q_3 = \frac{hA_3k_3(T_c - T_a)}{k_3 + d_3h} \tag{4.7}$$

$$Q_4 = \frac{hA_4k_4(T_c - T_a)}{k_4 + d_4h} \tag{4.8}$$

From equations (4.3), (4.4) and (4.5), we can derive final expressions for the mass flow rate and volume flow rate as follows:

$$\dot{m} = \frac{\dot{Q}_1 - (\dot{Q}_2 + \dot{Q}_3 + \dot{Q}_4)}{H_2 - H_1} \tag{4.9}$$

$$\dot{R} = \frac{1}{\rho} \times \frac{\dot{Q}_1 - (\dot{Q}_2 + \dot{Q}_3 + \dot{Q}_4)}{H_2 - H_1} \tag{4.10}$$

Where ρ is the coolant fluid density.

It was determined that to ensure a steady state internal temperature of 25°C, the volume flow rate of coolant should be $\dot{R}$ = 2.13 litres-per-minute by substituting in the known values.

Figure 4.7 shows the roller-probe with active cooling performing the same experiment as described in Section 4.2.1.

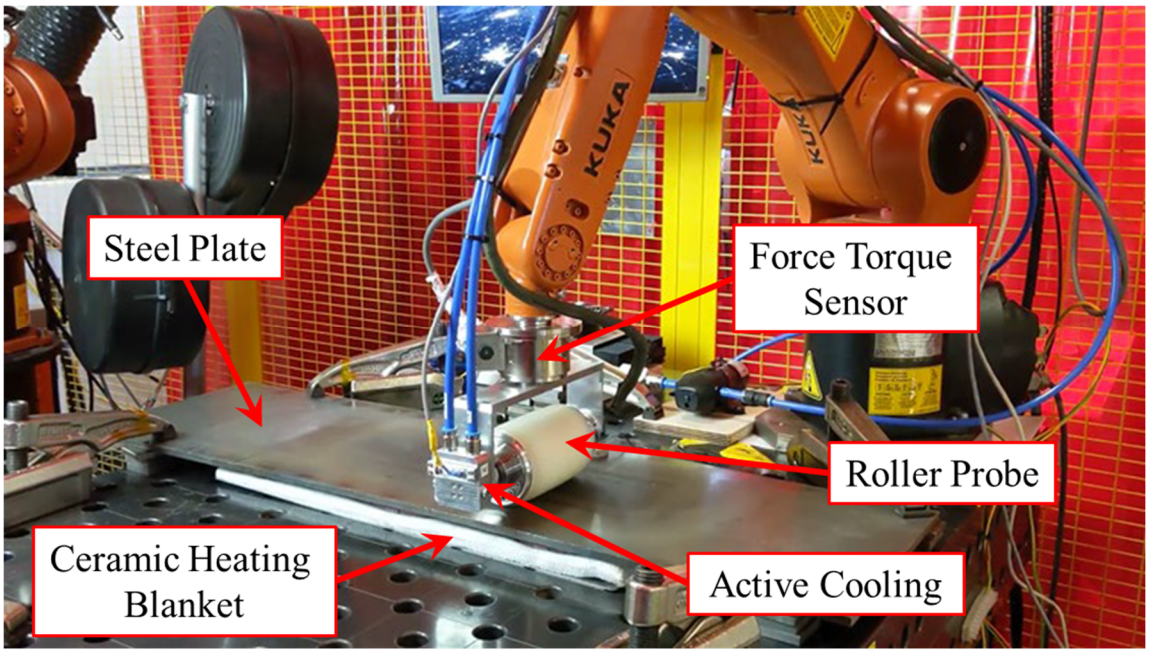

Figure 4.7. Active cooling temperature benchmarking experimental setup

Figure 4.8 shows the internal temperature of the roller-probe, with active cooling, where the base plate temperature was set to 350°C. With the addition of the active cooling system, the internal temperature of the roller-probe did not exceed 30°C and approached a steady state temperature within 90 minutes of the continuous test cycle. The additional noise present in the data when compared to passive operation is due to the additional components in the active cooling system, i.e. the pump and Peltiers.

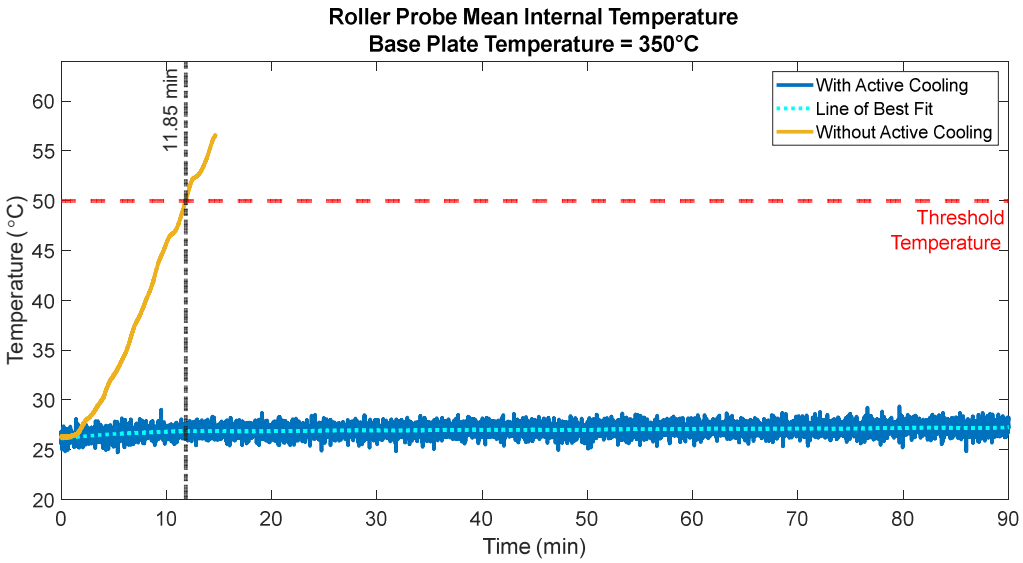

Figure 4.8. Mean internal roller-probe temperature before and after active cooling

4.2.3. Sensor Deployment Strategy

When developing the deployment strategy for the PAUT roller-probe, there were three main considerations:

I) Accurate and repeatable motion and positioning during inspection.

II) Compensation for the effects of industrially applicable non-machined surfaces.

III) Achieving consistent coupling during inspection.

To provide solutions to the above challenges, a bespoke robotic control system was used. Accurate and repeatable motion was achieved through a 6 Degree of Freedom (DOF) robotic manipulator, where its end-effector is the PAUT roller-probe sensor. Dry-coupling of the PAUT roller-probe sensor requires the application of sufficient force to ensure adequate transmission of the ultrasound into the component. The application of this force must be consistent throughout the inspection, adapting to any variability in the

component surface. This was achieved by integrating a 6 DOF Force-Torque (FT) sensor between the robot flange and end-effector, which allowed continuous monitoring of forces and torques around all axes. Furthermore, appropriate safety limits were set based on the maximum force and torque limits that the UT roller-probe sensor could sustain during inspection. The real-time, deterministic control of the above elements was performed through a central programming environment in LabVIEW®. The feedback of the FT sensor was linked to the robotic manipulator motion, with real-time corrections in the desired direction of inspection being made to maintain the setpoints and ensure consistent coupling throughout the inspection. Figure 4.9 shows the PAUT roller-probe mounted to a KUKA KR10 R1100 robotic manipulator through the FT sensor.

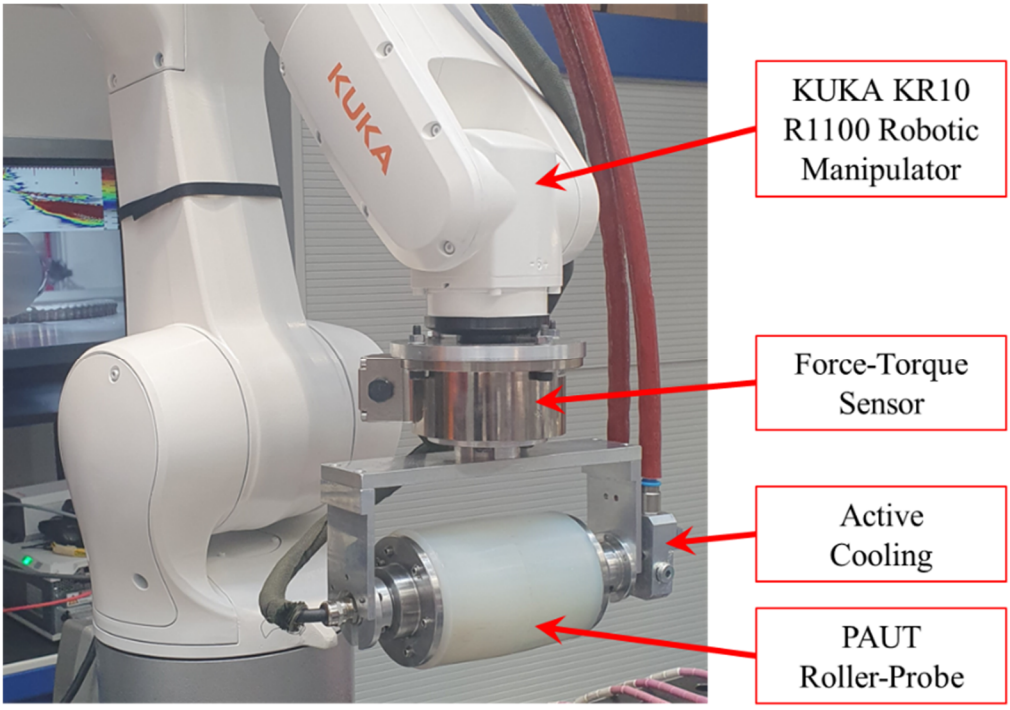

Figure 4.9. PAUT roller-probe with force-torque sensor and robotic manipulator

4.3. In-Process Ultrasonic Weld Inspection Imaging

4.3.1. Thermal Gradient Compensation

As previously discussed in Section 3.2, the presence of bulk thermal gradients, as expected with a localised heat source as used during welding, results in complex acoustic refraction where the ultrasonic beam will bend towards higher temperature regions within the material. If the temperature distribution within the component is known, then the beam bending effects experienced by the acoustic wave can be predicted and an appropriate correction made.

Although it is possible to perform calibration for an inspection carried out at a uniform elevated temperature by heating the calibration block to the same temperature, the same is not easily feasible for thermal gradients. The aim of in-process inspection, at this stage, is not to provide a fully-calibrated, code-compliant inspection but rather to introduce a greater certainty of a defect-free component entering the final inspection stage. There are still sufficient financial and scheduling benefits to be realised through this process to provide significant commercial advantages.

The array is able to steer and focus by applying time delays, known as focal laws, to the transmit and receive signals for each element, to compensate for the difference in transit time between the element and the focal point. This process, known as beamforming, requires the path and transit time to be calculated for every element in the array and every focal point. Since the speed of sound varies with temperature, reducing as the temperature increases, the thermal gradients present during welding produce distortion of the focus

and sound path, bending it towards the higher temperature region. Various techniques from FE Modelling [197] to ray-tracing [198] have been used to model the path and to derive the transit time through interfaces. Ray-tracing, treating closely spaced thermal contours as the interface between different materials (i.e. different velocity regions), was adopted due to faster computational speed [199]. This ray-tracing approach generates focal laws that ensure that the correct focus is achieved at the desired locations for the specified thermal map. However, the rest of the image will be distorted unless the bent beams are placed in the correct location in the image. A thermal compensation method was used to counteract the effects of beam bending and ensure that during the scan-conversion process, the bent beams are adjusted accordingly to correct for misalignments and produce a correct geometry throughout the whole image [200].

This thermal gradient compensation method was validated in the following experiment. A 15.8 mm thick flat carbon steel plate (S275) was machined with two 2.0 mm diameter SDHs at 5.0 mm and 10.0 mm depths to act as acoustic reflectors aligned along a 45° angle to mimic Lack of Fusion (LOF) along a 90° V-groove weld prep, as shown in Figure 4.10. A realistic thermal gradient was induced by performing an autogenous weld on the plate surface. Eight thermocouples, bonded to the top surface of the plate, were used to monitor the temperature distribution until it matched with the predictive model derived from COMSOL as described in Chapter 3, Section 3.2.1. The area covered by the thermocouples was equivalent to the footprint of the roller-probe.

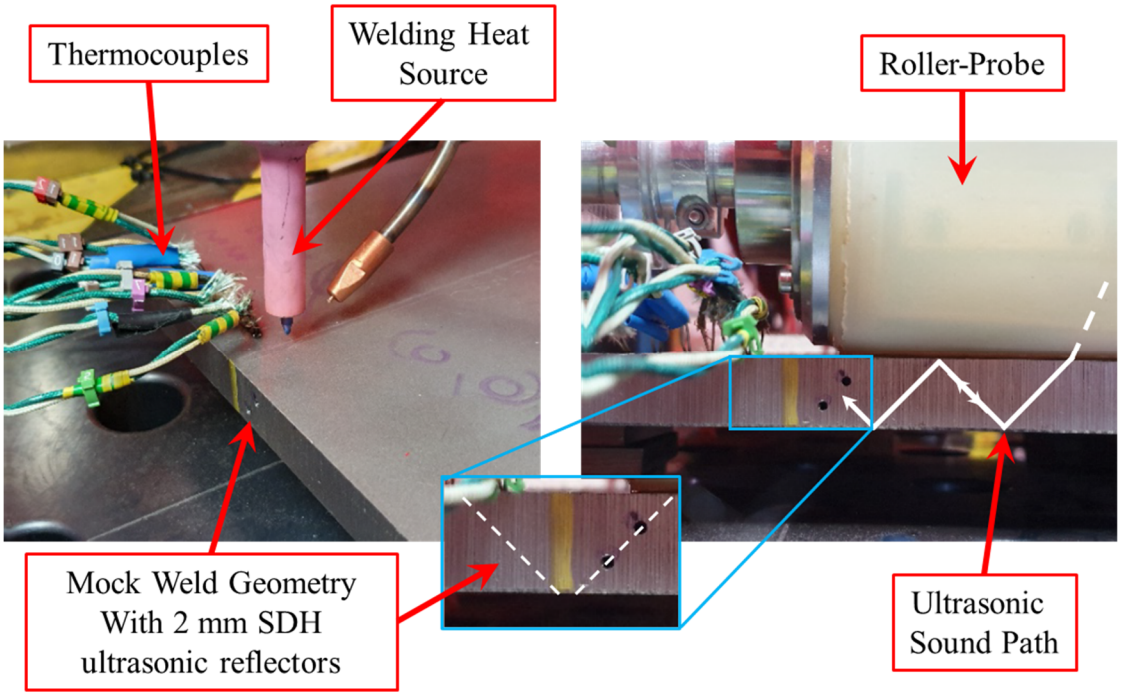

Figure 4.10. Experimental setup for validation of thermal compensation strategy showing the roller-probe position, calibration side-drilled holes and thermocouple placement

Three ultrasonic B-scan images were collected as shown in Figure 4.11: (a) At room temperature which acts as a reference image, (b) after welding, with thermal gradients affecting the ultrasonic transmission and no thermal gradient compensation and (c) after welding with real-time thermal gradient compensation applied. These B-scan images are shown in Figure 4.11. As expected, the thermal gradient results in a spatial shift of the indications within the B-scan, which can be seen clearly when tracking the red beam marker as highlighted. The echo tracked by this beam marker has the apparent range increased by 4.6 mm and the angle reduced by 1.2°. Figure 4.11c shows the positive effects of applying the compensation strategy, with the location of the reflector indications corrected and the range and beam angles matching well with the reference room-temperature image.

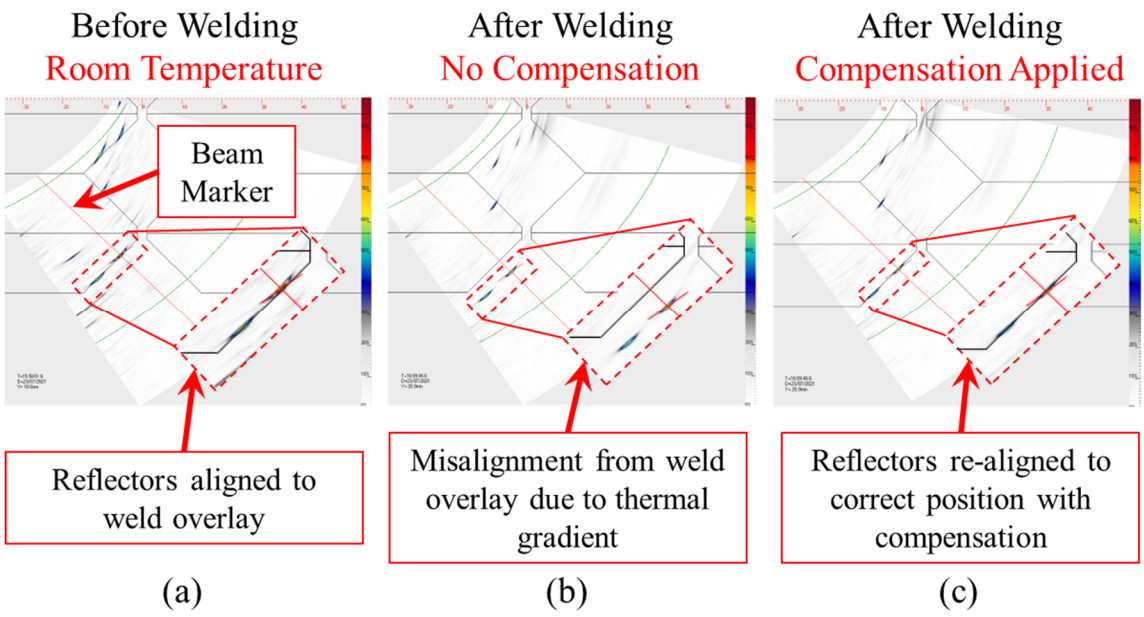

Figure 4.11. B-scan images taken (a) at room temperature, (b) after welding without thermal compensation applied and (c) after welding with thermal gradient compensation applied

4.3.2. Partially Filled Grooves

Ultrasonic inspection of partially-completed welds results in considerable reflections from the un-welded sidewall of the weld preparation creating false positive echoes and masking potential defects. It is necessary to mask out the effects of these strong reflections. This is achieved by implementing a Region of Interest (ROI) within the imaging area which is linked to the pass structure of the weld and therefore adaptive to the fill level at the point of inspection. An alarm system can then be set to be triggered by indications reaching pre-set amplitude thresholds and linked to this ROI. Therefore, the system will only flag a positive when there is an indication above the set threshold within the ROI and will not be triggered spuriously by the bevel reflection. Figure 4.12 shows the strong indication from the unfilled bevel present within the B-scan image. In Figure

4.12a there is no ROI set within the imaging area and therefore the alarm is being triggered even though there are no true defect indications present. In Figure 4.12b an ROI is set to include only the weld volume present within the joint and, since there are no defects present, the alarm is no longer being triggered as the unfilled bevel is masked out.

4.3.3. Interference Suppression

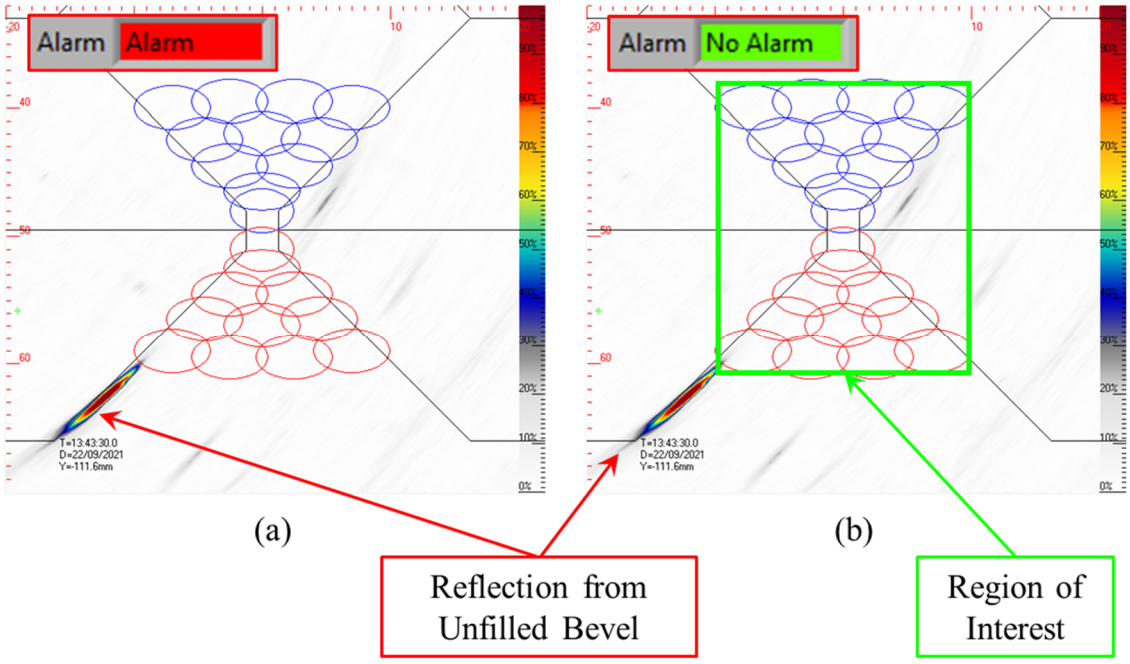

Figure 4.12. B-scan images of inspection of a partially filled weld joint showing the strong reflection present from the bevel where (a) there is no ROI implemented and (b) the ROI is restricted to the weld volume present at the point of inspection

The electromagnetic interference experienced during in-process weld inspection comes from a variety of sources. Most notably from the motor drives of the robotic manipulators used for deployment of both the sensor and welding process. These produce bursts of interference whose frequency is within the bandwidth of the transducer so cannot be rejected by traditional electrical filtering. Figure 4.13 shows three consecutive frames of ultrasonic data collected during an in-process weld inspection. The interference bursts

appear at different positions across the three frames producing moving patterns on the image (B-scan) and A-scan displays, while the ultrasonic reflector remains constant. Suppression of this interference is vital as the bursts generally have an amplitude exceeding the alarm threshold, resulting in unwanted, false-positives within the inspection.

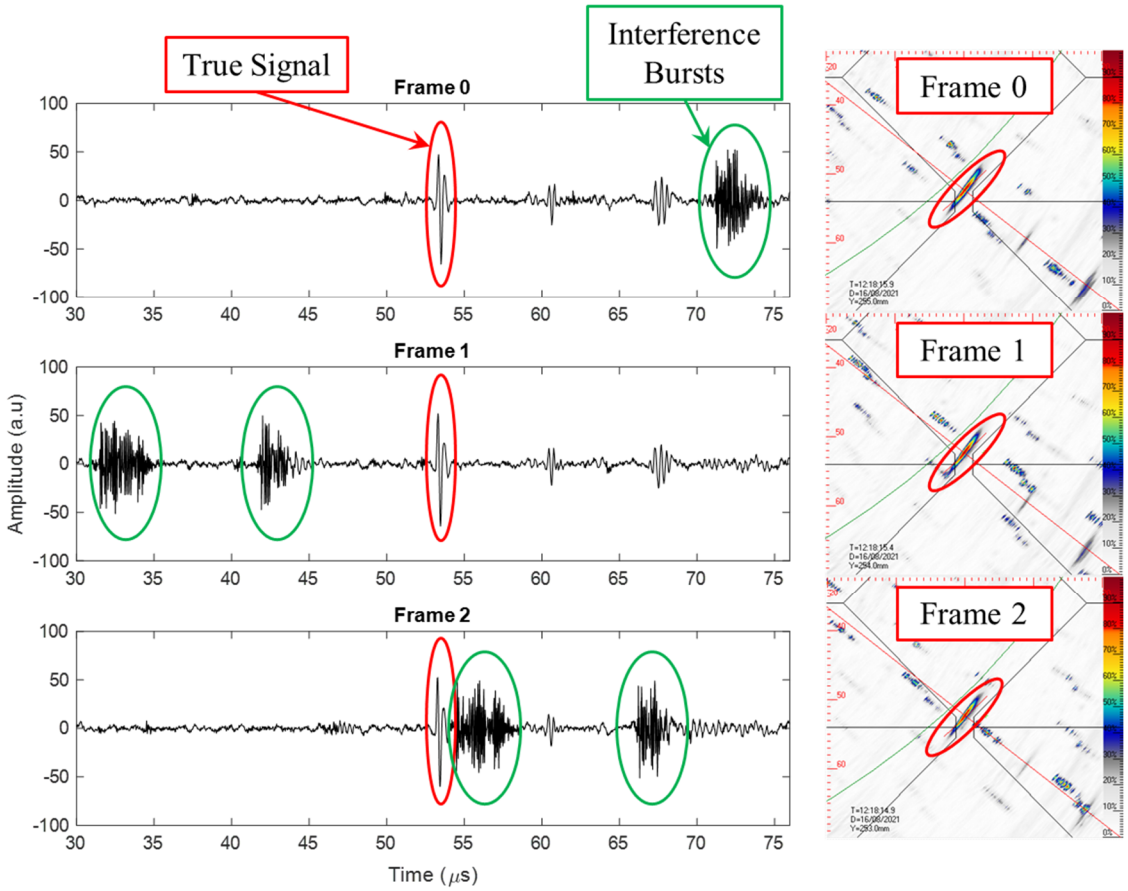

Figure 4.13. Three consecutively acquired frames showing raw A-scan signals (left) and B-scans (right). Highlighted are the true ultrasonic reflection echo and interference bursts which can be seen to occur at different times on each frame

To counteract this, an interference suppression algorithm was used, which uses a modified acquisition sequence followed by matched signal processing to completely remove the interference bursts without degrading the true ultrasonic signals [200]. Figure 4.14 shows a comparison between the un-processed B-scan image where the interference

bursts are easily identifiable and the resultant B-scan image after noise suppression has been applied.

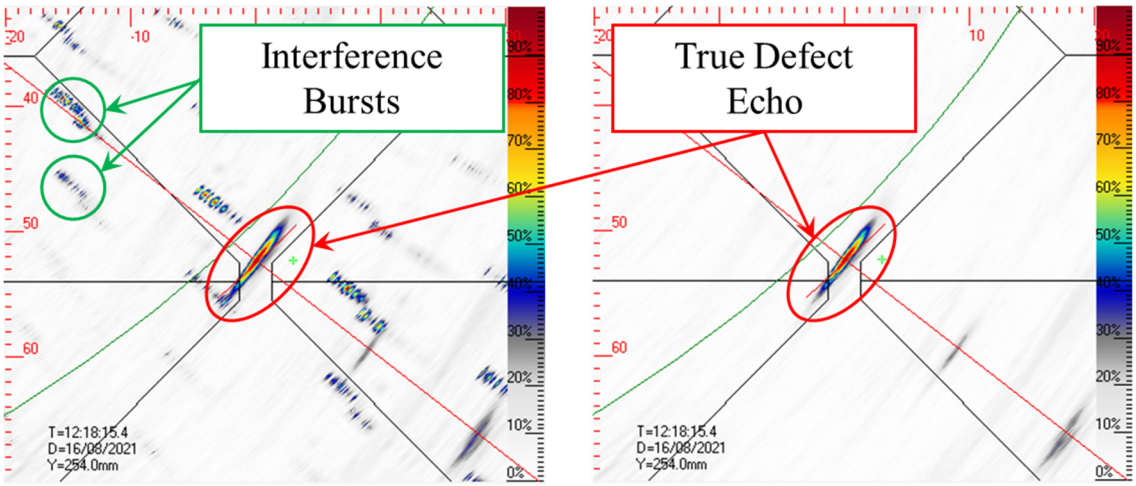

(a) (b)

Figure 4.14. B-scan images (a) before and (b) after application of the interference suppression algorithm

Improvements are conventionally quantified by a change to the SNR, however, this is not appropriate here, where the amplitude of the interference can easily be greater than that of the true signal, resulting in a negative value of SNR. As long as the cluster of interference samples are correctly identified by the algorithm, they are completely removed. For the samples where there is no interference across any of the streams, the SNR is improved by the same as conventional signal averaging.

4.3.4. Component Thickness Mapping

The thickness of hot-rolled steel plates is subject to tolerances of ±0.8 mm for thicknesses between 15.0 and 25.0 mm [201]. Similarly, un-machined seamless pipes are subject to wall thickness tolerances of ±12.5% [202]. That means that for a pipe with a

"nominal" thickness of 16 mm, the thickness is likely to vary approximately ±2.0 mm around the circumference of the pipe. A well-defined understanding of the thickness of a weld is vital when inspecting to ensure the correct placement of any defects which are discovered. Variation in thickness results in the incorrect vertical positioning of defects which is further magnified where multiple skips off the back and front walls are necessary. The positioning of the roller-probe for inspection of material with a thickness of 16 mm is such that imaging occurs at 3.5 half-skips (See Figure 4.10 for ultrasonic inspection path), this results in a total vertical positional error of ±6 mm in the worst case scenario of a ±12.5% thickness. It also results in similar horizontal positioning inaccuracy. Therefore, it is critical to apply corrections for the thickness variation to dynamically change the weld overlays and alarm ROI to maintain correct positioning of both defect indications and reflections from the unfilled bevel. To achieve this, each inspected component is first scanned ultrasonically to map the thickness variation around the circumference. This can be achieved by performing a sectorial scan of ±10° using longitudinal waves, with angles measured with respect to the surface normal [200]. Using a sector scan rather than a single transmission angle at 0° allows for any misalignment to be accounted for by searching for the beam angle which provides the maximum response. This data is then analysed to generate a thickness profile of the pipe circumference which can be applied during inspection for dynamic adjustment of the weld overlays and ROI position in the imaging display. Figure 4.15 shows the collected thickness data for two different components. One is an unmachined seamless hot rolled pipe (S355J2H) with an Outer Diameter (OD) of 323 mm and nominal thickness of 16 mm and the second is a machined seamless hot rolled pipe (S355J2H) with an OD of 400 mm and a nominal

thickness of 18 mm. As can be seen, the unmachined sample has significantly higher variability in the thickness, with a maximum variation of +1.1 mm, which is to be expected. The machined sample shows a more controlled thickness tolerance, with a maximum variation of +0.1 mm. Evidently, prior knowledge of the thickness variation is vital to ensure positional accuracy of any defects found.

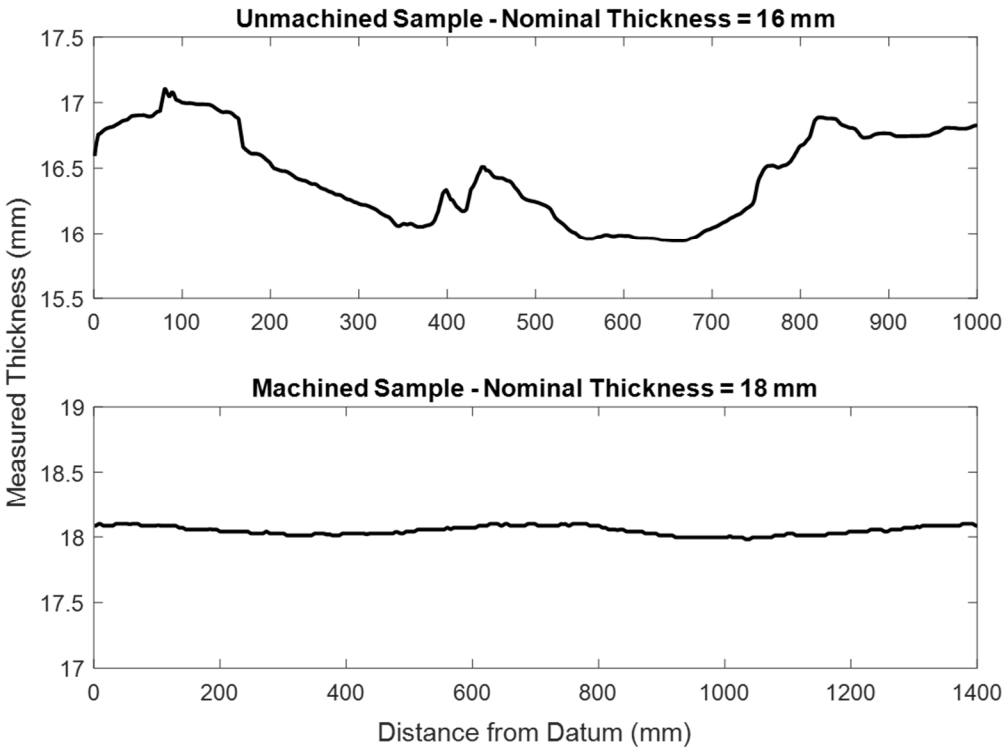

Figure 4.15. Ultrasonic thickness mapping of unmachined and machined components

4.4. Experimental Trials

4.4.1. Experimental Set-Up

An updated welding and inspection cell was developed and builds upon the cell architecture discussed in Chapter 3 Section 3.2.2 with the addition of a KUKA rotary head stock to facilitate welding and inspection of pipes. Figure 4.16 shows the cell layout.

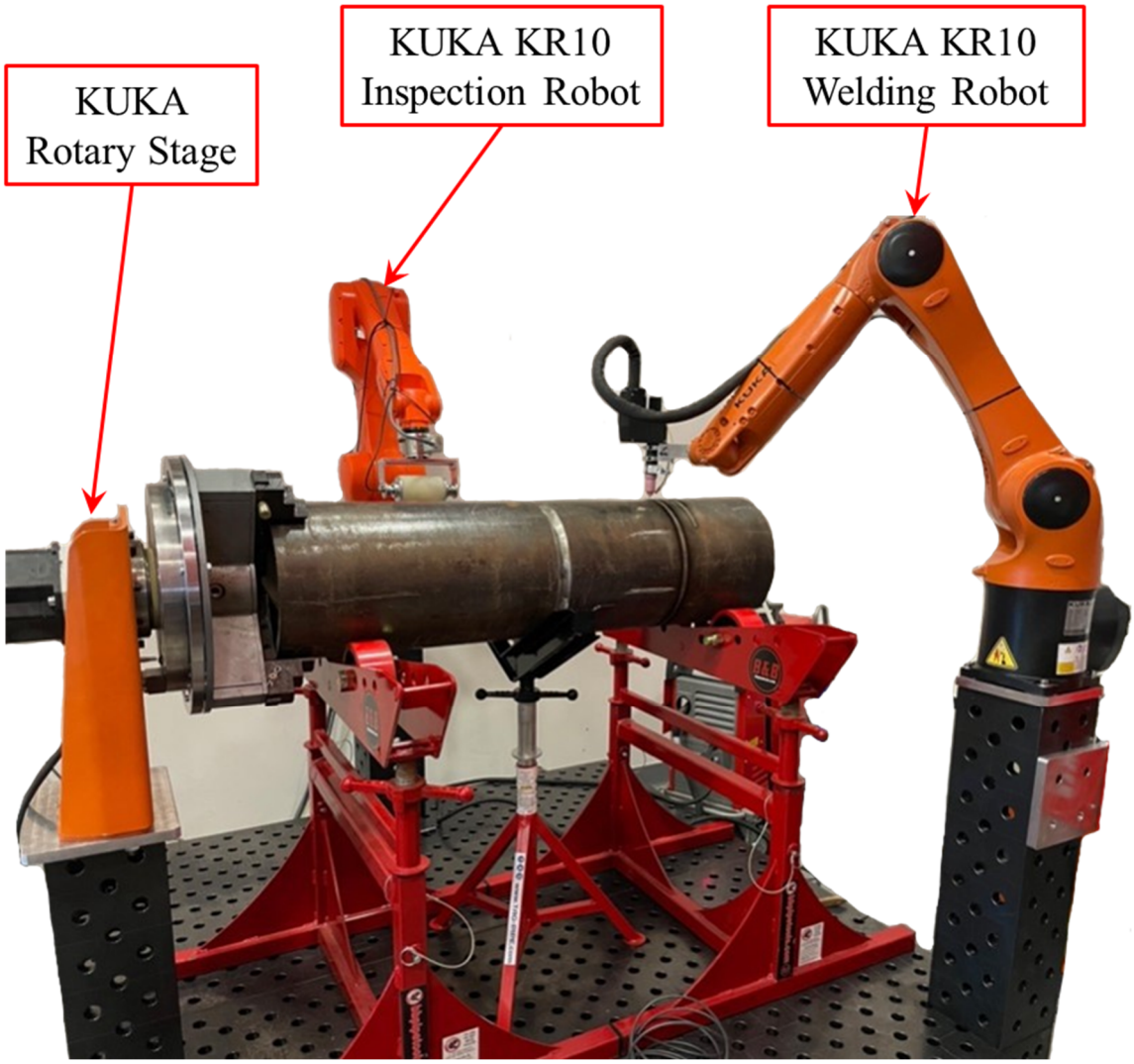

Figure 4.16. Welding and inspection cell hardware layout

Four seamless hot-rolled pipe test pieces made of S355J2H were used to optimise, validate and demonstrate the in-process inspection system developed. Two of the pipes had an OD of 323 mm and two had an OD of 406 mm. For all four test pieces, the nominal thickness was 16 mm and a 90° included V-groove geometry was used. The test pieces were mounted to the rotary stage to enable circumferential welding in a 1G position.

All welding trials were performed using a GTAW process, deployed via a KUKA KR10 R1100 robotic manipulator. To monitor the welding process, a XIRIS XVC-1000 HDR camera was used. The PAUT roller-probe was deployed via a KUKA KR10 R1100 robotic manipulator as described in Section 4.2.3. Control of the ultrasonic parameters was achieved through a custom PEAK NDT LTPA phased array controller. A 140 mm circumferential offset of the PAUT roller-probe to the welding position was found to be appropriate due to physical space constraints. The thermal modelling discussed in Chapter 3, was used to validate the safety of this operating position in terms of part surface temperature. Figure 4.17 shows a more detailed view of the hardware integration highlighting the relevant components and the inspection position relative to the weld torch.

Each test piece was scanned initially to generate a thickness profile which was then loaded into the acquisition software to provide the adaptive weld overlays and ROI. Each test piece was then inspected during each weld pass to validate the ability of the system to accurately detect defects. Ultrasonic data acquisition was performed at 5 Hz, i.e.

5 frames of data per second, which is equivalent to a cross-sectional image per millimetre of weld.

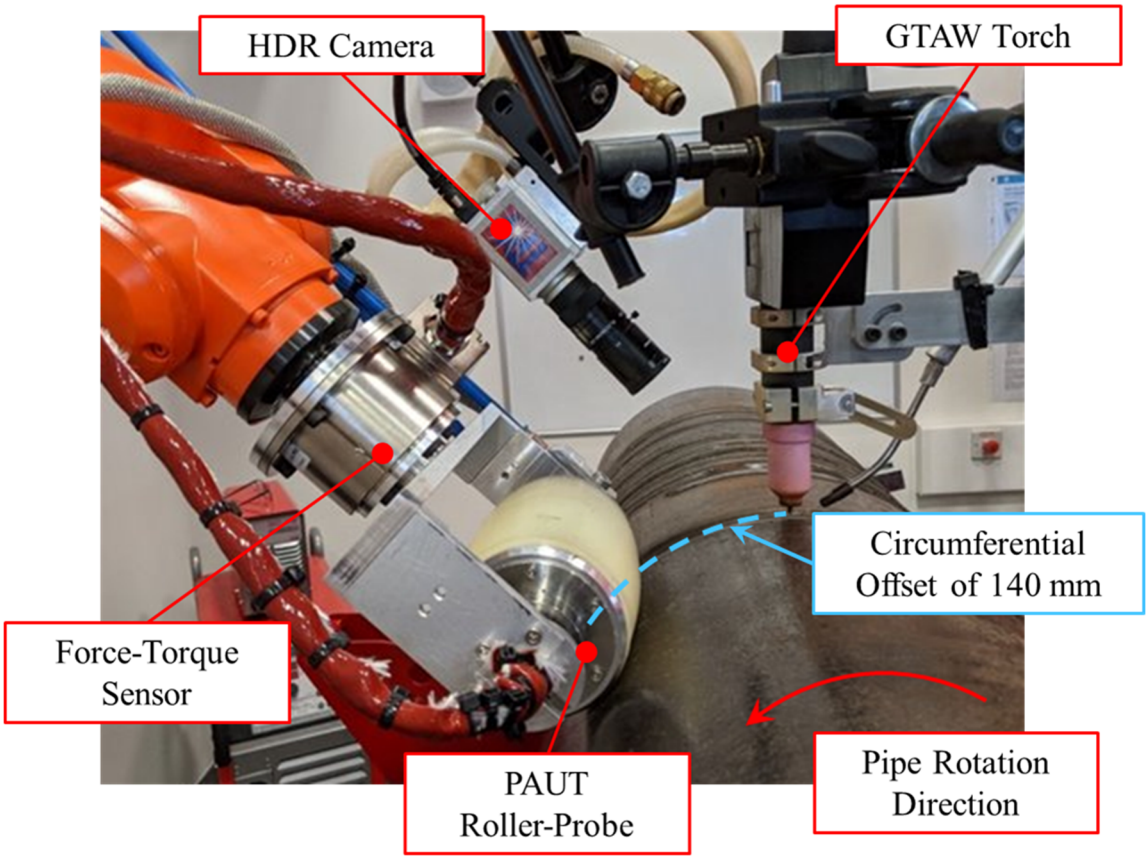

Figure 4.17. Experimental hardware setup

4.4.2. Artificial Defect Embedding Strategy

To enable in-process imaging, sizing and verification of the overall inspection accuracy, several intentional defects were embedded in each of the test pieces. The process for embedding artificial defects within welded components was discussed in Chapter 3, Section 3.3.2. Tungsten tubes with an OD of 2.9 mm, Internal Diameter (ID) of 1.0 mm and length of 30 mm provide a controlled size and position reference indicator for verification purposes. The tubes were embedded by first machining a slot within the weld

volume before manually tacking the tubes in place to prevent movement as the component pipe rotates during welding. Iron powder was also added into the slot, to reduce the volume of unfilled air after welding. Figure 4.18a shows a tungsten tube embedded in a machined slot after pass 7 and subsequently covered by weld passes as shown in Figure 4.18b. Figure 4.18c shows the location of the defect within an approximated pass structure. Tungsten tubes were placed in the centre of the weld volume to represent inclusions and close to the sidewall to replicate LOSWF.

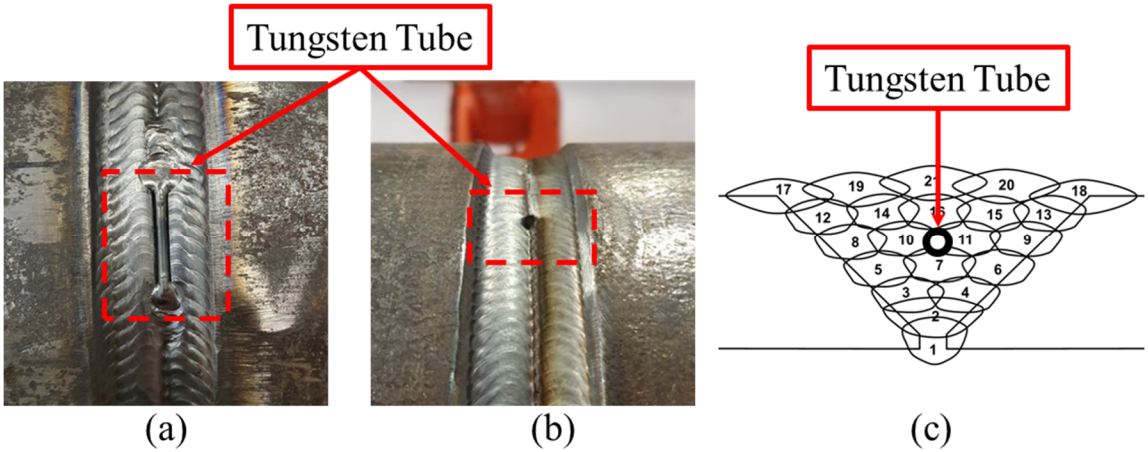

Figure 4.18. Images showing (a) embedding of a tungsten pipe within machined groove and tack welded in place, (b) an embedded tungsten pipe covered by subsequent weld passes and (c) the relative position of tungsten defect within the completed pass structure

4.5. Results & Discussion

Shown here are the results from the final test piece, where the welding parameters and defect insertion strategies had been improved throughout the previous trials. Figure 4.19 shows the detection of a tungsten defect intentionally embedded in layer 5. This tungsten defect was placed close to the weld bevel to replicate a LOSWF type defect. There is also a signal from the root, this is a normal geometrical reflection rather than an indication of a root defect.

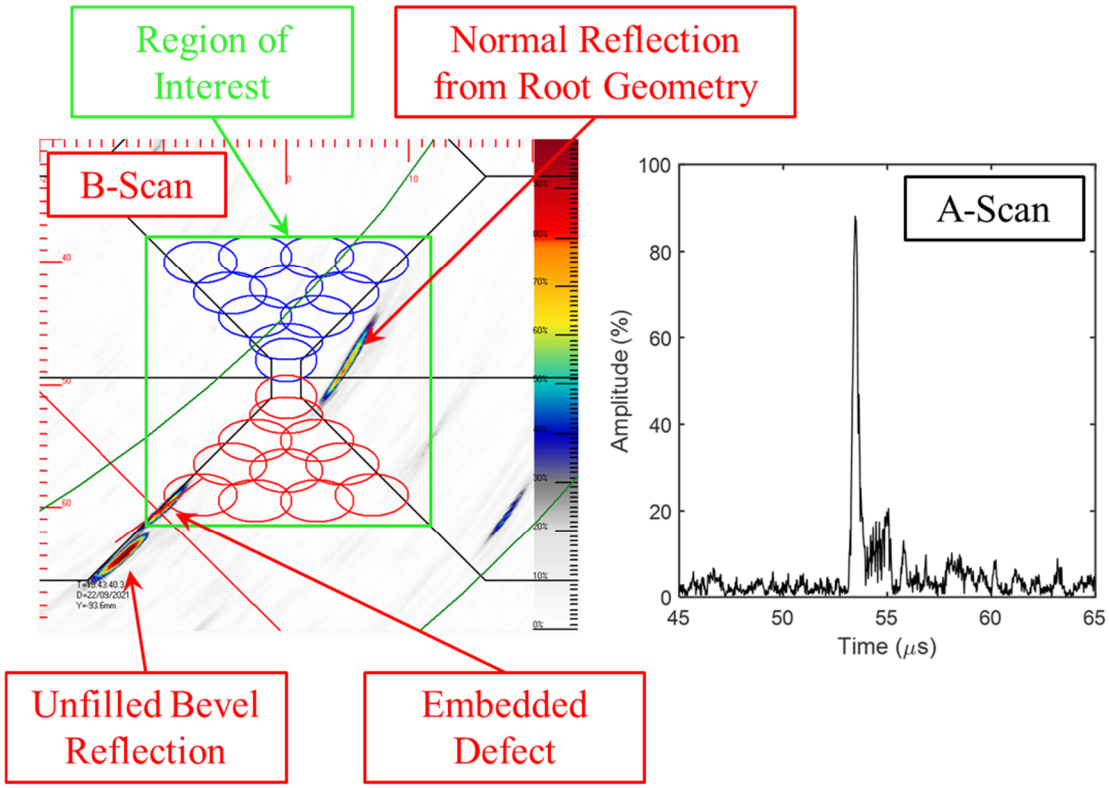

Figure 4.19. In-process UT inspection of a partially filled multi-pass weld showing correct detection of an intentionally embedded tungsten defect inserted in layer 5 (Defect 1) and a normal reflection from the root geometry

Figure 4.20 shows the detection of a tungsten defect intentionally embedded in layer 3. This tungsten defect was included centrally within the weld volume to replicate an inclusion type defect. Air pockets left around the tungsten tube during insertion have resulted in some reflectors which show in the B-scan as a cluster of signal points.

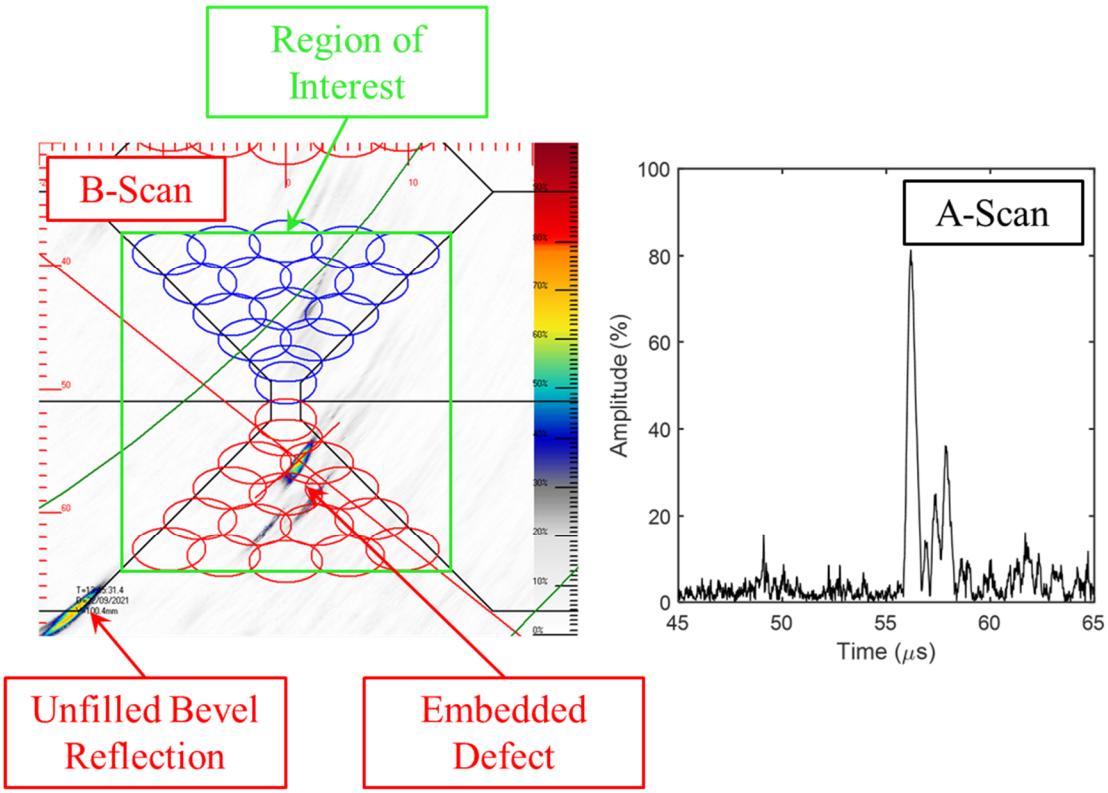

Figure 4.20. In-process UT inspection of a partially filled multi-pass weld showing correct detection of an intentionally embedded tungsten defect inserted in layer 3 (Defect 2)

Figure 4.21 shows the detection of a tungsten defect intentionally embedded in layer 6 of the weld. This tungsten defect was also placed centrally within the weld volume to replicate an inclusion type defect. Again, there is an indication visible in the root of the weld which is just a geometrical reflection.

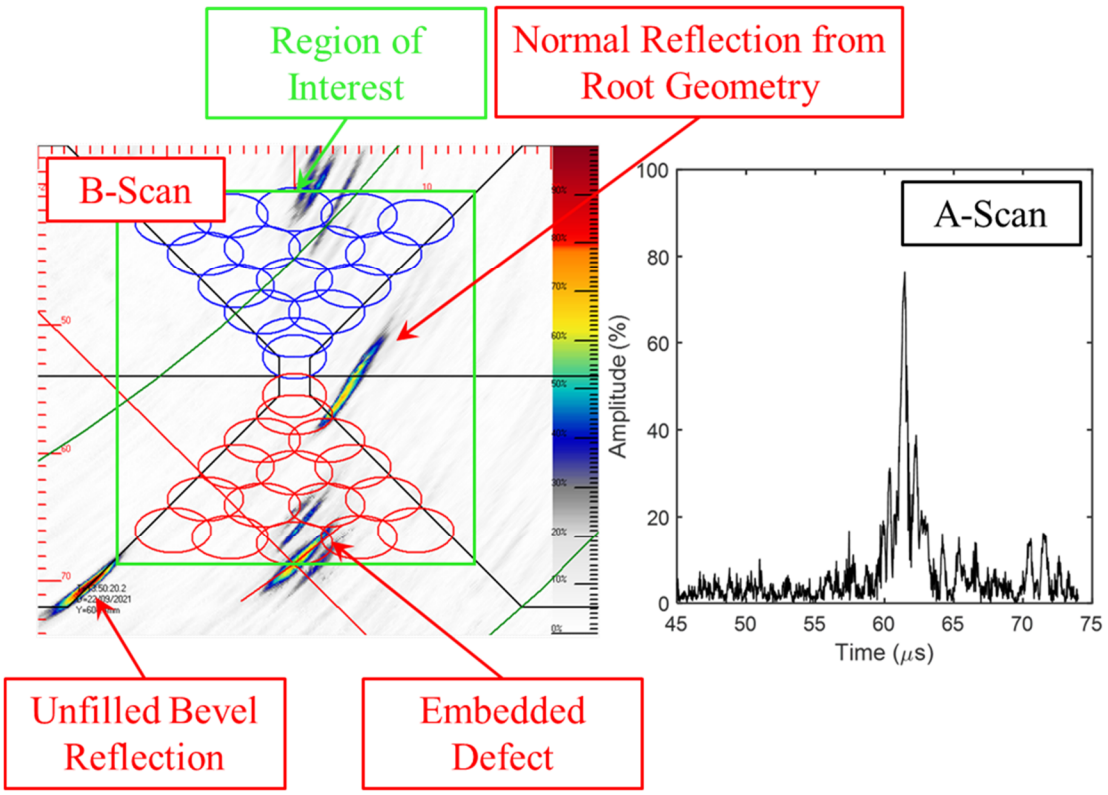

Figure 4.21. In-process UT inspection of a partially filled multi-pass weld showing correct detection of an intentionally embedded tungsten defect inserted in layer 6 (Defect 3) and a normal reflection from the root geometry

The results can also be displayed in a C-scan display, where the maximum amplitude for each beam within the ROI is plotted for each frame of data. This is effectively showing the results as an "un-wrapped" view of the weld joint itself and can aid in defect identification and sizing. Figure 4.22 shows a C-scan display of the in-process inspection of another test-piece. Here, the strong bevel reflection is seen clearly for the first 140 mm of the scan, after this point the weld pass being performed has fully filled the sidewall and this echo disappears. Also highlighted are indications of successfully detected porosity and inclusions within the weld volume. Defect characterisation is best performed through a combination approach, using the A, B and C-scan data in combination.

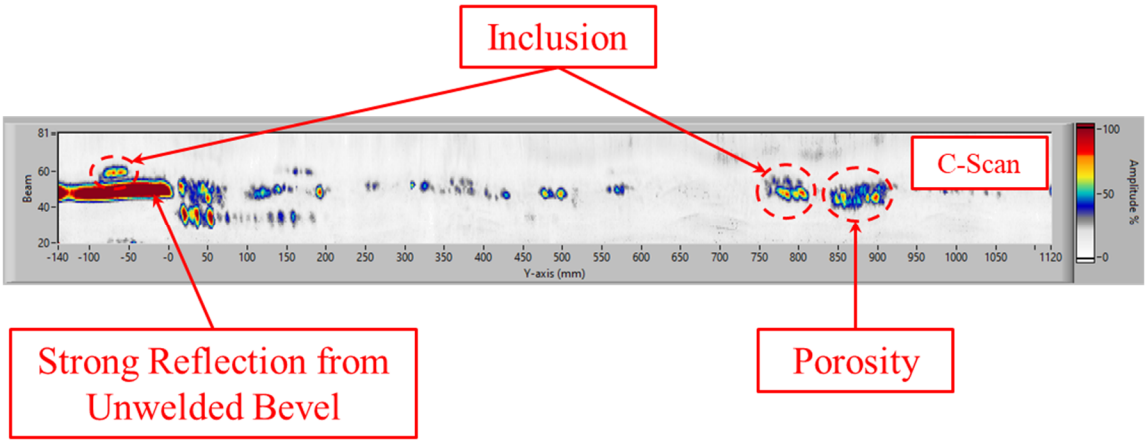

Figure 4.22. C-scan display

To quantify the efficacy of this in-process inspection system a final, traditional PAUT inspection of the test piece was carried out post-weld, at room temperature, as a point of comparison. The post-weld inspection was carried out with a standard 5 MHz, 64-element, linear ultrasonic array and PAUT weld inspection wedge of the same nominal refraction angle as the roller-probe. This inspection was carried out with the aid of liquid coupling on the surface of the test-piece, as is standard in a traditional PAUT inspection. SNR values for each of the intentional defects shown here were calculated for both the in-process inspection and final, cold inspection. SNR was calculated in decibels using Equation (4.11).

$$SNR = \log_{10}\left(\frac{peak\ defect\ amplitude}{mean\ noise\ amplitude}\right) \qquad (4.11)$$

In each case, the mean noise amplitude was taken from the period before the defect signal for a total of 1100 sample points. The SNR values are documented in Table 4.1.

Table 4.1. Signal-to-Noise Ratio (SNR) values for in-process inspection and traditional post-weld PAUT inspection

	SNR Values (dB)	
	Post Weld Inspection using Standard Array + Wedge	**In-Process Inspection using PAUT Roller-Probe**
Defect 1 (Figure 4.19)	35.49	32.65
Defect 2 (Figure 4.20)	38.34	31.56
Defect 3 (Figure 4.21)	30.77	29.42

The SNR values for the in-process inspection are lower, which is to be expected due to the dry-coupling of the roller-probe and significantly harsher environmental factors as discussed in detail. However, this comparison does show that the drop in SNR is marginal, with a maximum difference in SNR of 6.78 dB shown for defect 2 (Figure 4.20).

4.6. Chapter Summary

This chapter has presented a new approach to volumetric inspection of fusion welds which offers tangible commercial and economic benefits to a number of industries such as Nuclear, Defence and Energy. A high-temperature compliant PAUT roller-probe NDE sensor enabling continuous in-process weld inspection at temperatures compatible with most high-integrity fabrication pre- and post-weld heat treatments was introduced and deployed. The dry-coupled inspection approach removes the potential for weld contamination from traditional liquid acoustic coupling media. Additionally, multiple imaging strategies were introduced and quantified to compensate for:

I) Geometrical distortion and beam defocusing due to the elevated temperatures and thermal gradients present during welding

II) False-positives arising from the unfilled bevel edge via adaptive masking of the weld volume throughout the welding schedule, allowing accurate identification of defective areas.

III) Spurious artefacts present within the inspection due to EMI and robot motor drives via an interference suppression algorithm.

The results of this work are presented on carbon steel pipe demonstrators with both intentionally embedded and unintentional defects. The SNR of the imaging and inspection system is measured, evaluated and compared against traditional phased array ultrasonic testing techniques. The in-process inspection system developed here shows SNR values comparable with that of traditional post-weld ultrasonic testing techniques showing an average SNR value of 31.21 dB.

4.7. Author Statement

The author would like to acknowledge that this chapter was highly collaborative and could not have been possible without the time, knowledge and expertise offered by many academic and industrial collaborators. The work presented here was part of a much larger collaborative project, **A**dvanced **W**elding **E**quipment **S**ystem for **I**nspection and **M**onitoring (AWESIM) led by Cavendish Nuclear Ltd. The consortium included Doosan Babcock Ltd, the Advanced Nuclear Research Centre at University of Strathclyde, the Nuclear Advanced Manufacturing Research Centre at University of Sheffield, Peak NDT Ltd, Babcock International Group and Frazer Nash Ltd. The AWESIM project was funded by the BEIS Nuclear Innovation Programme under the Phase 2b call on Advanced Manufacturing and Materials.

The author's key personal roles within the project included:

I) Leading the team in NDT deployment, verification and quantification.

II) Development of thermal models to facilitate thermal compensation.

III) Robotic welding of test coupons including artificial defect embedding.

IV) Ultrasonic data capture and review – both in-process and post-weld for comparison and verification.

V) Quantification of imaging and compensation strategies, roller-probe performance and overall system performance.

The following author statement is given to recognise each individuals' effort in this work.

Nina E. Sweeney	Methodology, Investigation, Formal Analysis, Validation, Data Curation, Writing – Original Draft, Visualisation, Writing – Review & Editing
David Lines	Software development and deployment, Methodology, Investigation, Writing – Review & Editing
Charalampos Loukas	Software, Methodology, Investigation, Writing – Review & Editing
Randika W. Vithanage	Methodology, Investigation, Writing – Review & Editing
Momchil Vasilev	Software, Methodology, Investigation, Writing – Review & Editing
Charles N MacLeod	Conceptualisation, Methodology, Writing – Review & Editing, Supervision, Project Management
Ehsan Mohseni	Methodology, Investigation, Writing – Review & Editing

Chapter 5

In-Process Ultrasonic Phased Array Weld Pool Monitoring

5.1. Introduction

In-process monitoring of welding processes makes it possible to detect the formation of defects at the earliest possible point to enable quicker and more cost-effective repair while improving manufacturing schedule-certainty. Furthermore, the valuable data gathered through in-process monitoring of welding processes may be used to control and optimise the process in real time to reduce the overall rate of defect formation. As previously discussed in Chapter 2, Section 2.6, the two most important information sources which require monitoring to help ensure weld quality in-process are the weld seam and the weld pool [203]. While weld seam tracking has been successfully deployed using laser, active vision [204–206] and arc sensing technologies [206,207], developments in effective weld pool sensing have yet to be delivered.

Currently, the most widely adopted methods for monitoring the weld pool use passive vision through specialised HDR cameras [208–210]. Vision systems can be used

for the measurement of weld pool width, length and, in some cases, surface convexity which can be used to predict penetration depth [211]. IR cameras have been used to monitor the temperature of molten weld pools which can also be related to the penetration depth [212,213]. Visual methods only provide external surface measurements with no indication of the internal structure of the weld pool and predictions must be made to infer other important geometrical properties which cannot be measured directly i.e. penetration depth. Furthermore, the requirement for a direct line of sight to the weld pool makes them inappropriate for use in conjunction with many geometries and welding processes such as SAW.

The most common methods available which can provide volumetric and internal weld pool information are Radiographic Testing (RT), Eddy Current Testing (ECT) and Ultrasonic Testing (UT). RT has limitations in terms of applicability on thicker materials [214] and the need for radiation safety management [215]. The use of ECT for inspection is limited by the achievable penetration depth [216]. Ultrasonic sensing techniques in the field of weld pool monitoring have not been widely adopted, however, it has become a key area of research in recent years.

An in-line approach for real-time monitoring of the resistive spot welding process using ultrasonics has been successfully implemented within commercial spot welding equipment [217,218]. Here, pulse-echo ultrasonic inspection is used to monitor the growth and solidification of spot welds. Through characterisation of the resultant signal responses, an effective screening method for spot welds was developed which can identify spot welds

with insufficient penetration [219,220]. The application of linear and matrix arrays to provide additional information in this area has also been explored [221,222].

Air-coupled ultrasonic techniques have also been used successfully for in-process screening of thin section butt welds, through the use of guided Lamb waves [223]. While air-coupled ultrasonics has the advantage of being non-contact in a high-temperature environment, the SNR is generally low when compared with traditional contact alternatives [224]. LU, another non-contact approach, has also been used to monitor the joining of lapped steel plates using fusion GTA spot welding [225]. LU generation has also been used alongside EMATs for reception to estimate the penetration depth of a fusion butt weld in real-time [226]. LU systems come with stringent safety requirements for in-situ deployment and are currently far more expensive to implement than conventional UT systems [227].

Real-time ultrasonic thickness measurements have been used to provide a priori knowledge of material thickness in order to inform a feed-forward closed-loop control system capable of welding butt joints of varying thickness while maintaining consistent penetration [228]. This indirect sensing method does not provide information relating to the weld pool itself and instead relates the thickness measurement to appropriate welding parameters based on a pre-defined parametric function. Traditional single-element contact ultrasonic techniques have been used successfully to monitor in real-time the deposition of the root pass of a multi-pass gas tungsten arc weld [229]. The use of longitudinal ultrasonic waves in an angled beam pitch-catch setup was shown to be effective in monitoring and characterising the weld pool. Furthermore, this technique also showed

promise for the detection of defects as they are formed. However, significant limitations of this approach are anticipated when considering its use for monitoring higher passes within a multi-pass weld. Single-element transducers have fixed physical characteristics which constrain their operation, such as natural focus and beam spread [230]. Furthermore, angled inspections are limited to pre-defined individual angles through the use of wedges. Focusing of the ultrasonic energy at different angles and positions is a necessity for accurate isolation of the weld pool from the surrounding solidified material. PAUT has become increasingly popular in many NDE applications over recent years, due to the arrays' flexibility when compared with single-element transducers [231]. They offer the ability to implement a large number of inspection modalities with a single transducer from a single inspection point, increasing coverage and sensitivity [232] and making them a more appropriate choice.

In this chapter, phased array ultrasonic testing is used to interrogate the molten weld pool in real-time. Optimised ultrasonic longitudinal wave modes were used in a focused pitch-catch arrangement to monitor the deposition of both root and hot pass welds. The received ultrasonic signals are shown to contain information related to key physical transitions occurring within the welding process, namely the melting and solidification of the weldment. Furthermore, the technique used here is shown to be effective for determining weld quality in real-time with significant signal changes occurring when defects such as Lack of Root Penetration (LORP) are present. The accurate focusing and steering capabilities offered by phased arrays are used to successfully isolate the molten weld pool from the surrounding solidified weldment during deposition of multiple layers

of a multi-pass weld. It is also deemed that the information held within the ultrasonic signals is of sufficient quality to inform process control algorithms in the future.

5.2. Technical Considerations for Ultrasonic Monitoring of Fusion Weld Pools

5.2.1. Single-Element vs Phased Array Transducers

The inspection of individual weld passes within a multi-pass weld, as necessary for in-process monitoring of the weld pool, is effectively impossible using single-element transducers due to their aforementioned limitations. As the weld cross-section is filled, it becomes increasingly difficult to isolate the liquid weld pool from the already deposited and solidified weld material surrounding it. Due to the effects of beam spread, the acoustic energy propagates into the surrounding solid material, obscuring any signals from the molten weld pool due to acoustic velocity differences and attenuation. Phased arrays are therefore an attractive alternative in this scenario, allowing accurate beam steering and focusing to concentrate the ultrasonic energy on the intended molten weld pool. Furthermore, through the use of angular sweeps, additional data for optimisation purposes can be collected within a single acquisition.

Figure 5.1 [144] shows models produced using the NDT simulation software package CIVA [233] of a weld inspection using (a) an unfocused longitudinal transmission using a 6 mm diameter single-element probe with a 70° wedge and (b) a phased array 70° longitudinal transmission focused at the root. The approximate welding pass layout has been overlaid in each case. The focusing capabilities of phased array

inspection allows for more accurate isolation of individual passes. In the case of the single-element inspection, the natural focus of the probe means that the beam energy is concentrated not far below the surface of the specimen and the associated beam spread results in a large area of the weld being covered. While the beam spread and natural focus of a single-element probe can be altered by design, a bespoke set of probes and wedges would be needed for each weld pass which quickly becomes impractical when considering varying geometries and welding pass sequences. Through the correct provision of angle and focus point, the use of phased array can maximise the amount of energy transmitted through a single weld pass making them a more appropriate choice.

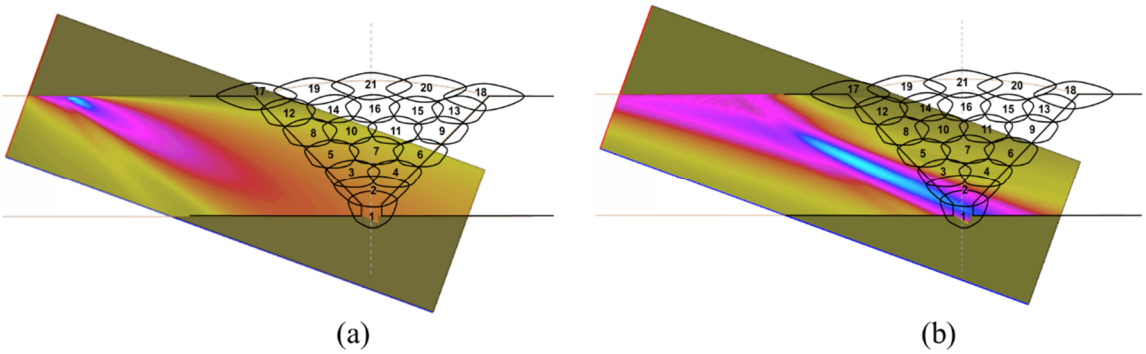

Figure 5.1. CIVA beam computation models of a 70° weld inspection using (a) an unfocused single-element probe and (b) a focused phased array probe with weld pass overlays [144]

5.2.2. Ultrasonic Wave Propagation Within the Molten Weld Pool

There are three common ultrasonic setups which may be leveraged to interrogate the weld pool in real-time: shear pulse-echo, longitudinal pulse-echo and longitudinal pitch-catch. A robust understanding of the expected ultrasonic wave propagation for each of these setups during various stages of the welding process is vital to identify their

effectiveness for weld pool monitoring. Figure 5.2 shows simplified 2D wave propagation diagrams for each of these ultrasonic setups, taking the simplest welding scenario of a root weld. Three stages of the welding process were analysed:

I) Before welding, where only the weld groove is present.

II) During welding, where a liquid weld pool is present at the root of the weld groove.

III) After welding, where the weld bead has fully solidified.

This analysis looked to better understand the interactions of the ultrasonic waves within the weld volume at these various stages to identify the benefits and drawbacks of each ultrasonic setup.

The main characteristic of interest with shear waves is their inability to exist within liquids. The reflection coefficient from the surface of the weld pool will be unity and all energy will return to the receiver in the pulse-echo arrangement shown here, with the addition of mode conversion taking place at the reflection point. With suitable signal processing and analysis, this would provide information on the relative position, size and shape of the weld pool. This could be a useful arrangement for analysing the surface of the weld pool and could identify the presence of LOF type defects. However, no information relating to the internal structure of the weld pool will be contained in the signals.

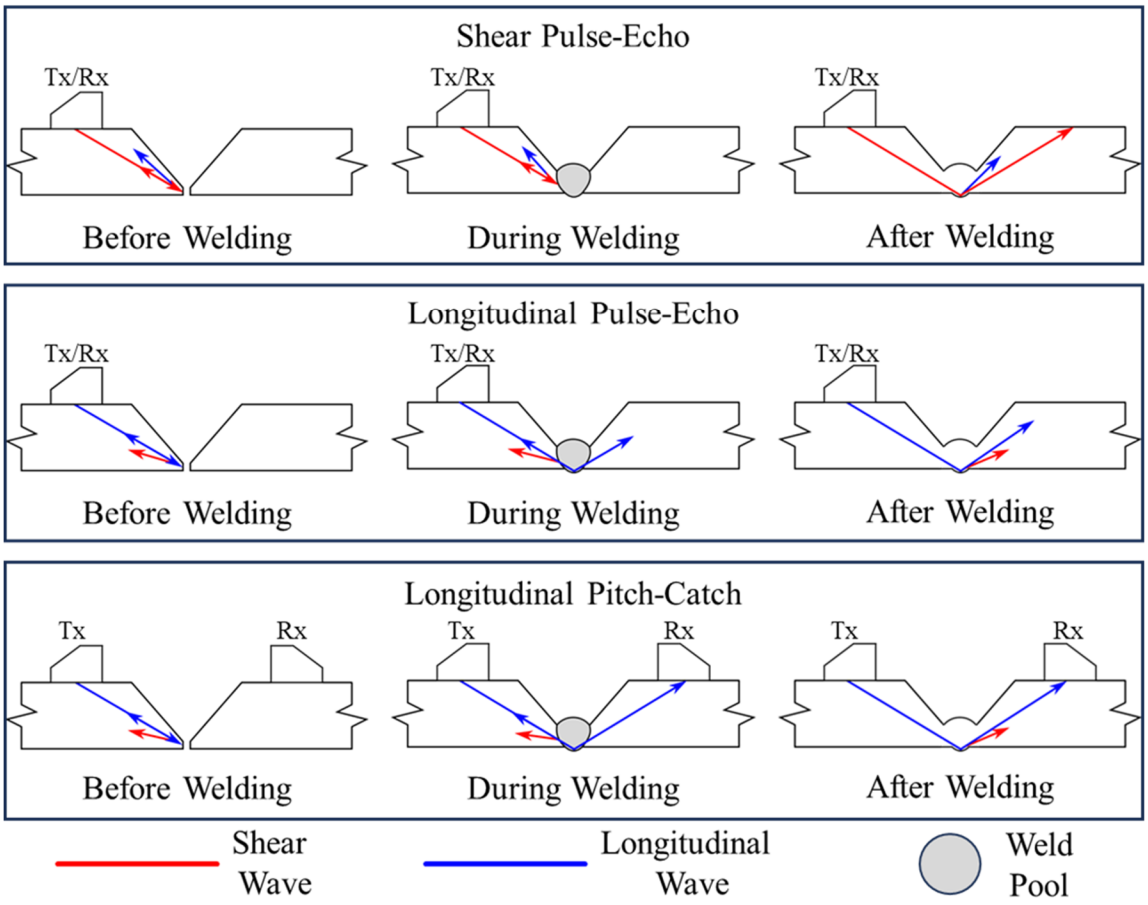

Figure 5.2. Ultrasonic wave propagation during various stages of the welding process, highlighting interface reflections and expected mode conversions

Longitudinal waves can exist within liquids and therefore there will be transmission of ultrasonic energy through the molten weld pool. This makes the pulse-echo arrangement using longitudinal waves redundant in favour of using shear waves, as only some of the incident wave will be reflected back to the receiver.

Previous literature found significant practical advantage to using a longitudinal pitch-catch arrangement [229]. Since no shear waves can exist within the liquid weld pool, there can be no mode conversion at the reflection point between liquid metal and air, therefore, the reflection coefficient for longitudinal waves within the weld pool is unity.

Given the expectation of higher attenuation of the ultrasonic waves during welding due to the extreme temperatures and thermal gradients, this conservation of energy during transmission is of great benefit. Additionally, the faster speed of longitudinal waves aids in the identification of the relevant signals, as the first arrival signal is easily identifiable as having taken the shortest, direct path between transmitter and receiver without mode conversion. The use of a longitudinal pitch-catch arrangement also offers the opportunity to collect information about the internal structure of the weld pool. These could be linked to changes in the welding process for control purposes. For these reasons, the longitudinal pitch-catch arrangement was taken forward for further experimentation, with a focus placed on the direct longitudinal signal.

5.3. Room Temperature Feasibility Study

Given the expected challenges associated with welding thermal gradients as discussed in previous chapters, the concept of monitoring liquid weld pools was first trialled at room temperature using a representative welded sample and an appropriate analogue for liquid steel. Finding an appropriate alternative for liquid steel which remains liquid at room temperature is by no means trivial. Previously, eutectic alloys such as Gallium-Indium alloys, which are liquid at room temperature, have been shown to be useful ultrasonic coupling mediums after having undergone suitable preparation [234]. However, in tests performed as part of this work with Gallium-Indium-Tin alloy, also known as Galinstan®, oxidisation of the alloy resulted in poor acoustic transmission into the liquid. Figure 5.3 shows the progressive oxidisation of Galinstan® droplets after being placed on a solid steel substrate at room temperature. During these tests, oxidisation of

the surface occurred within seconds of its exposure to air. For this reason, Galinstan® was discounted from further trials.

Figure 5.3. Oxidisation of Galinstan® droplets at room temperature

Water, whilst not the most accurate substitution for liquid steel in terms of mechanical and acoustical properties, is a viable and simple alternative to sufficiently understand the difference in signals obtained between solids and liquids. Water has been used previously in studies concerning ultrasonic liquid metal processing as an analogue for liquid metals and alloys [235,236].

Emphasis was placed on recreating the longitudinal pitch-catch wave propagation scenario depicted in Figure 5.2 as accurately as possible. Therefore, a reference staircase weld sample was fabricated as shown in Figure 5.4. This reference weld sample was manufactured so that each layer is offset from the one previous so that it contains the full range of weld cross-section profiles, allowing each to be inspected individually. By placing water in the empty portion of this sample until it was the same volume as the adjacent solid root pass, it was possible to analyse the difference in received ultrasonic signals from each scenario. The experimental set up and ultrasonic transmission paths are shown in Figure 5.4. Two inspection positions are shown as sections A-A, through solid

root weld, and B-B, through liquid water. These are representative of the "after welding" and "during welding" scenarios respectively, as depicted in Figure 5.2.

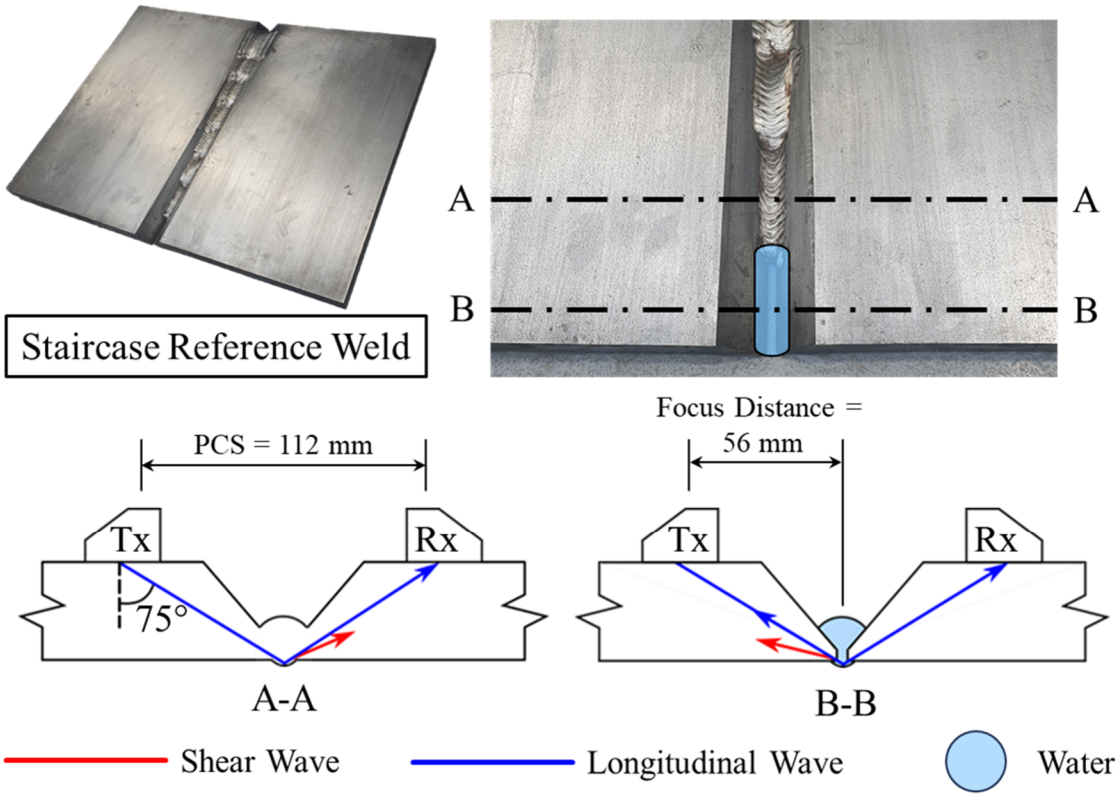

Figure 5.4. Room temperature feasibility study experiment set up

A phased array ultrasonic testing setup was used to inspect sections A-A and B-B. When designing this experiment, steps were taken to make the ultrasonic hardware suitable for in-process weld inspections as well as room temperature experiments. This ensured that once an optimised setup was found, transition to in-situ weld experiments was quick and straightforward. Two Olympus 5L64-A32 probes with Olympus SA32-ULT-N55S-IHC high-temperature wedges were used. The Probe Centre Separation (PCS) was chosen to be 112 mm, sufficient to allow travel of the weld torch between the wedges without collisions. Ultrasonic control was provided by PEAK NDT's Micropulse

6 controller, with delay laws generated to produce a 75° longitudinal beam with a focus distance of 56 mm, placing the focal point at the centre and base of the root.

5.3.1. Results & Discussion

Figure 5.5 shows the resultant A-scans through sections A-A and B-B with the direct longitudinal signal highlighted. Later arriving signals have mode conversions present, making it difficult to accurately assess the path taken between transmitter and receiver. All analysis was, therefore, performed on the first arrival signal.

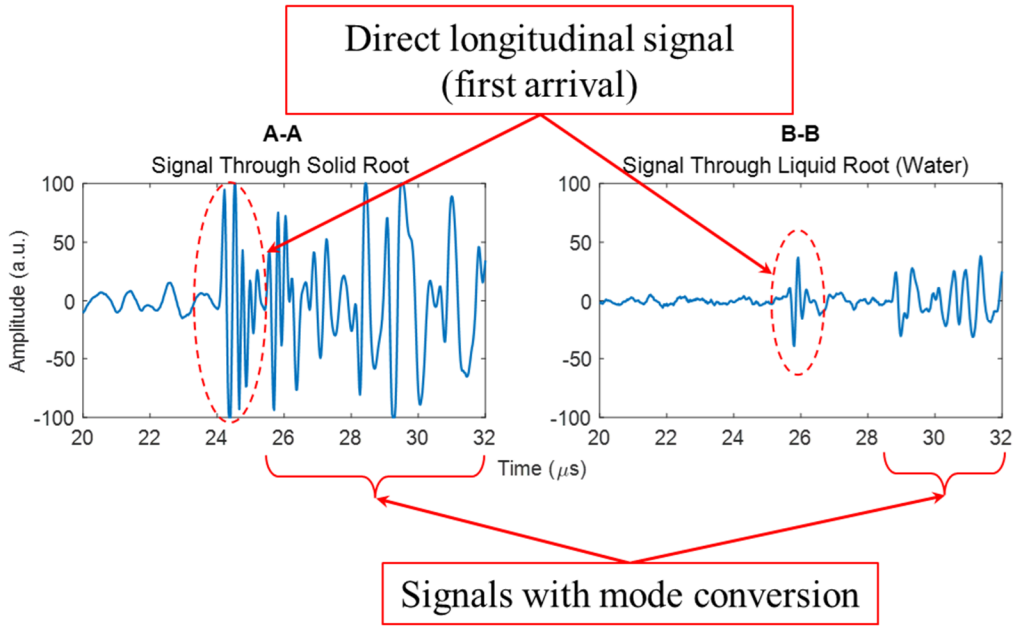

Figure 5.5. Resultant A-scans from sections A-A (liquid root) and B-B (solid root)

The key differences between the acoustic responses are the positive shift in Time-of-Flight (TOF) and the amplitude reduction. The TOF shift is attributed to the acoustic velocity difference between solid steel and water and is, therefore, directly related to the distance travelled in each medium. This is important when considering changes in weld pool size and shape which may indicate the formation of defects. The amplitude reduction

within the response from the liquid root can be attributed to the acoustic impedance mismatch between solid steel and water. A gain of 110 dB was necessary to receive usable signals through the water. This is due to the attenuation experienced through the high-temperature polymer wedges and the acoustic impedance mismatch between steel and water which results in transmission of only ~ 11% of the incident energy. At this level of gain, the signals through the solid root are saturated. It is expected that when inspecting liquid weld pools in-process that the acoustic mismatch will be minimal in comparison to these trials since liquid steel and solid steel will have more similar acoustic properties.

These room-temperature trials indicate that there are significant differences in signal responses between solid and liquid root welds which can be used to distinguish between them and drive future weld pool monitoring and process control. This conceptual experimental setup was therefore carried forward to facilitate real-time weld pool monitoring of root and hot pass welds and is introduced in the following sections.

5.4. Real-Time Weld Pool Monitoring Experimental Set-Up

Figure 5.6 [144] shows the experimental hardware used. All welding trials were performed using a GTAW process, deployed via a KUKA KR-90 robotic arm. To monitor the weld deposition visually, a XIRIS XVC-1000 High Dynamic Range (HDR) camera was used. The sample plates used were carbon steel S275 with dimensions of

100.0 × 300.0 × 15.8 mm. The weld preparation was a single-V, 90° included bevel angle with a root gap of 2.0 mm and a root face of 1.5 mm.

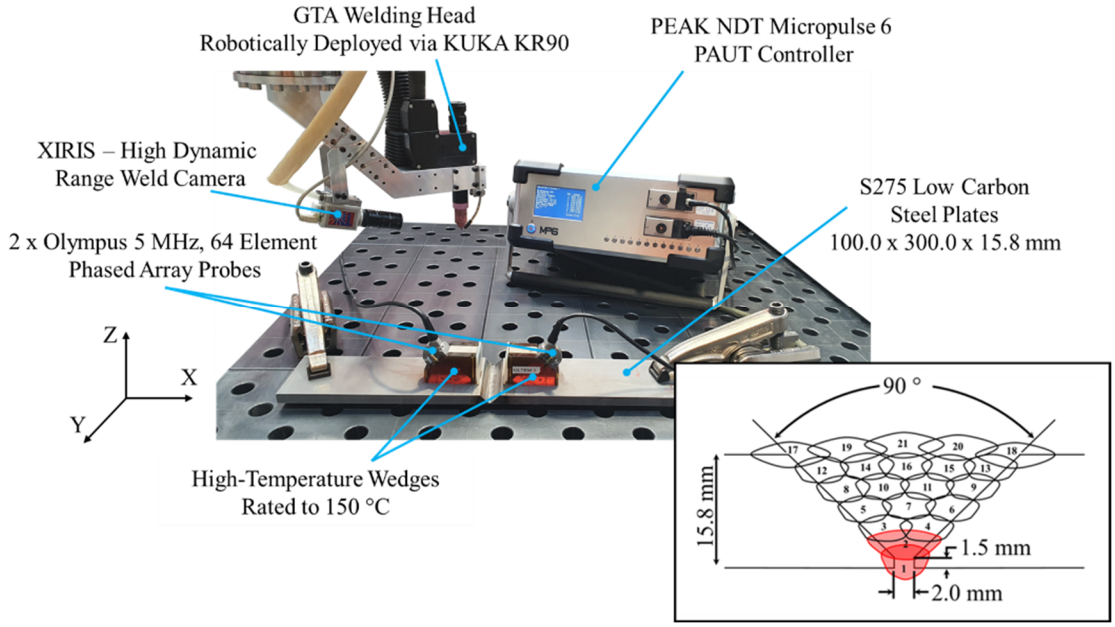

Figure 5.6. Experimental hardware set up. A 6 DOF robotic manipulator is fitted with a GTA welding head and weld camera. Olympus 5 MHz, 64 element phased array probes are used with high-temperature wedges and connected to a PEAK NDT Micropulse 6 controller. The weld bevel preparation is also shown with approximate pass structure. The passes relevant to experiments within this chapter are highlighted in red. [144]

The ultrasonic set-up was designed to provide longitudinal wave modes through the deposited weld in the same pitch-catch arrangement as used in the preliminary room temperature experiments. Detailed schematics of the ultrasonic set up are shown in Figure 5.7 [144]. To best account for the expected beam shifts due to temperature, an angular sweep from 75° to 80° with a fixed distance focus in x for all angles at the centreline of the weld preparation was implemented. In post-processing, the optimal angle could then be chosen based on the first arrival amplitude response. During all welding trials, the ultrasonic probes were fixed in position at the midpoint of the plate as shown in Figure

5.7b, with the welding torch moving between them. The probes remaining static greatly simplifies the experimental hardware and procedures whilst still providing valuable results. The probes were clamped to the surface with a high-temperature liquid couplant to provide consistent acoustic coupling.

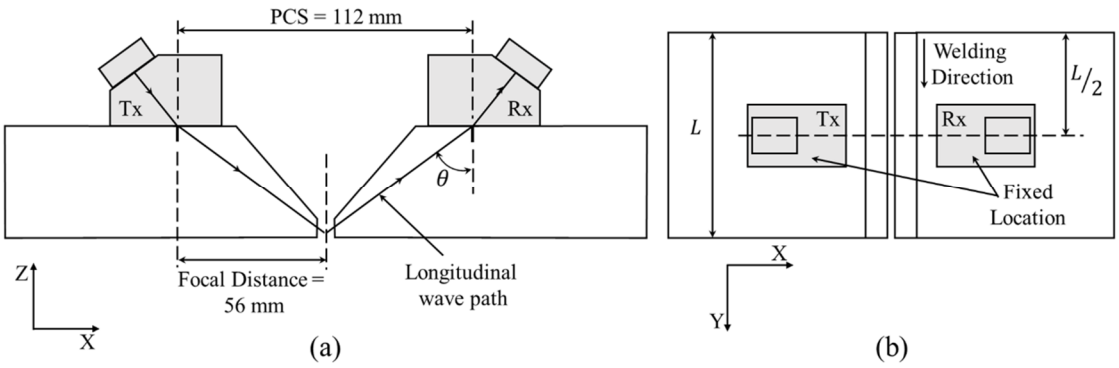

Figure 5.7. Ultrasonic hardware set up and placement shown in a (a) section view and (b) plan view. Highlighting Transmit (Tx) and Receive (Rx) probes, Probe Centre Separation (PCS) and focal distance. [144]

Four targeted experiments were designed to specifically isolate and replicate common weld fabrication scenarios, namely:

I) Bridging root weld to isolate the molten weld pool

II) Full root weld replicating standard welding practice

III) Full root weld with induced LORP

IV) Short hot pass weld to isolate the molten weld pool in upper multi-pass layers

The welding parameters were optimised over several separate trials not documented here. They are shown in Table 5.1.

*Table 5.1. Optimised welding parameters *Arc Voltage Control (AVC)*

Experiment Number	Pass	Current (A)	AVC *(V)	Travel Speed (mm/min)	Wire Feed Speed (mm/min)	Weave Amplitude (mm)	Weave Frequency (Hz)
1	Root	135	12.5	50	1000	2.2	0.3
2	Root	135	12.5	50	1000	2.2	0.3
3	Root	135	12.5	50	1000	2.2	0.3
4	Hot	220	13	100	1225	4	0.6

5.5. Experiment 1 – Bridging Root Weld to Isolate the Molten Weld Pool

In the first instance, it was important to isolate the melt pool and observe the signal changes which occur when the welding arc is started and throughout the melting and solidification processes. To do this, the experiment began with a small solid tack weld placed in the centre of the two probes. Figure 5.8 [144] shows a schematic diagram highlighting the position of the weld with respect to the ultrasonic probes. The welding arc was then ignited on top of this tack weld allowing a sufficient melt pool to be formed. This method restricts the acoustic transmission path initially through the solidified tack weld and then through the molten melt pool. Confirmation of the complete melting of this tack weld was provided visually through the XIRIS weld camera, as shown in Figure 5.9. Also shown in Figure 5.9 is the formation of small areas of silicates on the surface of the weld pool. A short root weld of length 5 mm was then performed before the arc was extinguished and the weld was allowed to solidify and cool.

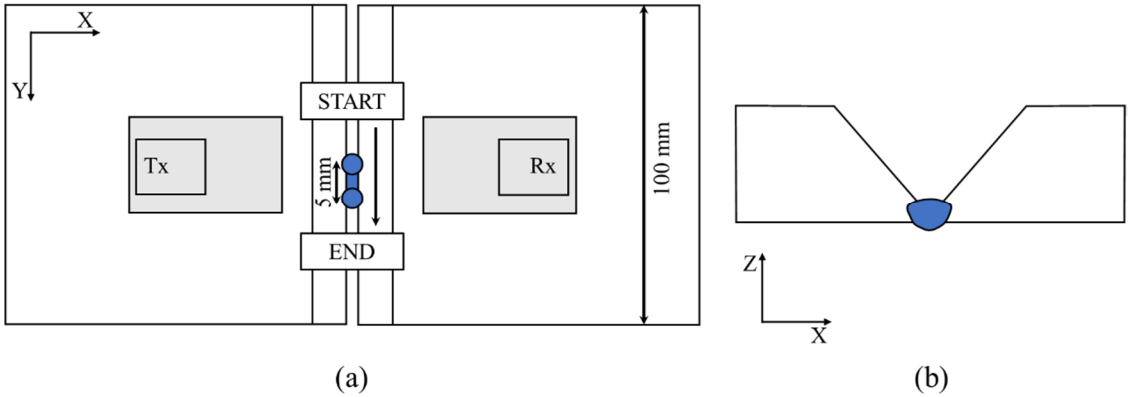

Figure 5.8. Schematic view of experiment 1 showing position of weld in relation to probes in both a (a) plan and (b) section view. [144]

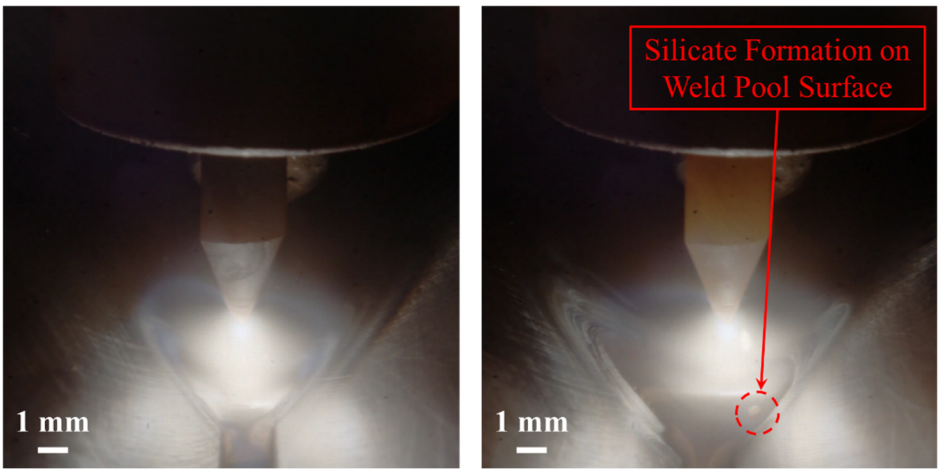

Figure 5.9. Still images taken from XIRIS weld camera showing completely molten weld pool and the formation of silicates on the weld pool surface.

5.5.1. Experiment 1 – Results & Discussion

The angle chosen from the sectorial sweep was 75° focused at the centre point between the two probes as it provided the maximum amplitude without saturation occurring within the region of interest. The first signal arrival must contain only

contributions from longitudinal waves without mode conversion. As it contains sufficient information to differentiate key characteristics of the weld pool it is the focus of the analysis. Figure 5.10a [144] shows a TOF map, displayed in the same style as a Time of Flight Diffraction (TOFD) B-scan. However, since the probes remain stationary throughout the experiment, the x-axis refers to acquisition time rather than the physical distance travelled. Figure 5.10b [144] shows individual A-scans each taken from key moments throughout the welding process as highlighted in Figure 5.10a.

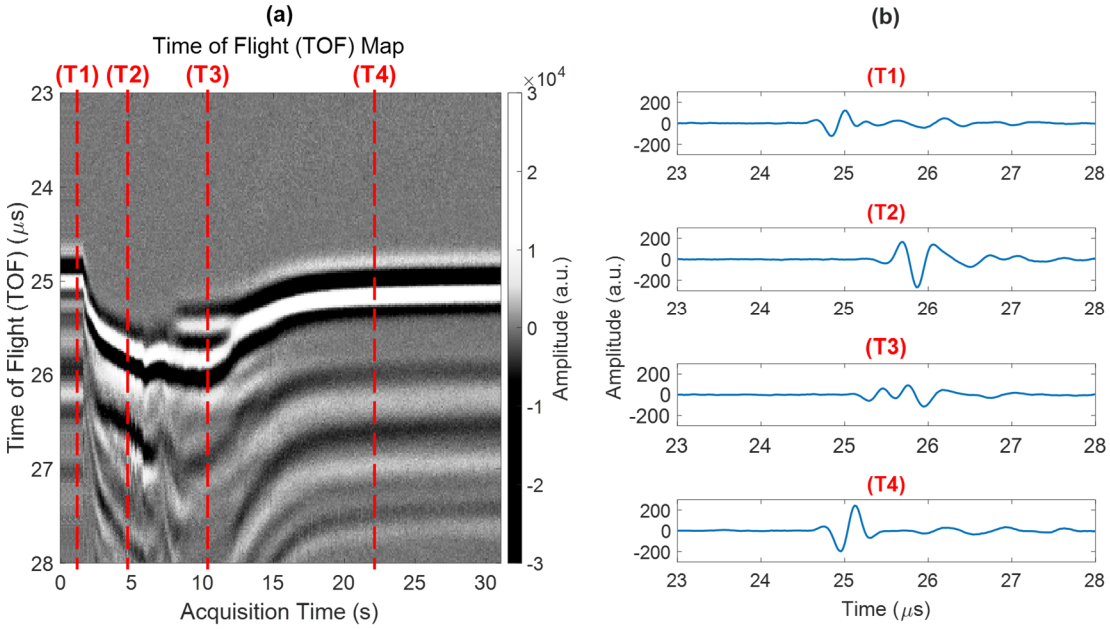

Figure 5.10. (a) Time of Flight (TOF) map of acquired ultrasonic signals (b) A-scans from highlighted acquisition times. [144]

At T1 the ultrasonic beam is travelling through the solid tack weld at an ambient temperature of 22°C. The signal has a positive phase, with the phase defined by the first peak amplitude of the signal, with a first arrival time of 24.7 μs which is in agreement with a theoretical TOF calculation given the transmission angle, distance travelled in the wedges and PCS.

Between T1 and T2, the welding arc is ignited and the tack weld is melted. At this point, the ultrasonic beam path is restricted to travel through the molten weld pool. Here, there is a clear TOF shift indicative of both the reduction in speed of sound associated with ultrasound travel through liquid and the extreme thermal gradients generated by the welding process. The signal also exhibits a 180° phase shift, now displaying a negative phase. The phase change is indicated more clearly in Figure 5.11.

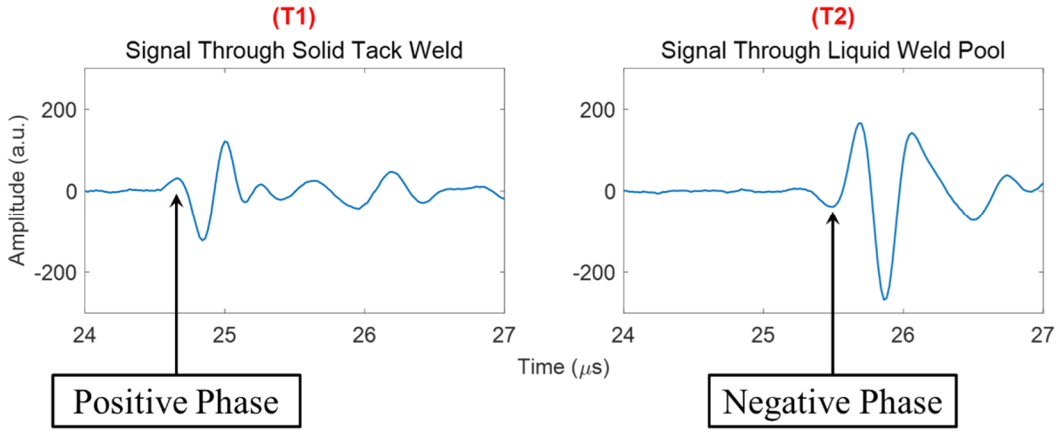

Figure 5.11. 180° phase shift between signal at T1 and T2

Between T2 and T3, the weld torch begins moving, performing a short 5 mm root weld. At time T3, an earlier arriving signal appears, indicating two ultrasonic paths being present with differing TOF's. While the use of 1D phased arrays provides accurate focusing in the X-Z plane, there is no lateral focusing capability in the X-Y plane. Now that the weld torch has moved, a shorter ultrasonic path is available through the already deposited and solidified portion of the weld, where the speed of sound is faster. This shorter path is contained in the first peak of the signal. It is also noted that the signal has returned to having a positive phase, which is in agreement with the path of the earlier arriving signal being through solidified material. The second peak is seen to be continuous

on the TOF map between T2 and T3, taking the reduced velocity path through the molten weld pool. The effect of the lateral beam spread is shown visually in Figure 5.12a [144] and related to the resultant ultrasonic signals at T3 through Figure 5.12b [144].

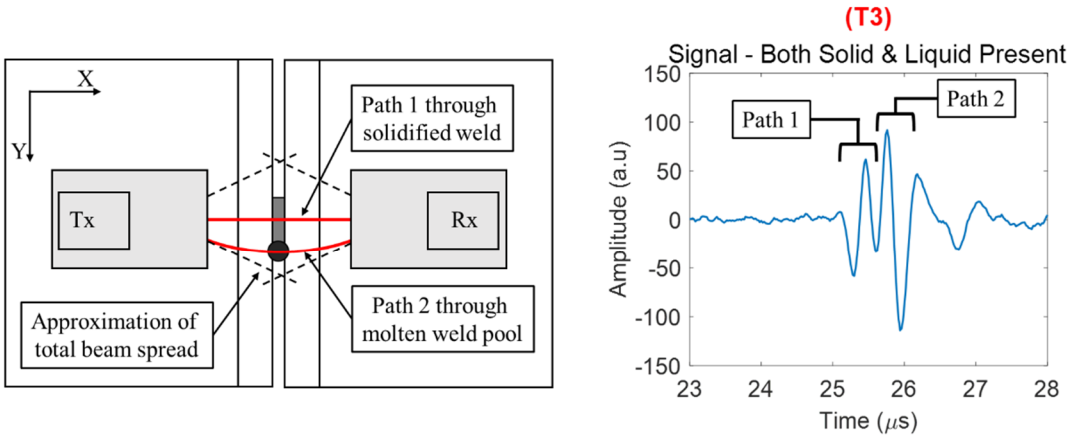

(a) (b)

Figure 5.12. Effects of lateral beam spread shown in (a) a plan view and linked to the resultant ultrasonic signals in (b) [144]

As the arc is extinguished and the weld solidifies and cools, the signal through the liquid weld pool diminishes as the volume of accessible liquid reduces. The TOF reduces during this portion of the acquisition, which can be attributed to the cooling of the weld which would result in an increase in wave velocity. Again, the signal through the solidified weld shows a positive phase.

A significant result here is the 180° phase shift displayed in the signal as the molten weld pool is established and then again as the weld solidifies. Ultrasonic phase changes are associated with a reflection from a high-to-low impedance boundary [237]. The reflection point in both the solid and liquid cases occurs at the base of the root and, with the assumption of a purely molten weld pool, the reflection interface in both cases is of high-to-low impedance (either solid steel-to-air, or molten steel-to-air). Therefore, the

expectation is that both signals should contain the same phase, having both undergone the same phase reversal during their reflection. However, the results shown here indicate the opposite. One explanation for this, requiring further investigation, could be due to the lack of shielding gas present on the underside of the root allowing formation of an oxide layer [238]. Such a layer on the underside of the molten weld pool would change the reflection interface to being low-to-high (molten steel-to-oxide layer), resulting in the ultrasonic wave no longer experiencing a phase reversal.

5.6. Experiment 2 – Full Root Pass Weld Replicating Standard Welding Practice

The next experiment looks to observe if these same signal changes are visible when depositing a full root pass weld past the stationary probes. Here, the weld is initiated at one end of the plate outside of the lateral beam spread of the probes. The weld then transits between the two probes and ends at the opposite end of the plate, with a total weld length of 90 mm. Figure 5.13 [144] shows a schematic diagram highlighting the position of the weld with respect to the ultrasonic probes.

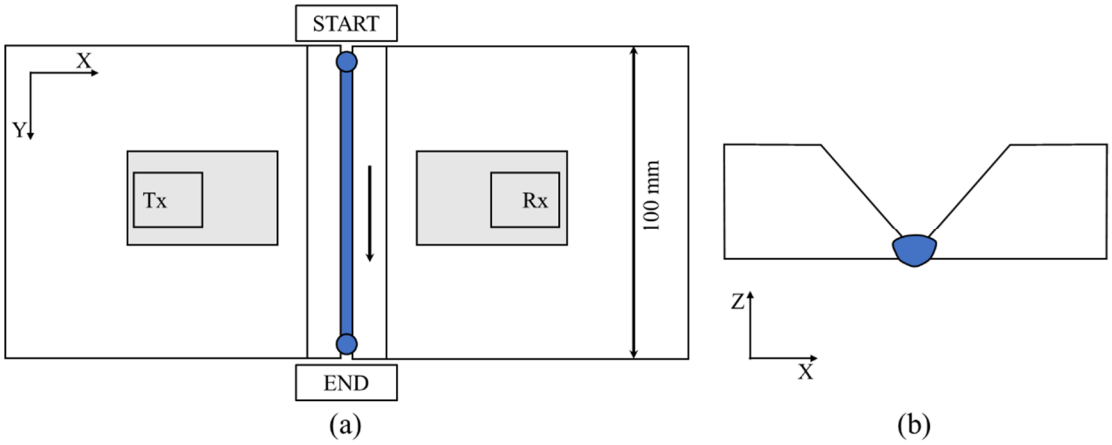

Figure 5.13. Schematic view of experiment 2 showing position of weld in relation to probes in both a (a) plan and (b) section view [144]

5.6.1. Experiment 2 – Results & Discussion

The angle chosen from the sectorial sweep was 75°, focused at the centre point of the two plates as it provided the maximum amplitude without saturation occurring within the region of interest. Figure 5.14a [144] shows the TOF map created during this experiment, with key A-scans taken from highlighted points during the welding and acquisition shown in Figure 5.14b [144].

Initially, there is no material between the plates for sound to be transmitted and therefore there is no signal visible. As previously discussed, there is no focusing capability in the X-Y plane and consequently, the initial signal through the molten weld pool is visible before the weld reaches the midpoint of the probes. At the highlighted acquisition time, T1, the emerging molten weld pool is located at the outer edges of the beam spread and therefore is lower in amplitude due to reduced beam energy. It does show the same characteristic negative phase cycle as observed in Section 5.5.1. The parabolic shape created in the TOF map highlighted by the blue dotted box in Figure 5.14a is indicative

of the molten weld pool passing across the beam spread of the probes. This changing TOF gives the illusion of varying wave speed, however, this is actually due to the change in path length. This effect is shown visually in Figure 5.15 [144].

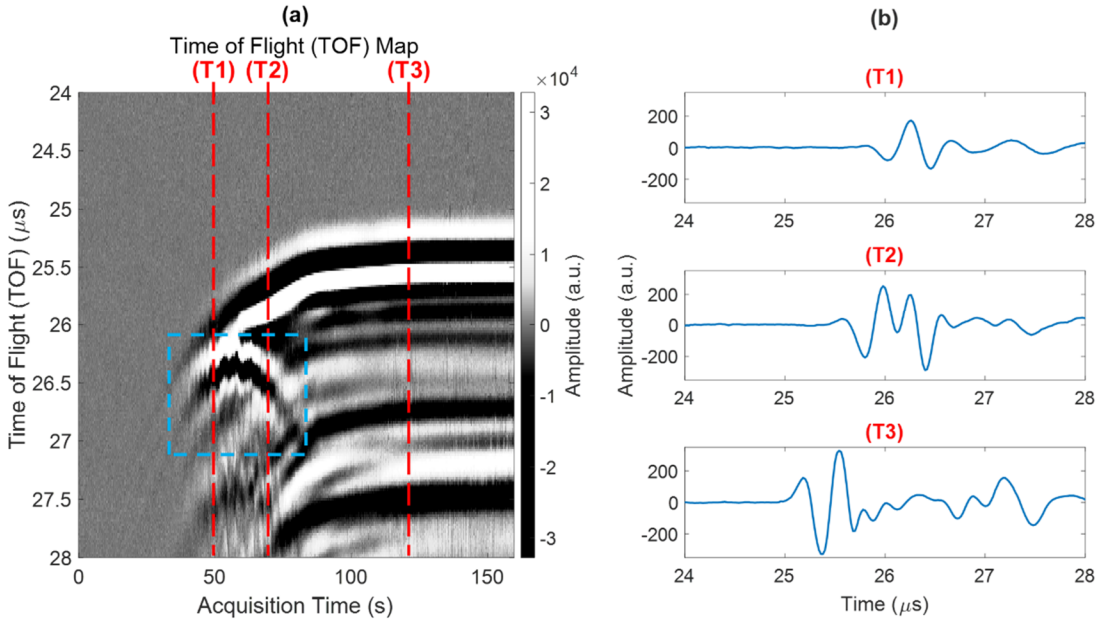

Figure 5.14. (a) Time of Flight (TOF) map of acquired ultrasonic signals (b) A-scans from highlighted acquisition times. [144]

The ultrasonic path length through the molten weld pool is minimised at point 2 in Figure 5.15 [144] and maximised at the outer extremities of the beam spread at points 1 and 3. Therefore the TOF will minimise and maximise as the molten weld pool passes across the beam spread, creating this distinctive parabolic shape as shown in Figure 5.15b. This distinctive signal shape was observed and found to be repeatable in multiple welding trials which, for brevity, are not documented here.

At time T2 in Figure 5.14a, the signal is seen to divide, again this is suggestive of there being two ultrasonic paths available. This is in agreement with the results shown in Section 5.5.1, where the first peak is attributed to the faster path through the already

deposited and solidified weld and the second to the path through the molten weld pool. Finally, as the molten weld pool moves outside of the beam spread of the probes again, the second peak diminishes in size leaving only the signal through the solidified weld. This signal again displays a positive phase and its TOF reduces as the weld cools and the wave speed increases as a consequence.

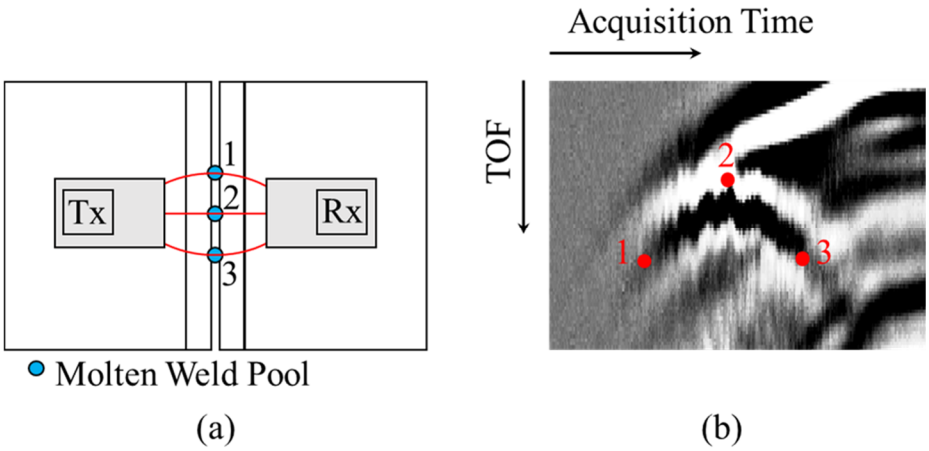

Figure 5.15. (a) Diagram showing changing path length as weld transits across probe beam spread. (b) Highlighted in TOF map. [144]

5.7. Experiment 3 – Full Root Weld with Induced Lack of Root Penetration

Here, an embedded tungsten tube (ID 1.5 mm, OD 3.0 mm) was used to induce extensive LORP. The tungsten tube was manually tacked into position at the centre of the probes and at the base of the root in order to prevent the melt pool from fusing to either root face. All deposited material will be on top of the tungsten tube. Figure 5.16 [144] shows a schematic diagram highlighting the position of the tungsten tube with respect to the ultrasonic probes.

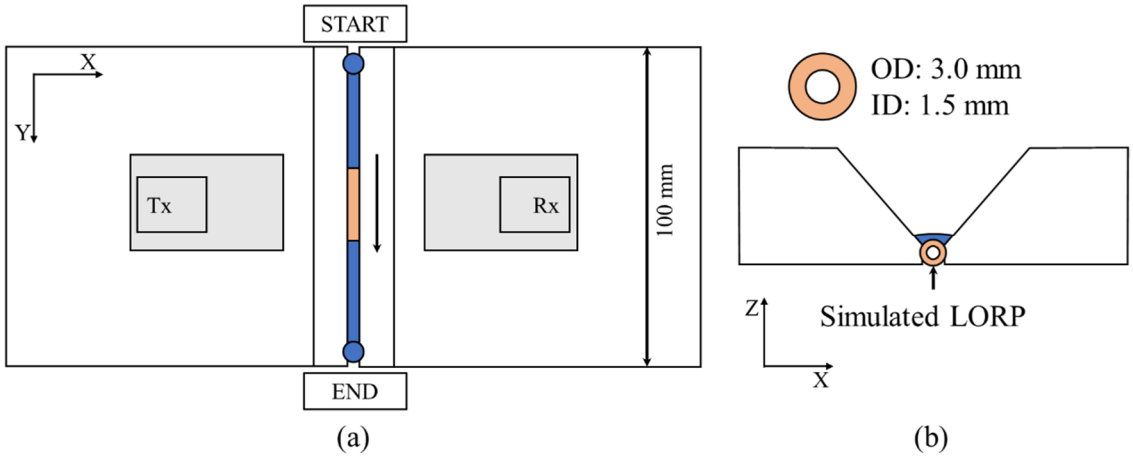

Figure 5.16. Schematic view of experiment 3 showing position of weld in relation to probes in both a (a) plan and (b) section view. [144]

5.7.1. Experiment 3 – Results & Discussion

Figure 5.17a [144] shows the underside of the weld performed in Experiment 2, Section 5.6, which displays consistent root penetration compared with the resultant LORP achieved using the tungsten tube barrier shown in Figure 5.17b [144]. This method of adding a tungsten tube was deemed successful at simulating LORP. The angle selected from the sectorial sweep was 75°, therefore the results are directly comparable with those shown for Experiment 2 in Section 5.6.1.

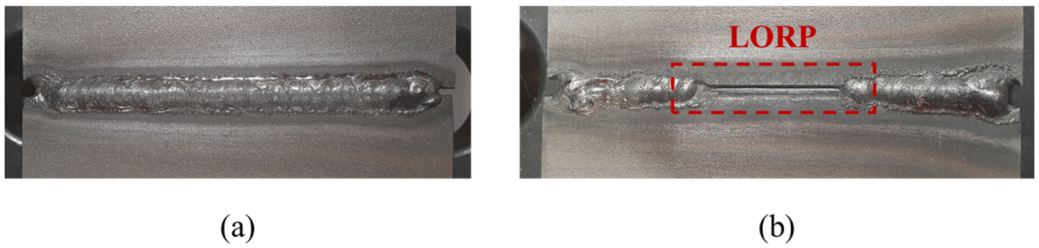

Figure 5.17. Photographs of the underside of root welds showing (a) consistent root penetration and (b) induced Lack of Root Penetration (LORP) [144]

The TOF maps for both welds are shown in Figure 5.18 [144]. The parabolic portion, highlighted as a blue dotted box in both TOF maps, indicates the time period when the molten weld pool is located within the lateral beam spread of the probe. It can be seen that while the parabolic shape is clear and uninterrupted in Figure 5.18a, it is no longer continuous in Figure 5.18b. The variation in the signal pattern visible here indicates a change in the ultrasonic path between the two probes caused by the introduction of LORP. This suggests that the proposed weld monitoring method explored here can successfully distinguish between good and poor root weld penetration.

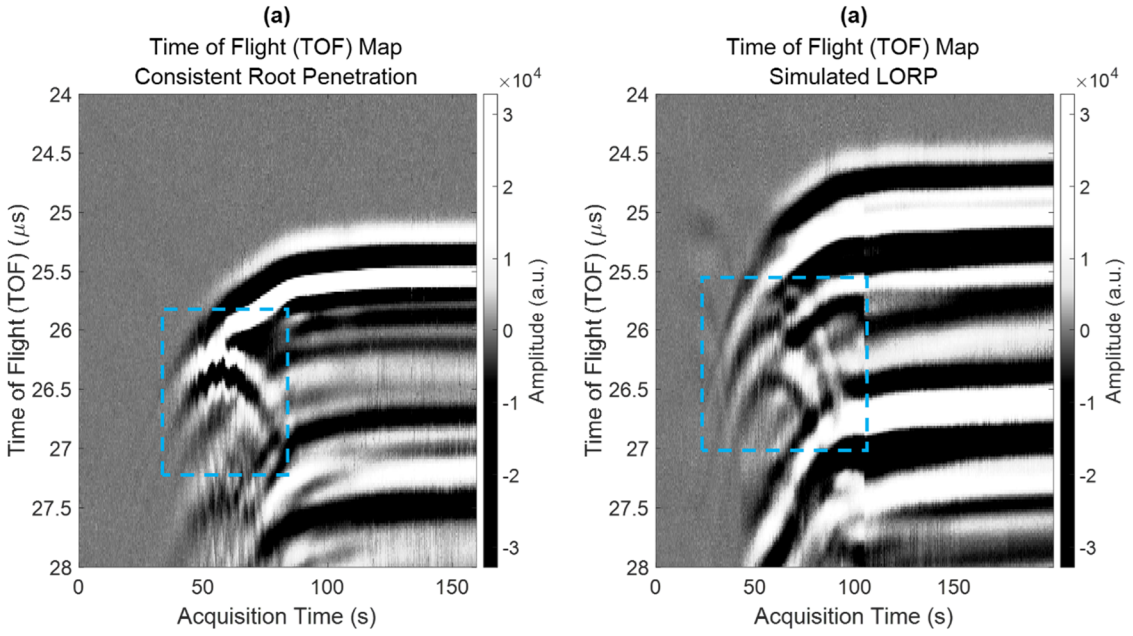

Figure 5.18. TOF maps for (a) experiment 2 with consistent root penetration and (b) experiment 3 with Lack of Root Penetration (LORP) present. [144]

There is a difference in the TOF between Figure 5.18a & b for the signal through the final solidified weld. As there was no alteration to the welding process to induce the LORP, the volume of deposited material is the same in both cases, however, the tungsten tube barrier causes the weld volume to sit higher up the weld groove. The beam focusing

with PAUT does not provide an absolute pin-point focal spot but rather a concentration of energy. This means that some ultrasound will be able to transmit across the deposited material above the tungsten, however, it will have a reduced path length resulting in a shorter TOF.

5.8. Experiment 4 – Short Hot Pass Weld to Isolate Molten Weld Pool in Upper Multi-Pass Layers

As previously discussed in Section 5.2.1 the use of phased arrays enables the concentration of ultrasonic energy to maximise the transmission through any given point. Therefore, it is possible to isolate individual passes with more accuracy than would be possible with single-element inspection systems. To investigate this, an experiment was developed to isolate the molten weld pool during the deposition of the hot pass, or second layer, of a multi-pass weld. The welded sample produced in Section 5.5 with an already-deposited root pass was used and a short hot pass was performed on top of it. The hot pass was ignited between the two probes and the weld pool was allowed to grow in size before a short 10 mm length weld was performed as shown in the schematic of Figure 5.19 [144].

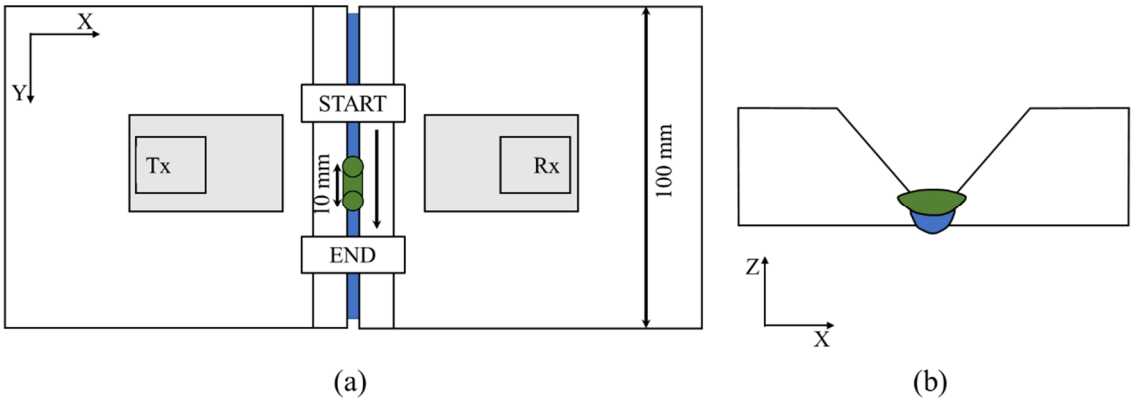

Figure 5.19. Schematic view of experiment 4 showing position of weld in relation to probes in both a (a) plan and (b) section view. [144]

5.8.1. Experiment 4 – Results & Discussion

The angle of inspection chosen was 80°, as this provided a suitable amplitude response without saturation within the region of interest. The resultant TOF map is shown in Figure 5.20 [144].The signal highlighted in Figure 5.20a & b as T1 is known to be travelling through the already deposited, room-temperature root pass. As expected, this signal shows a positive phase cycle. At an acquisition time of 22.5 s, the arc is ignited and the signal immediately divides as shown in the highlighted signal T2. Since there is surrounding solidified material present both below the hot pass and immediately before and after the arc-ignition position, there will always be two paths for the ultrasound to take. Again, these two paths can be identified in the divided signals due to their associated differing acoustic velocities. The TOF shift visible between T1 and T2 is due to the temperature gradient induced by the welding process. As the arc is extinguished and the weld begins to cool, the two peaks re-join and a single signal is seen in T3 representing the signal through the solidified material.

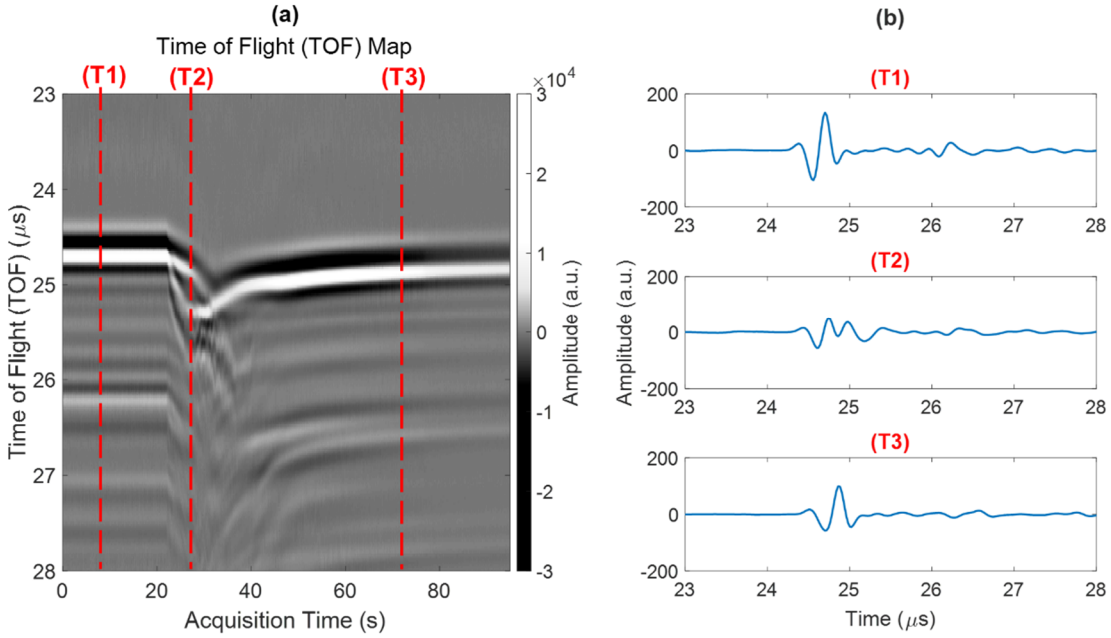

Figure 5.20. (a) Time of Flight (TOF) map of acquired ultrasonic signals (b) A-scans from highlighted acquisition times. [144]

5.9. Chapter Summary

In the work reported in this chapter, focused phased array pitch-catch inspection techniques have been implemented successfully for in-process monitoring of both root and hot pass GTAW welds. It has been proven that, despite the harsh environment that welding presents, ultrasonic waves can be propagated successfully through the molten weld pool. The resultant signals have been analysed and found to contain significant information relating to physical changes taking place within the welding process, namely the transition from solid weldment to molten weld material and back again. By recording changes in these signals and recognising the appropriate features within the signal, such as phase and TOF, it is possible to monitor the weld pool directly. These signal changes have been shown to be useful in determining weld quality with notable variations

occurring when defects such as LORP are present. Furthermore, the results indicate that through appropriate focusing and steering of the ultrasound through the use of phased arrays, it is possible to successfully isolate the signals transmitted through the molten weld pool within various layers in a multi-pass weld.

With modification to the deployment strategy to allow for in-line, concurrent inspection, the signal responses are of sufficient quality that they offer a significant opportunity to form the basis of a closed-loop control system in the future.

Chapter 6

Conclusions and Suggestions for Future Work

6.1. Conclusions

Manufacturing remains one of the fastest growing markets worldwide, largely due to the continued development and refinement of automated systems which have drastically increased productivity within the sector. However, the demands placed on the manufacturing sector to reduce costs and become more energy efficient in line with the UK's trajectory towards Net Zero mean that continued change and innovation is needed. The uptake of automation within the HVM sector, particularly through the introduction of robotic welding systems, has highlighted a significant lack of efficiency within the NDE sector. This has resulted in NDE being regarded as a major bottleneck within production environments. This is particularly true for the welding of thick section components, where earlier detection of defects during the manufacturing process would offer significant technical and commercial benefits to manufacturers and end-users. Therefore, a move to implementing innovative in-process inspection and monitoring is necessary to minimise

manufacturing schedule disruption and produce more economical and ecological components.

This thesis has looked to understand and address the practical challenges associated with the deployment of ultrasonic testing technologies at the point of manufacture. From this, new approaches for volumetric inspection of fusion welds and weld process monitoring using phased array ultrasonics have been developed and implemented. The ideas and subsequent developments discussed within this thesis demonstrate the step-change in ultrasonic inspection capabilities needed to merge NDE seamlessly with the manufacturing process.

Thermal models have been produced and experimentally validated to gain a better understanding of the changing thermal gradients produced by a GTAW process. This has been a vital step forward for the development of accurate compensation strategies for ultrasonic imaging through thermal gradients by providing the required prior knowledge [165].

A PAUT weld inspection for in-process inspection during welding has been developed and successfully deployed. This system enables continuous, dry-coupled, in-process weld inspection at temperatures compatible with most pre-and post-weld heat treatments, up to 350°C. The practical challenges associated with deployment of this system have been discussed along with the techniques developed to overcome them. Multiple imaging strategies were employed to compensate for geometrical distortion, thermal gradients, and interference. These strategies were quantified to validate their performance.

Verification of the system performance was enabled by the artificial defect-embedding process developed in Chapter 3, which provided defects of known size, shape and location within the weld volume. This provided repeatable reference reflectors which would remain consistent within the variability of the welding process. The performance of this system was quantified through comparison with traditional room temperature inspection results. The SNR values for embedded defects were calculated both in-process and post-weld and a maximum difference of 6.78 dB was found. Overall, the system performed with an average SNR value of 31.21 dB.

Finally, PAUT techniques have been implemented for use in an in-process weld pool monitoring system [144]. Ultrasonic waves were successfully propagated through the molten weld pool during multi-pass GTA welding. Through appropriate analysis of the resultant signal's phase and TOF, significant information can be obtained about the condition of the weld pool. Notable differences in signals were seen when representative defects were added during the welding process. It is proposed that with modification to the deployment strategy to allow for in-line, concurrent inspection, the signal responses are of sufficient quality that they offer significant opportunity to form the basis of a closed-loop control system.

6.2. Suggestions for Future Work

6.2.1. In-Process Ultrasonic Weld Inspection Challenges and Opportunities

The thermal modelling discussed here was successful in predicting the temperature gradients experienced during in-process inspection and was carried forward to develop the thermal compensation methods used in Chapter 4. However, the models were for a specific geometry and procedure. Therefore, a move to expand this thermal modelling technique to include a variety of industrially relevant geometries and processes will be required to progress the use of the in-process PAUT inspection system described in Chapter 4.

Furthermore, a progression towards a comprehensive weld modelling technique would assist in the advancement of the ultrasonic weld monitoring work presented in Chapter 5. In order to accurately predict the propagation of ultrasonic waves through the liquid weld pool, a robust understanding of the thermal gradients experienced is required along with accurate knowledge of ultrasonic velocity at temperature beyond 1000 °C.

The artificial tungsten pipe defect embedding strategy discussed in this chapter provides defects of known size, shape and location which is critical for inspection verification. This is particularly important for in-process inspection where there are a number of changing variables, such as extreme thermal gradients. With the development of thermal modelling techniques giving more accurate understanding of the changes in thermal gradients and their effects on the ultrasonic propagation, a move towards inserting

defects which are more representative of real defects is desirable. The most promising method for doing this is through alteration of the welding process and procedure to produce both LOF and crack-type defects. The developed methods would need to be repeatable and optimised to allow for control of defect size and shape. This work would need to be supported by the development of an appropriate calibration method for in-process PAUT systems to allow for accurate thresholding and sizing. This is discussed in more depth in Section 6.2.2.

6.2.2. In-Process Ultrasonic Phased Array Inspection During Fusion Welding

It is important that this inspection system developed here be compatible across a number of industrial welding processes. Therefore, it is intended for this system to be trialled and deployed further under processes such as Metal Inert Gas/Metal Active Gas (MIG/MAG) and SAW. Each welding process presents new and unique challenges to the deployment of the inspection system. For example, trials must be undertaken to ensure that there are no negative effects on either the hardware or imaging capability from the increased spatter and dust associated with MIG/MAG processes when compared with GTAW. Similarly, the effects of debris on the surface, such as the flux used in SAW, are unknown and must be investigated. In each case, it may be necessary to adapt the hardware with the addition of brushes or mechanisms to clean the surface of the roller-probe tyre to alleviate any negative effects.

Work must be done to establish the limits of operation of this inspection system with regards to component geometry i.e. the minimum diameter of pipe which can be successfully inspected, minimum thickness for inspection etc. Compatibility across industrially relevant geometries is also vital for future industrial applicability and adoption.

Additional future work is focused on optimisation of the system for transverse defect detection. Trials will be undertaken to establish the systems sensitivity to transverse defects, such as transverse cracking. Defect sizing is of critical importance when sentencing and assessing a component's fitness for service. This requires stringent calibration procedures which do not currently exist for in-process weld inspection approaches and, therefore, this is a significant body of future work. This work would be assisted by the development of appropriate artificial defect insertion strategies as discussed. A room-temperature calibration procedure is also desirable to allow the system to be used for final, post-weld inspections. This would enable inspection of delayed defects, such as hydrogen induced cracking, at the end of manufacture as is standard within current testing procedures.

6.2.3. In-Process Ultrasonic Phased Array Weld Pool Monitoring

The primary limitation of this proposed monitoring technique is the fixed location of the ultrasonic probes. In order to make this approach more practical, scanning of the probes in-line with the weld torch is necessary for providing continuous monitoring. Capturing data at specified increments would provide an encoded record of the welding

process with positional data provided through robotic deployment. Furthermore, concurrent monitoring will be better suited to analysing signal changes which may indicate the formation of various defects and how these may relate to changes in the welding process. The use of a weld inspection roller probe [239] would allow for smooth robotic translation of the probes whilst maintaining consistent coupling.

Another constraint upon future deployment is the use of liquid coupling which could cause contamination of the weld when combined with the movement of the probes, resulting in defects such as gross porosity. Dry-coupling techniques which use high-temperature polymers with optimised acoustical properties are a promising method to enable couplant-free deployment.

The experiments documented here are focused on the monitoring of the root and hot passes, however, with suitable modifications made to the ultrasonic focusing and deployment, the same technique may be used to monitor higher passes within multi-pass welding. Furthermore, this technique will also be applicable to welding processes other than GTAW such as GMAW and SAW.

The results shown here indicate considerable promise for quantitative analysis of the weld pool size using the TOF data contained within the ultrasonic signals. This direction of research would provide a significant step forward in progress towards automated control of the welding process using ultrasonics. This work would require accurate knowledge of the weld pool temperature and consequent speed of sound to provide accurate measurements. Currently, the available data on temperature vs. speed of ultrasonic waves is limited to 1100°C [45] and future work is being undertaken to

understand and quantify this variation. This is also tied to the development of accurate thermal models as discussed.

Further investigation is also required to accurately identify the physical mechanism which results in the 180° phase reversal observed between signals through solidified weld material and the molten weld pool.

References

[1] UK Manufacturing, The Facts 2022 n.d. https://www.makeuk.org/insights/publications/uk-manufacturing-the-facts--2022 (accessed September 3, 2023).

[2] Make UK The Manufacturer's Organisation. Manufacturing Outlook 2023 Q2. n.d.

[3] Aratani L. Pandemic caused perfect storm for supply chain crisis, experts say. The Guardian 2021.

[4] Barbieri P, Boffelli A, Elia S, Fratocchi L, Kalchschmidt M, Samson D. What can we learn about reshoring after Covid-19? Oper Manag Res 2020;13:131–6. https://doi.org/10.1007/s12063-020-00160-1.

[5] Gurvich VJ, Hussain AS. In and Beyond COVID-19: US Academic Pharmaceutical Science and Engineering Community Must Engage to Meet Critical National Needs. AAPS PharmSciTech 2020;21:153. https://doi.org/10.1208/s12249-020-01718-9.

[6] Farrer M. Global supply chain crisis fuels push to local manufacturing as China's appeal dims. The Guardian 2022.

[7] Bagchi B, Paul B. Effects of Crude Oil Price Shocks on Stock Markets and Currency Exchange Rates in the Context of Russia-Ukraine Conflict: Evidence from G7 Countries. Journal of Risk and Financial Management 2023;16:64. https://doi.org/10.3390/jrfm16020064.

[8] Russia's War on Ukraine – Topics. IEA n.d. https://www.iea.org/topics/russias-war-on-ukraine (accessed September 3, 2023).

[9] Izzeldin M, Muradoğlu YG, Pappas V, Petropoulou A, Sivaprasad S. The impact of the Russian-Ukrainian war on global financial markets. International Review of Financial Analysis 2023;87:102598. https://doi.org/10.1016/j.irfa.2023.102598.

[10] Nations U. The Climate Crisis – A Race We Can Win. United Nations n.d. https://www.un.org/en/un75/climate-crisis-race-we-can-win (accessed September 3, 2023).

[11] UK manufacturing holds key to unlocking Government's domestic and global ambitions. SMMT 2021. https://www.smmt.co.uk/2021/10/uk-manufacturing-holds-key-to-unlocking-governments-domestic-and-global-ambitions/ (accessed September 3, 2023).

[12] Richardson M. UK Government, Boeing and partners announce £80m manufacturing investment - Composites in Manufacturing 2023. https://composites.media/uk-government-boeing-and-partners-announce-80m-manufacturing-investment (accessed September 3, 2023).

[13] Glasgow's Innovation Accelerator moves forward with share of £100 million project 2023.

[14] In 1961, the First Robot Arm Punched In - IEEE Spectrum n.d. https://spectrum.ieee.org/unimation-robot (accessed September 3, 2023).

[15] The Evolution of Robotic Welding -- A historical…. TIE Industrial n.d. https://www.robots.com/articles/the-evolution-of-robotic-welding-a-historical-retrospective (accessed September 3, 2023).
[16] Bolmsjö G, Olsson M, Cederberg P. Robotic arc welding – trends and developments for higher autonomy. Industrial Robot: An International Journal 2002;29:98–104. https://doi.org/10.1108/01439910210419088.
[17] The British Standards Limited 2019. BS EN ISO 17640:2018: Non-destructive testing of welds. Ultrasonic testing. Techniques, testing levels, and assessment. 2019.
[18] The British Standards Limited 2017. BS EN ISO 19285:2017: Non-destructive testing of welds. Phased array ultrasonic testing (PAUT). Acceptance levels. 2017.
[19] International Energy Agency, IEA. Net Zero by 2050 - A Roadmap for the Global Energy Sector. n.d.
[20] Raising awareness of NDT will address skills shortage n.d. https://www.bindt.org/News/March-2015/Raising-awareness-of-ndt-will-address-skills-shortage/ (accessed November 24, 2023).
[21] How a Shrinking Workforce Affects Testing and Inspection in NDT | Quality Magazine n.d. https://www.qualitymag.com/articles/97260-how-a-shrinking-workforce-affects-testing-and-inspection-in-ndt (accessed November 24, 2023).
[22] Gap between the Supply and Demand of Well-Trained Technicians Drives NDT Training Services Market n.d. https://www.ndt.net/search/docs.php3?id=16073&msgID=0&rootID=0 (accessed November 24, 2023).
[23] Fortune Business Insights. Non-Destructive Testing [NDT] Market Size | Forecast, 2030. 2023.
[24] Peak NDT | The KTP Project- Leading the Research & Development of Flexible Automated Ultrasonic Imaging and Inspection Systems n.d. https://www.peakndt.com/case_studies/the-ktp-project-leading-the-research-development-of-flexible-automated-ultrasonic-imaging-and-inspection-systems/ (accessed November 24, 2023).
[25] What is Fusion Welding? n.d. https://www.twi-global.com/technical-knowledge/faqs/what-is-fusion-welding.aspx (accessed May 16, 2023).
[26] Weman K. 4 - Arc welding: an overview. In: Weman K, editor. Welding Processes Handbook (Second Edition), Woodhead Publishing; 2012, p. 31–50. https://doi.org/10.1533/9780857095183.31.
[27] Weman K. 1 - Introduction to welding. In: Weman K, editor. Welding Processes Handbook (Second Edition), Woodhead Publishing; 2012, p. 1–12. https://doi.org/10.1533/9780857095183.1.
[28] Norrish J. 5 - Gases for advanced welding processes. In: Norrish J, editor. Advanced Welding Processes, Woodhead Publishing; 2006, p. 58–73. https://doi.org/10.1533/9781845691707.58.
[29] Singh R. 3 - Welding and joining processes. In: Singh R, editor. Applied Welding Engineering (Third Edition), Butterworth-Heinemann; 2020, p. 157–86. https://doi.org/10.1016/B978-0-12-821348-3.00015-X.

[30] Weman K. 9 - Manual metal arc (MMA) welding with coated electrodes. In: Weman K, editor. Welding Processes Handbook (Second Edition), Woodhead Publishing; 2012, p. 99–103. https://doi.org/10.1533/9780857095183.99.
[31] Weman K. 8 - MIG/MAG welding. In: Weman K, editor. Welding Processes Handbook (Second Edition), Woodhead Publishing; 2012, p. 75–97. https://doi.org/10.1533/9780857095183.75.
[32] Lindén G. 3 - Shielding gases in MIG welding. In: Weman K, Lindén G, editors. Mig Welding Guide, Woodhead Publishing; 2006, p. 49–70. https://doi.org/10.1533/9781845691479.1.49.
[33] Norrish J. 7 - Gas metal arc welding. In: Norrish J, editor. Advanced Welding Processes, Woodhead Publishing; 2006, p. 100–35. https://doi.org/10.1533/9781845691707.100.
[34] Weman K. 10 - Submerged arc welding. In: Weman K, editor. Welding Processes Handbook (Second Edition), Woodhead Publishing; 2012, p. 105–17. https://doi.org/10.1533/9780857095183.105.
[35] What is Submerged-arc Welding? n.d. https://www.twi-global.com/technical-knowledge/faqs/faq-what-is-submerged-arc-welding.aspx (accessed May 16, 2023).
[36] Singh R. 4 - Welding automation. In: Singh R, editor. Applied Welding Engineering (Third Edition), Butterworth-Heinemann; 2020, p. 187–201. https://doi.org/10.1016/B978-0-12-821348-3.00016-1.
[37] Weman K. 6 - TIG welding. In: Weman K, editor. Welding Processes Handbook (Second Edition), Woodhead Publishing; 2012, p. 63–9. https://doi.org/10.1533/9780857095183.63.
[38] Tungsten | Uses, Properties, & Facts | Britannica n.d. https://www.britannica.com/science/tungsten-chemical-element (accessed May 16, 2023).
[39] Lucas W. CHAPTER 1 - Process fundamentals. In: Lucas W, editor. Tig and Plasma Welding, Woodhead Publishing; 1990, p. 9–24. https://doi.org/10.1533/9780857093264.1.9.
[40] Plasma Arc Welding n.d. https://www.twi-global.com/technical-knowledge/job-knowledge/plasma-arc-welding-007.aspx (accessed August 27, 2023).
[41] What is Electron Beam Welding? Process Definition and Advantages n.d. https://www.twi-global.com/technical-knowledge/faqs/faq-what-is-electron-beam-welding.aspx (accessed August 27, 2023).
[42] Weman K. 12 - Other methods of welding. In: Weman K, editor. Welding Processes Handbook (Second Edition), Woodhead Publishing; 2012, p. 133–42. https://doi.org/10.1533/9780857095183.133.
[43] Gunn RN, editor. 9 - Welding processes. Duplex Stainless Steels, Woodhead Publishing; 1997, p. 133–45. https://doi.org/10.1533/9781845698775.133.
[44] What is Resistance Welding? n.d. https://www.twi-global.com/technical-knowledge/faqs/what-is-resistance-welding.aspx (accessed August 27, 2023).
[45] Kimchi M, Phillips DH. Introduction to Resistance Spot Welding. In: Kimchi M, Phillips DH, editors. Resistance Spot Welding: Fundamentals and Applications

for the Automotive Industry, Cham: Springer International Publishing; 2023, p. 1–2. https://doi.org/10.1007/978-3-031-25783-4_1.
[46] Foster EA, Bernard R, Bolton G, Jackson-Camargo JC, Gachagan A, Mohseni E, et al. Inspection of nuclear assets with limited access using feature guided waves. NDT and E International 2022;131. https://doi.org/10.1016/j.ndteint.2022.102695.
[47] Jr RWM. Principles of Welding: Processes, Physics, Chemistry, and Metallurgy. John Wiley & Sons; 2008.
[48] American Welding Society. AWS A3.0M/A3.0:2020 An American National Standard. American Welding Society; 2020.
[49] Singh R. Designing Weldments. John Wiley & Sons; 2022.
[50] Connor LP, O'Brien RL, Oates WR, American Welding Society, editors. Welding handbook. 8th ed. Miami, FL: American Welding Society; 1987.
[51] Singh R. 9 - Weld defects and inspection. In: Singh R, editor. Applied Welding Engineering (Third Edition), Butterworth-Heinemann; 2020, p. 285–301. https://doi.org/10.1016/B978-0-12-821348-3.00027-6.
[52] The British Standards Limited 2013. BS EN ISO 6520-2:2013 Welding and allied processes. Classification of geometris imperfections in metallic materials. 2013.
[53] Porosity in Welding - Defects / Imperfections in Welds n.d. https://www.twi-global.com/technical-knowledge/job-knowledge/defects-imperfections-in-welds-porosity-042.aspx (accessed August 25, 2020).
[54] What are wormholes and how can they be prevented? n.d. https://www.twi-global.com/technical-knowledge/faqs/faq-what-are-wormholes-and-how-can-they-be-prevented.aspx (accessed May 16, 2023).
[55] A general review of geometric shape imperfections - Part 1 n.d. https://www.twi-global.com/technical-knowledge/job-knowledge/a-general-review-of-geometric-shape-imperfections-types-and-causes-part-1-067.aspx (accessed May 16, 2023).
[56] The British Standards Limited 2023. BS EN ISO 5817:2023 Welding. Fusion-welded joints in steel, nickel, titanium and their alloys (beam welding excluded). Quality levels for imperfections. 2023.
[57] Defects - Solidification Cracking n.d. https://www.twi-global.com/technical-knowledge/job-knowledge/defects-solidification-cracking-044.aspx (accessed May 16, 2023).
[58] Phan MAL, Fraser D, Gulizia S, Chen ZW. Mechanism of hot crack propagation and prevention of crack formation during electron beam powder bed fusion of a difficult-to-weld Co-Cr-Ni-W superalloy. Journal of Materials Processing Technology 2021;293:117088. https://doi.org/10.1016/j.jmatprotec.2021.117088.
[59] Lippold JC. 5 - Hydrogen Induced Cracking. Welding metallurgy and weldability, Hoboken, New Jersey: John Wiley & Sons Inc; 2015, p. 213–62.
[60] David L Bill | Mathers, Gene | Abson. Defects / Hydrogen Cracks in Steels - Identification n.d. https://www.twi-global.com/technical-knowledge/job-knowledge/defects-hydrogen-cracks-in-steels-identification-045.aspx (accessed May 16, 2023).
[61] Weld Defects / Imperfections - Incomplete Root Fusion or Penetration n.d. https://www.twi-global.com/technical-knowledge/job-knowledge/weld-defects-

imperfections-incomplete-root-fusion-or-penetration-040.aspx (accessed May 16, 2023).
[62] Tungsten Inclusion | American Welding Society Education Online n.d. https://awo.aws.org/glossary/tungsten-inclusion/ (accessed May 16, 2023).
[63] LOSWF n.d. https://www.bindt.org/What-is-NDT/Index-of-acronyms/L/loswf/ (accessed May 16, 2023).
[64] Halmshaw R. 2 - Visual Methods. Non-destructive testing. 2nd ed, London: E. Arnold; 1991, p. 5–14.
[65] Halmshaw R. 1 - Visual Methods. Introduction to the non-destructive testing of welded joints. 2nd ed, Cambridge, England: Abington; 1996, p. 1–4.
[66] Halmshaw R. 7 - Penetrant Flaw Detection. Non-destructive testing. 2nd ed, London: E. Arnold; 1991.
[67] Halmshaw R. 5 - Penetrant Methods. Introduction to the non-destructive testing of welded joints. 2nd ed, Cambridge, England: Abington; 1996, p. 104–10.
[68] Penetrant examination in Non-Destructive Examination n.d. https://www.twi-global.com/technical-knowledge/faqs/faq-what-are-the-principles-of-penetrant-examination-in-non-destructive-examination-nde.aspx (accessed May 18, 2023).
[69] Halmshaw R. 4 - Magnetic Methods. Introduction to the non-destructive testing of welded joints. 2nd ed, Cambridge, England: Abington; 1996, p. 104–10.
[70] Halmshaw R. 6 - Electrical Methods. Non-destructive testing. 2nd ed, London: E. Arnold; 1991, p. 230–61.
[71] Halmshaw R. 6 - Electrical Methods. Introduction to the non-destructive testing of welded joints. 2nd ed, Cambridge, England: Abington; 1996, p. 104–10.
[72] Chady T, Enokizono M, Sikora R, Takeuchi K, Kinoshita T. Eddy current testing of concrete structures. International Journal of Applied Electromagnetics and Mechanics 2002;15:33–7. https://doi.org/10.3233/JAE-2002-503.
[73] Zhang J, Yuan M, Song S-J, Kim H-J. Precision measurement of coating thickness on ferromagnetic tube using pulsed eddy current technique. Int J Precis Eng Manuf 2015;16:1723–8. https://doi.org/10.1007/s12541-015-0226-7.
[74] Halmshaw R. Industrial Radiology: Theory and practice. Springer Science & Business Media; 2012.
[75] Halmshaw R. 3 - Radiological Methods. Non-destructive testing. 2nd ed, London: E. Arnold; 1991, p. 15–100.
[76] The British Standards Limited 2013. BS EN ISO 5579:2013 - Non-destructive testing — Radiographic testing of metallic materials using film and X- or gamma rays — Basic rules (ISO 5579:2013). 2013.
[77] Health and Safety Executive (HSE). L121 Work with ionising radiation: Ionising Radiations Regulations 2017. Approved Code of Practice and guidance 2nd edition. TSO (The Stationery Office); 2018.
[78] What is Ultrasonic Testing and How Does it Work? n.d. https://www.twi-global.com/technical-knowledge/faqs/ultrasonic-testing.aspx (accessed May 23, 2023).
[79] Halmshaw R. 4 - Ultrasonic Testing of Materials. Non-destructive testing. 2nd ed, London: E. Arnold; 1991, p. 101–99.

[80] Krautkrämer J, Krautkrämer H. Attenuation of Ultrasonic Waves in Solids. In: Krautkrämer J, Krautkrämer H, editors. Ultrasonic Testing of Materials, Berlin, Heidelberg: Springer; 1990, p. 108–16. https://doi.org/10.1007/978-3-662-10680-8_7.
[81] Krautkrämer J, Krautkrämer H. Plane Sound Waves at Boundaries. In: Krautkrämer J, Krautkrämer H, editors. Ultrasonic Testing of Materials, Berlin, Heidelberg: Springer; 1990, p. 15–45. https://doi.org/10.1007/978-3-662-10680-8_3.
[82] Krautkrämer J, Krautkrämer H. Piezo-electric Methods of Generation and Reception of Ultrasonic Waves. In: Krautkrämer J, Krautkrämer H, editors. Ultrasonic Testing of Materials, Berlin, Heidelberg: Springer; 1990, p. 117–40. https://doi.org/10.1007/978-3-662-10680-8_8.
[83] Stratoudaki T, Clark M, Wilcox PD. Laser induced ultrasonic phased array using full matrix capture data acquisition and total focusing method. Optics Express 2016;24:21921–38. https://doi.org/10.1364/OE.24.021921.
[84] Drain CBS LE. Ultrasonic Generation by Laser. Laser Ultrasonics Techniques and Applications, Routledge; 1990.
[85] Hirao M, Ogi H. Electromagnetic Acoustic Transducers: Noncontacting Ultrasonic Measurements using EMATs. Tokyo: Springer Japan; 2017. https://doi.org/10.1007/978-4-431-56036-4.
[86] Nondestructive Evaluation Techniques : Ultrasound n.d. https://www.nde-ed.org/NDETechniques/Ultrasonics/EquipmentTrans/emats.xhtml (accessed May 23, 2023).
[87] Wavelength & Defect Detection n.d. https://www.nde-ed.org/EducationResources/CommunityCollege/Ultrasonics/Physics/defectdetect.htm (accessed September 28, 2020).
[88] Drinkwater BW, Wilcox PD. Ultrasonic arrays for non-destructive evaluation: A review. NDT & E International 2006;39:525–41. https://doi.org/10.1016/j.ndteint.2006.03.006.
[89] Clay AC, Wooh S-C, Azar L, Wang J-Y. Experimental Study of Phased Array Beam Steering Characteristics. Journal of Nondestructive Evaluation 1999;18:59–71. https://doi.org/10.1023/A:1022618321612.
[90] Holmes C, Drinkwater B, Wilcox P. The post-processing of ultrasonic array data using the total focusing method. Insight - Non-Destructive Testing and Condition Monitoring 2004;46(11):677–80.
[91] The British Standards Limited 2017. BS EN ISO 5577:2017 - Non-destructive testing — Ultrasonic testing — Vocabulary. 2017.
[92] C-Scan n.d. https://www.bindt.org/What-is-NDT/Index-of-acronyms/C/C-Scan/ (accessed August 29, 2023).
[93] Norrish J. 10 - Monitoring and control of welding processes. In: Norrish J, editor. Advanced Welding Processes, Woodhead Publishing; 2006, p. 179–217. https://doi.org/10.1533/9781845691707.179.
[94] Cheng Y, Yu R, Zhou Q, Chen H, Yuan W, Zhang Y. Real-time sensing of gas metal arc welding process – A literature review and analysis. Journal of

Manufacturing Processes 2021;70:452–69. https://doi.org/10.1016/j.jmapro.2021.08.058.
[95] Li X, Li X, Ge SS, Khyam MO, Luo C. Automatic Welding Seam Tracking and Identification. IEEE Transactions on Industrial Electronics 2017;64:7261–71. https://doi.org/10.1109/TIE.2017.2694399.
[96] Muhammad J, Altun H, Abo-Serie E. Welding seam profiling techniques based on active vision sensing for intelligent robotic welding. Int J Adv Manuf Technol 2017;88:127–45. https://doi.org/10.1007/s00170-016-8707-0.
[97] Zhang YM. Part 2 Chapter 6: Weld Seam Monitoring. Real-Time Weld Process Monitoring, Elsevier; 2008, p. 129–86.
[98] Loukas C, Warner V, Jones R, MacLeod CN, Vasilev M, Mohseni E, et al. A sensor enabled robotic strategy for automated defect-free multi-pass high-integrity welding. Materials & Design 2022;224. https://doi.org/10.1016/j.matdes.2022.111424.
[99] Kiddee P, Fang Z, Tan M. An automated weld seam tracking system for thick plate using cross mark structured light. Int J Adv Manuf Technol 2016;87:3589–603. https://doi.org/10.1007/s00170-016-8729-7.
[100] Le J, Zhang H, Chen X. Right-angle fillet weld tracking by robots based on rotating arc sensors in GMAW. Int J Adv Manuf Technol 2017;93:605–16. https://doi.org/10.1007/s00170-017-0536-2.
[101] Nayak NR, Ray A. 2 - An Overview of Seam Tracking Tehcnologies. Intelligent Seam Tracking for Robotic Welding, Springer Science & Business Media; 2013, p. 8–30.
[102] Maqueira B, Umeagukwu CI, Jarzynski J. Application of ultrasonic sensors to robotic seam tracking. IEEE Transactions on Robotics and Automation 1989;5:337–44. https://doi.org/10.1109/70.34769.
[103] Estochen EL, Neuman CP, Prinz FB. Application of Acoustic Sensors to Robotic Seam Tracking. IEEE Transactions on Industrial Electronics 1984;IE-31:219–24. https://doi.org/10.1109/TIE.1984.350038.
[104] Mahajan A, Figueroa F. Intelligent seam tracking using ultrasonic sensors for robotic welding. Robotica 1997;15:275–81. https://doi.org/10.1017/S0263574797000313.
[105] Huang Y, Chen S. Introduction. In: Huang Y, Chen S, editors. Key Technologies of Intelligentized Welding Manufacturing: The Spectral Diagnosis Technology for Pulsed Gas Tungsten Arc Welding of Aluminum Alloys, Singapore: Springer; 2020, p. 1–25. https://doi.org/10.1007/978-981-13-7549-1_1.
[106] Tarn J, Huissoon JP. Developing psycho-acoustic experiments in gas metal arc welding. vol. 2, 2005, p. 1112-1117 Vol. 2. https://doi.org/10.1109/ICMA.2005.1626707.
[107] Lv N, Chen S. Investigation on Acoustic Signals for On-line Monitoring of Welding. In: Tarn T-J, Chen S-B, Fang G, editors. Robotic Welding, Intelligence and Automation, vol. 88, Berlin, Heidelberg: Springer Berlin Heidelberg; 2011, p. 235–43. https://doi.org/10.1007/978-3-642-19959-2_29.

[108] Huang W, Yang S, Lin D, Kovacevic R. Monitoring of spatters by using microphone during gas tungsten arc welding of galvanized high-strength steel DP 980, 2009, p. 159–66.
[109] Lv N, Xu Y, Zhong J, Chen H, Wang J, Chen S. Research on detection of welding penetration state during robotic GTAW process based on audible arc sound. Industrial Robot: An International Journal 2013;40:474–93. https://doi.org/10.1108/IR-09-2012-417.
[110] Szłapa P, Marczak W. Arc welding noise assessment from the measured ultrasound pressure levels: Part I: The metal active gas welding. Ultrasonics 2018;90:71–9. https://doi.org/10.1016/j.ultras.2018.06.011.
[111] Griffin JM, Jones S, Perumal B, Perrin C. Investigating the Detection Capability of Acoustic Emission Monitoring to Identify Imperfections Produced by the Metal Active Gas (MAG) Welding Process. Acoustics 2023;5:714–45. https://doi.org/10.3390/acoustics5030043.
[112] Spence C, Parise C, Chen Y-C. The Colavita Visual Dominance Effect. The Neural Bases of Multisensory Processes, CRC Press/Taylor & Francis; 2012.
[113] Kassuba T, Klinge C, Hölig C, Röder B, Siebner HR. Vision holds a greater share in visuo-haptic object recognition than touch. NeuroImage 2013;65:59–68. https://doi.org/10.1016/j.neuroimage.2012.09.054.
[114] Xiris Weld Monitoring Cameras - High Dynamic Range Weld Cameras n.d. https://www.xiris.com/weld-monitoring-cameras/ (accessed August 30, 2023).
[115] Welding Camera | Welding Vision System | Welding Analysis. Cavitar Ltd - See What You Have Missed n.d. https://www.cavitar.com/product/cavitar-welding-camera/ (accessed August 30, 2023).
[116] CaviAdn. Cavitar Ltd. Announce Partnership in Weld Viewing Technology. Cavitar Ltd - See What You Have Missed 2022. https://www.cavitar.com/library/cavitar-ltd-and-intertest-inc-announce-partnership-in-weld-viewing-technology/ (accessed August 30, 2023).
[117] Yu R, Kershaw J, Wang P, Zhang Y. Real-time recognition of arc weld pool using image segmentation network. Journal of Manufacturing Processes 2021;72:159–67. https://doi.org/10.1016/j.jmapro.2021.10.019.
[118] Pietrzak KA, Packer SM. Vision-Based Weld Pool Width Control. Journal of Engineering for Industry 1994;116:86–92. https://doi.org/10.1115/1.2901813.
[119] Brzakovic D, Khani DT, Awad B. A vision system for monitoring weld pool. Proceedings 1992 IEEE International Conference on Robotics and Automation, 1992, p. 1609–14 vol.2. https://doi.org/10.1109/ROBOT.1992.220022.
[120] Font comas T, Diao C, Ding J, Williams S, Zhao Y. A Passive Imaging System for Geometry Measurement for the Plasma Arc Welding Process. IEEE Transactions on Industrial Electronics 2017;64:7201–9. https://doi.org/10.1109/TIE.2017.2686349.
[121] Chen Z. Monitoring weld pool surface and penetration using reversed electrode images. Welding Journal 2017;96.
[122] Chen Z, Chen J, Feng Z. Welding penetration prediction with passive vision system. Journal of Manufacturing Processes 2018;36:224–30. https://doi.org/10.1016/j.jmapro.2018.10.009.

[123] Alfaro SCA, Franco FD. Exploring Infrared Sensoring for Real Time Welding Defects Monitoring in GTAW. Sensors 2010;10:5962–74. https://doi.org/10.3390/s100605962.
[124] Bicknell A, Smith JS, Lucas J. Infrared sensor for top face monitoring of weld pools. Meas Sci Technol 1994;5:371–8. https://doi.org/10.1088/0957-0233/5/4/008.
[125] The British Standards Limited 2017. BS EN ISO 19285:2017: Non-destructive testing of welds. Phased array ultrasonic testing (PAUT). Acceptance levels. 2017.
[126] The British Standards Limited 2019. BS EN ISO 17640:2018: Non-destructive testing of welds. Ultrasonic testing. Techniques, testing levels, and assessment. 2019.
[127] High-Temperature Ultrasonic Testing n.d. https://www.olympus-ims.com/en/high-temperature-ultrasonic-testing/ (accessed September 20, 2023).
[128] HotSense^{TM} UT Transducers. Ionix Advanced Technologies n.d. https://ionixadvancedtechnologies.co.uk/products/inspection-probe/ (accessed September 20, 2023).
[129] Bouchy S, Zednik RJ, Belanger P. Ultrasonic Transducers for In-Service Inspection and Continuous Monitoring in High-Temperature Environments. Sensors 2023;23:3520. https://doi.org/10.3390/s23073520.
[130] 9.5 High Temperature Testing | Olympus IMS n.d. https://www.olympus-ims.com/en/ndt-tutorials/flaw-detection/high-temp-testing/ (accessed September 20, 2023).
[131] HotSense^{TM} Time of Flight Diffraction – Ionix. Ionix Advanced Technologies n.d. https://ionixadvancedtechnologies.co.uk/products/hotsense-tofd/ (accessed September 20, 2023).
[132] Vithanage RKW, Mohseni E, Qiu Z, MacLeod C, Javadi Y, Sweeney N, et al. A phased array ultrasound roller probe for automated in-process/interpass inspection of multipass welds. IEEE Transactions on Industrial Electronics 2020. https://doi.org/10.1109/TIE.2020.3042112.
[133] Cook RH, Skelton RP. Environment-Dependence of the Mechanical Properties of Metals at High Temperature. International Metallurgical Reviews 1974;19:199–222. https://doi.org/10.1179/imtlr.1974.19.1.199.
[134] Gardner L, Insausti A, Ng KT, Ashraf M. Elevated temperature material properties of stainless steel alloys. Journal of Constructional Steel Research 2010;66:634–47. https://doi.org/10.1016/j.jcsr.2009.12.016.
[135] Huang L, Li G-Q, Wang X-X, Zhang C, Choe L, Engelhardt M. High Temperature Mechanical Properties of High Strength Structural Steels Q550, Q690 and Q890. Fire Technol 2018;54:10.1007/s10694-018-0760–9. https://doi.org/10.1007/s10694-018-0760-9.
[136] Scruby CB, Moss BC. Non-contact ultrasonic measurements on steel at elevated temperatures. NDT & E International 1993;26:177–88. https://doi.org/10.1016/0963-8695(93)90472-7.

[137] Mineo C, Lines D, Cerniglia D. Generalised bisection method for optimum ultrasonic ray tracing and focusing in multi-layered structures. Ultrasonics 2021;111:106330. https://doi.org/10.1016/j.ultras.2020.106330.
[138] Dewhurst RJ, Edwards C, McKie ADW, Palmer SB. A remote laser system for ultrasonic velocity measurement at high temperatures. Journal of Applied Physics 1988;63:1225–7. https://doi.org/10.1063/1.339987.
[139] Foster EA, Sweeney NE, Nicolson E, Singh J, Rizwan MK, Lines D, et al. Thermal compensation of ultrasonic transmit and receive data for steel welded plates at the point of manufacture. NDT & E International 2023;137:102812. https://doi.org/10.1016/j.ndteint.2023.102812.
[140] Javadi Y, Mohseni E, MacLeod CN, Lines D, Vasilev M, Mineo C, et al. Continuous monitoring of an intentionally-manufactured crack using an automated welding and in-process inspection system. Materials & Design 2020;191:108655. https://doi.org/10.1016/j.matdes.2020.108655.
[141] Lines DI, Javadi Y, Mohseni E, Vasilev M, MacLeod CN, Vithanage RW, et al. Flexible robotic cell for in-process inspection of multi-pass welds n.d.
[142] Silber FA, Ganglbauer C. Ultrasonic testing of hot welds. Non-Destructive Testing 1970;3:429–32. https://doi.org/10.1016/0029-1021(70)90156-8.
[143] Javadi Y, Mohseni E, MacLeod CN, Lines D, Vasilev M, Mineo C, et al. High-temperature in-process inspection followed by 96-h robotic inspection of intentionally manufactured hydrogen crack in multi-pass robotic welding. International Journal of Pressure Vessels and Piping 2021;189. https://doi.org/10.1016/j.ijpvp.2020.104288.
[144] Sweeney NE, Parke S, Lines D, Loukas C, Vasilev M, Pierce SG, et al. In-process phased array ultrasonic weld pool monitoring. NDT & E International 2023;137:102850. https://doi.org/10.1016/j.ndteint.2023.102850.
[145] Javadi Y, Sweeney NE, Mohseni E, MacLeod CN, Lines D, Vasilev M, et al. In-process calibration of a non-destructive testing system used for in-process inspection of multi-pass welding. Materials and Design 2020;195. https://doi.org/10.1016/j.matdes.2020.108981.
[146] COMSOL Documentation n.d. https://doc.comsol.com/6.1/docserver/#!/com.comsol.help.comsol/helpdesk/helpdesk.html (accessed September 20, 2023).
[147] Zacharia T, Vitek JM, Goldak JA, DebRoy TA, Rappaz M, Bhadeshia HKDH. Modeling of fundamental phenomena in welds. Modelling Simul Mater Sci Eng 1995;3:265–88. https://doi.org/10.1088/0965-0393/3/2/009.
[148] Ushio M. Mathematical modelling of flow in the weld pool. Welding International 1991;5:679–83. https://doi.org/10.1080/09507119109454436.
[149] Yang Z, Debroy T. Modeling macro-and microstructures of Gas-Metal-Arc Welded HSLA-100 steel. Metall Mater Trans B 1999;30:483–93. https://doi.org/10.1007/s11663-999-0082-x.
[150] info@micro-epsilon.de M-EM-. Sensors & Measurement Systems | Micro-Epsilon. Micro-Epsilon Messtechnik n.d. https://www.micro-epsilon.co.uk (accessed September 20, 2023).
[151] Çengel YA. Heat and mass transfer. 2000.

[152] Prabhu KMM. Window Functions and Their Applications in Signal Processing. Taylor & Francis; 2014. https://doi.org/10.1201/9781315216386.
[153] V P. Experimental and computed temperature histories in gas tungsten arc welding of thin plates. Welding Journal Research Supplement 1969;48:296–305.
[154] Arora H, Singh R, Brar GS. Thermal and structural modelling of arc welding processes: A literature review. Measurement and Control 2019;52:955–69. https://doi.org/10.1177/0020294019857747.
[155] Stenbacka N. On arc efficiency in gas tungsten arc welding. Soldag Insp 2013;18:380–90. https://doi.org/10.1590/S0104-92242013000400010.
[156] What is the difference between heat input and arc energy? n.d. https://www.twi-global.com/technical-knowledge/faqs/faq-what-is-the-difference-between-heat-input-and-arc-energy.aspx (accessed December 6, 2023).
[157] Collings N, Wong KY, Guile AE. Efficiency of tungsten-inert-gas arcs in very-high-speed welding. Proceedings of the Institution of Electrical Engineers 1979;126:276–80. https://doi.org/10.1049/piee.1979.0071.
[158] Dutta P, Joshi Y, Franche C. Determination of gas tungsten arc welding efficiencies. Experimental Thermal and Fluid Science 1994;9:80–9.
[159] DuPont JN, Marder AR. Thermal efficiency of arc welding processes. Welding Journal 1995;74.
[160] Fuerschbach PW, Knorovsky G. A study of melting efficiency in plasma arc and gas tungsten arc welding : a method for selecting optimal weld schedules to minimize net heat input is derived frm calorimetric measuremts. Welding Journal 1991.
[161] Vasilev M. Sensor-enabled robotics for ultrasonic NDE. University of Strathclyde., 2021. https://doi.org/10.48730/WF52-X747.
[162] Vasilev M, MacLeod CN, Loukas C, Javadi Y, Vithanage RKW, Lines D, et al. Sensor-Enabled Multi-Robot System for Automated Welding and In-Process Ultrasonic NDE. Sensors 2021;21:5077. https://doi.org/10.3390/s21155077.
[163] Type K Thermocouple - Type K Thermocouples - K Type Thermocouples - K Type Thermocouple n.d. https://www.thermocoupleinfo.com/type-k-thermocouple.htm (accessed November 20, 2023).
[164] Calculating Thermocouple Measurement Error in DMM/Switch Temperature Measurement Systems - NI n.d. https://knowledge.ni.com/KnowledgeArticleDetails?id=kA03q000000x0dBCAQ&l=en-GB (accessed November 20, 2023).
[165] Foster EA, Sweeney NE, Nicolson E, Singh J, Rizwan MK, Lines D, et al. Thermal compensation of ultrasonic transmit and receive data for steel welded plates at the point of manufacture. NDT & E International 2023;137:102812. https://doi.org/10.1016/j.ndteint.2023.102812.
[166] Consonni M, Howse D, Wee CF, Schneider C. Production of joints welded with realistic defects. Welding International 2014;28:535–46. https://doi.org/10.1080/09507116.2012.753263.
[167] Ammirato F, Shankar R, Edelmann X. Ultrasonic examination of dissimilar-metal welds in BWR and PWR plants. International Journal of Pressure Vessels and Piping 1988;35:37–56. https://doi.org/10.1016/0308-0161(88)90090-7.

[168] Würschig T. Acoustic Response of Reference Notches: Derivation of Acceptance Criteria for Automated Ultrasonic Testing Based on the Correlation Between Defect Quality and Effective Defect Size. J Nondestruct Eval 2022;41:16. https://doi.org/10.1007/s10921-022-00847-4.
[169] Koskinen A, Haapalainen J, Virkkunen I, Kemppainen M. Differences in Ultrasonic Indications - Thermal Fatigue Cracks and EDM Notches. E-Journal of Nondestructive Testing 2012;17.
[170] Camerini CG, Campos LB, Silva VMA, Castro DSV, Santos RWF, Rebello JMA, et al. Correlation of eddy current signals obtained from EDM notches and fatigue cracks. Journal of Materials Research and Technology 2019;8:4843–8. https://doi.org/10.1016/j.jmrt.2019.08.031.
[171] Larson BF, Lo CCH, Nakagawa N. INVESTIGATION OF THE EFFECTS OF NOTCH WIDTH ON EDDY CURRENT RESPONSE AND COMPARISON OF SIGNALS FROM NOTCHES AND CRACKS. AIP Conference Proceedings 2010;1211:1973–9. https://doi.org/10.1063/1.3362351.
[172] Virkkunen I, Kempainen M, Ostermeyer H, Paussu R, Dunhill T. Grown cracks for NDT development and qualification. Insight - Non-Destructive Testing and Condition Monitoring 2009;51:271–8. https://doi.org/10.1784/insi.2009.51.5.271.
[173] Kong Y, Bennett CJ, Hyde CJ. A review of non-destructive testing techniques for the in-situ investigation of fretting fatigue cracks. Materials & Design 2020;196:109093. https://doi.org/10.1016/j.matdes.2020.109093.
[174] Javadi Y, Vasilev M, MacLeod CN, Pierce SG, Su R, Mineo C, et al. Intentional weld defect process: From manufacturing by robotic welding machine to inspection using TFM phased array. AIP Conference Proceedings 2019;2102:040011. https://doi.org/10.1063/1.5099761.
[175] Tungsten - Element information, properties and uses | Periodic Table n.d. https://www.rsc.org/periodic-table/element/74/tungsten (accessed November 8, 2023).
[176] Javadi Y, MacLeod CN, Pierce SG, Gachagan A, Lines D, Mineo C, et al. Ultrasonic phased array inspection of a Wire + Arc Additive Manufactured (WAAM) sample with intentionally embedded defects. Additive Manufacturing 2019;29. https://doi.org/10.1016/j.addma.2019.100806.
[177] Mohseni E, Javadi Y, Sweeney NE, Lines D, MacLeod CN, Vithanage RKW, et al. Model-assisted ultrasonic calibration using intentionally embedded defects for in-process weld inspection. Materials and Design 2021;198. https://doi.org/10.1016/j.matdes.2020.109330.
[178] Jones JE, Luo Y. CHAPTER 10 - Pre- and Post-Weld Heat Treatment. In: Olson DL, Dixon R, Liby AL, editors. Materials Processing: Theory and Practices, vol. 8, Elsevier; 1990, p. 293–323. https://doi.org/10.1016/B978-0-444-87427-6.50016-2.
[179] Khan M, Dewan MW, Sarkar MdZ. Effects of welding technique, filler metal and post-weld heat treatment on stainless steel and mild steel dissimilar welding joint. Journal of Manufacturing Processes 2021;64:1307–21. https://doi.org/10.1016/j.jmapro.2021.02.058.

[180] Shafeek HI, Gadelmawla ES, Abdel-Shafy AA, Elewa IM. Automatic inspection of gas pipeline welding defects using an expert vision system. NDT & E International 2004;37:301–7. https://doi.org/10.1016/j.ndteint.2003.10.004.
[181] Dai W, Li D, Tang D, Jiang Q, Wang D, Wang H, et al. Deep learning assisted vision inspection of resistance spot welds. Journal of Manufacturing Processes 2021;62:262–74. https://doi.org/10.1016/j.jmapro.2020.12.015.
[182] Scruby CB. Some applications of laser ultrasound. Ultrasonics 1989;27:195–209. https://doi.org/10.1016/0041-624X(89)90043-7.
[183] Cho H, Ogawa S, Takemoto M. Non-contact laser ultrasonics for detecting subsurface lateral defects. NDT & E International 1996;29:301–6. https://doi.org/10.1016/S0963-8695(96)00033-3.
[184] Lukacs P, Davis G, Stratoudaki T, Javadi Y, Pierce G, Gachagan A. Remote, volumetric ultrasonic imaging of defects using two-dimensional laser induced phased arrays: 2021 48th Annual Review of Progress in Quantitative Nondestructive Evaluation, QNDE 2021. Proceedings of 2021 48th Annual Review of Progress in Quantitative Nondestructive Evaluation, QNDE 2021 2022. https://doi.org/10.1115/qnde2021-74694.
[185] Lukacs P, Davis G, Stratoudaki T, Williams S, MacLeod CN, Gachagan A. Remote ultrasonic imaging of a wire arc additive manufactured Ti-6AI-4V component using laser induced phased array: IEEE International Instrumentation and Measurement Technology Conference (I2MTC), 2021. 2021 IEEE International Instrumentation and Measurement Technology Conference (I2MTC) 2021:1–6. https://doi.org/10.1109/I2MTC50364.2021.9459823.
[186] Cerniglia D, Montinaro N. Defect Detection in Additively Manufactured Components: Laser Ultrasound and Laser Thermography Comparison. Procedia Structural Integrity 2018;8:154–62. https://doi.org/10.1016/j.prostr.2017.12.016.
[187] Zarei A, Pilla S. Laser ultrasonics for nondestructive testing of composite materials and structures: A review. Ultrasonics 2024;136:107163. https://doi.org/10.1016/j.ultras.2023.107163.
[188] Vasilev M, MacLeod CN, Loukas C, Javadi Y, Vithanage RKW, Lines D, et al. Sensor-Enabled Multi-Robot System for Automated Welding and In-Process Ultrasonic NDE. Sensors 2021;21:5077. https://doi.org/10.3390/s21155077.
[189] Javadi Y, Macleod C, Lines D, Vasilev M, Mohseni E, Foster E, et al. IN-PROCESS INSPECTION OF MULTI-PASS ROBOTIC WELDING 2019.
[190] Macleod CN, Dobie G, Pierce SG, Summan R, Morozov M. Machining-Based Coverage Path Planning for Automated Structural Inspection. IEEE Transactions on Automation Science and Engineering 2018;15:202–13. https://doi.org/10.1109/TASE.2016.2601880.
[191] Loukas C, Williams V, Jones R, Vasilev M, MacLeod CN, Dobie G, et al. A cost-function driven adaptive welding framework for multi-pass robotic welding. Journal of Manufacturing Processes 2021;67:545–61. https://doi.org/10.1016/j.jmapro.2021.05.004.
[192] Williams M. Chapter 11 - Process automation platforms. In: Perlmutter BA, editor. Integration and Optimization of Unit Operations, Elsevier; 2022, p. 239–47. https://doi.org/10.1016/B978-0-12-823502-7.00024-4.

[193] Vithanage RKW, Mohseni E, Lines D, Loukas C, Foster E, MacLeod CN, et al. Development of a phased array ultrasound roller probe for inspection of wire + arc additive manufactured components. Journal of Manufacturing Processes 2022;80:765–74. https://doi.org/10.1016/j.jmapro.2022.06.045.
[194] Siricharoenpanich A, Wiriyasart S, Naphon P. Study on the thermal dissipation performance of GPU cooling system with nanofluid as coolant. Case Studies in Thermal Engineering 2021;25:100904. https://doi.org/10.1016/j.csite.2021.100904.
[195] Zhang Z, Wang X, Yan Y. A review of the state-of-the-art in electronic cooling. E-Prime - Advances in Electrical Engineering, Electronics and Energy 2021;1:100009. https://doi.org/10.1016/j.prime.2021.100009.
[196] Vithanage RKW, Macleod CN, Lines DIA. AWESIM - PAUT Hardware. PCT/GB2022/053360 (Patent Application), 2023.
[197] Tant KMM, Galetti E, Mulholland AJ, Curtis A, Gachagan A. Effective grain orientation mapping of complex and locally anisotropic media for improved imaging in ultrasonic non-destructive testing. Inverse Problems in Science and Engineering 2020;28:1694–718. https://doi.org/10.1080/17415977.2020.1762596.
[198] Zhang J, Drinkwater B, Wilcox P. Efficient immersion imaging of components with nonplanar surfaces. IEEE Trans Ultrason Ferroelectr Freq Control 2014;61:1284–95. https://doi.org/10.1109/TUFFC.2014.3035.
[199] Mineo C, Cerniglia D, Mohseni E. Solving ultrasonic ray tracing in parts with multiple material layers through Root-Finding methods. Ultrasonics 2022;124:106747. https://doi.org/10.1016/j.ultras.2022.106747.
[200] Vithanage RKW, Macleod CN, Lines DIA, Smart M, Smart P, Swain R, et al. AWESIM - PAUT Software Methodology. PCT/GB2022/053365 (Patent Application), 2023.
[201] The British Standards Limited 2010. BS EN 10029:2010: Hot-rolled steel plates 3 mm thick or above - Tolerances on dimensions and shape. 2010.
[202] The British Standards Limited 2003. BS EN 10297-1:2003: Seamless circular steel tubes for mechanical and general engineering purposes - Technical delivery conditions - Part 1: Non-alloy and alloy steel tubes. 2003.
[203] Cheng Y, Yu R, Zhou Q, Chen H, Yuan W, Zhang Y. Real-time sensing of gas metal arc welding process – A literature review and analysis. Journal of Manufacturing Processes 2021;70:452–69. https://doi.org/10.1016/j.jmapro.2021.08.058.
[204] Li X, Li X, Ge SS, Khyam MO, Luo C. Automatic Welding Seam Tracking and Identification. IEEE Transactions on Industrial Electronics 2017;64:7261–71. https://doi.org/10.1109/TIE.2017.2694399.
[205] Muhammad J, Altun H, Abo-Serie E. Welding seam profiling techniques based on active vision sensing for intelligent robotic welding. Int J Adv Manuf Technol 2017;88:127–45. https://doi.org/10.1007/s00170-016-8707-0.
[206] Zhang YM. Part 2 Chapter 6: Weld Seam Monitoring. Real-Time Weld Process Monitoring, Elsevier; 2008, p. 129–86.

[207] Le J, Zhang H, Chen X. Right-angle fillet weld tracking by robots based on rotating arc sensors in GMAW. Int J Adv Manuf Technol 2017;93:605–16. https://doi.org/10.1007/s00170-017-0536-2.
[208] Font comas T, Diao C, Ding J, Williams S, Zhao Y. A Passive Imaging System for Geometry Measurement for the Plasma Arc Welding Process. IEEE Transactions on Industrial Electronics 2017;64:7201–9. https://doi.org/10.1109/TIE.2017.2686349.
[209] Peng G, Chang B, Wang G, Gao Y, Hou R, Wang S, et al. Vision sensing and feedback control of weld penetration in helium arc welding process. Journal of Manufacturing Processes 2021;72:168–78. https://doi.org/10.1016/j.jmapro.2021.10.023.
[210] Brzakovic D, Khani DT, Awad B. A vision system for monitoring weld pool. Proceedings 1992 IEEE International Conference on Robotics and Automation, 1992, p. 1609–14 vol.2. https://doi.org/10.1109/ROBOT.1992.220022.
[211] Chen Z, Chen J, Feng Z. Welding penetration prediction with passive vision system. Journal of Manufacturing Processes 2018;36:224–30. https://doi.org/10.1016/j.jmapro.2018.10.009.
[212] Alfaro SCA, Franco FD. Exploring Infrared Sensoring for Real Time Welding Defects Monitoring in GTAW. Sensors 2010;10:5962–74. https://doi.org/10.3390/s100605962.
[213] Bicknell A, Smith JS, Lucas J. Infrared sensor for top face monitoring of weld pools. Meas Sci Technol 1994;5:371–8. https://doi.org/10.1088/0957-0233/5/4/008.
[214] The British Standards Limited 2013. BS EN ISO 5579:2013: Non-Destructive Testing - Radiographic testing of metallic materials using film and X- or gamma rays - Basic Rules. 2013.
[215] Health and Safety Executive (HSE). L121 Work with ionising radiation: Ionising Radiations Regulations 2017. Approved Code of Practice and guidance 2nd edition. TSO (The Stationery Office); 2018.
[216] Shull PJ. Chapter 5: Eddy Current. : Theory, Techniques, and Applications, Boca Raton: CRC Press; 2016, p. 108. https://doi.org/10.1201/9780203911068.
[217] Maev RG, Chertov AM, Paille JM, Ewasyshyn FJ. Ultrasonic in-process monitoring and feedback of resistance spot weld quality. US20170021446A1, 2017.
[218] Maev R, Chertov A, Regalado W, Karloff A, Tchipilko A, Lichaa P, et al. In-Line Inspection of Resistance Spot Welds for Sheet Metal Assembly. Welding Journal 2014;93:58–62.
[219] Andreoli AF, Chertov AM, Maev RG. Correlation between Peel Test and Real Time Ultrasonic Test for Quality Diagnosis in Resistance Spot Welding. Soldag Insp 2016;21:282–9. https://doi.org/10.1590/0104-9224/SI2103.04.
[220] Stocco D, Maev RG, Chertov AM, Batalha GF. Comparison between in - line ultrasonic monitoring of the spot weld quality and conventional NDT methods applied in a real production environment. Proceedings 2008.

[221] Lui A, Karloff AC, Maev RGr. M-scan cross-sectional imaging of resistance spot welds during welding. 2012 IEEE International Ultrasonics Symposium, 2012, p. 2392–5. https://doi.org/10.1109/ULTSYM.2012.0598.
[222] Lui A, Karloff AC, Chertov AM, Maev RGr, Boni E, Tortoli P. Application of a programmable multi-channel ultrasonic system for in-line quality monitoring of spot welds. 2011 IEEE International Ultrasonics Symposium, 2011, p. 524–6. https://doi.org/10.1109/ULTSYM.2011.0126.
[223] Vasilev M, MacLeod C, Galbraith W, Javadi Y, Foster E, Dobie G, et al. Non-contact in-process ultrasonic screening of thin fusion welded joints. Journal of Manufacturing Processes 2021;64:445–54. https://doi.org/10.1016/j.jmapro.2021.01.033.
[224] Kelly SP, Farlow R, Hayward G. Applications of through-air ultrasound for rapid NDE scanning in the aerospace industry. IEEE Transactions on Ultrasonics, Ferroelectrics, and Frequency Control 1996;43:581–91. https://doi.org/10.1109/58.503780.
[225] Nomura K, Deno S, Matsuida T, Otaki S, Asai S. In situ measurement of ultrasonic behavior during lap spot welding with laser ultrasonic method. NDT & E International 2022;130:102662. https://doi.org/10.1016/j.ndteint.2022.102662.
[226] Mi B, Ume C. Real-Time Weld Penetration Depth Monitoring With Laser Ultrasonic Sensing System. Journal of Manufacturing Science and Engineering 2005;128:280–6. https://doi.org/10.1115/1.2137747.
[227] Cerniglia D, Montinaro N. Defect Detection in Additively Manufactured Components: Laser Ultrasound and Laser Thermography Comparison. Procedia Structural Integrity 2018;8:154–62. https://doi.org/10.1016/j.prostr.2017.12.016.
[228] Vasilev M, MacLeod C, Javadi Y, Pierce G, Gachagan A. Feed forward control of welding process parameters through on-line ultrasonic thickness measurement. Journal of Manufacturing Processes 2021;64:576–84. https://doi.org/10.1016/j.jmapro.2021.02.005.
[229] Stares IJ, Duffil C, Ogilvy JA, Scruby CB. On-line weld pool monitoring and defect detection using ultrasonic. NDT International 1990;23:195–200. https://doi.org/10.1016/0308-9126(90)91601-O.
[230] Halmshaw R. 4.2 Waves at Boundaries. Non-destructive testing. 2nd ed, London: E. Arnold; 1991, p. 106–23.
[231] Drinkwater BW, Wilcox PD. Ultrasonic arrays for non-destructive evaluation: A review. NDT & E International 2006;39:525–41. https://doi.org/10.1016/j.ndteint.2006.03.006.
[232] Clay AC, Wooh S-C, Azar L, Wang J-Y. Experimental Study of Phased Array Beam Steering Characteristics. Journal of Nondestructive Evaluation 1999;18:59–71. https://doi.org/10.1023/A:1022618321612.
[233] EXTENDE. CIVA NDE Software Manual 2020.
[234] Culjat MO, Singh RS, White SN, Neurgaonkar RR, Brown ER. Evaluation of gallium-indium alloy as an acoustic couplant for high-impedance, high-frequency applications. Acoustics Research Letters Online 2005;6:125–30. https://doi.org/10.1121/1.1903025.

[235] Lebon GSB, Tzanakis I, Pericleous K, Eskin D, Grant PS. Ultrasonic liquid metal processing: The essential role of cavitation bubbles in controlling acoustic streaming. Ultrasonics Sonochemistry 2019;55:243–55. https://doi.org/10.1016/j.ultsonch.2019.01.021.
[236] Tzanakis I, Lebon GSB, Eskin DG, Pericleous KA. Characterizing the cavitation development and acoustic spectrum in various liquids. Ultrasonics Sonochemistry 2017;34:651–62. https://doi.org/10.1016/j.ultsonch.2016.06.034.
[237] Krautkrämer J, Krautkrämer H. 2. Plane Sound Waves at Boundaries. Ultrasonic Testing of Materials, Springer Science & Business Media; 2013, p. 23–45.
[238] Mills KC, Keene BJ. Factors affecting variable weld penetration. International Materials Reviews 1990;35:185–216. https://doi.org/10.1179/095066090790323966.
[239] Vithanage RKW, Mohseni E, Qiu Z, MacLeod C, Javadi Y, Sweeney N, et al. A phased array ultrasound roller probe for automated in-process/interpass inspection of multipass welds. IEEE Transactions on Industrial Electronics 2020:1–1. https://doi.org/10.1109/TIE.2020.3042112.

Appendix A – Full Thermal Modellin□Results

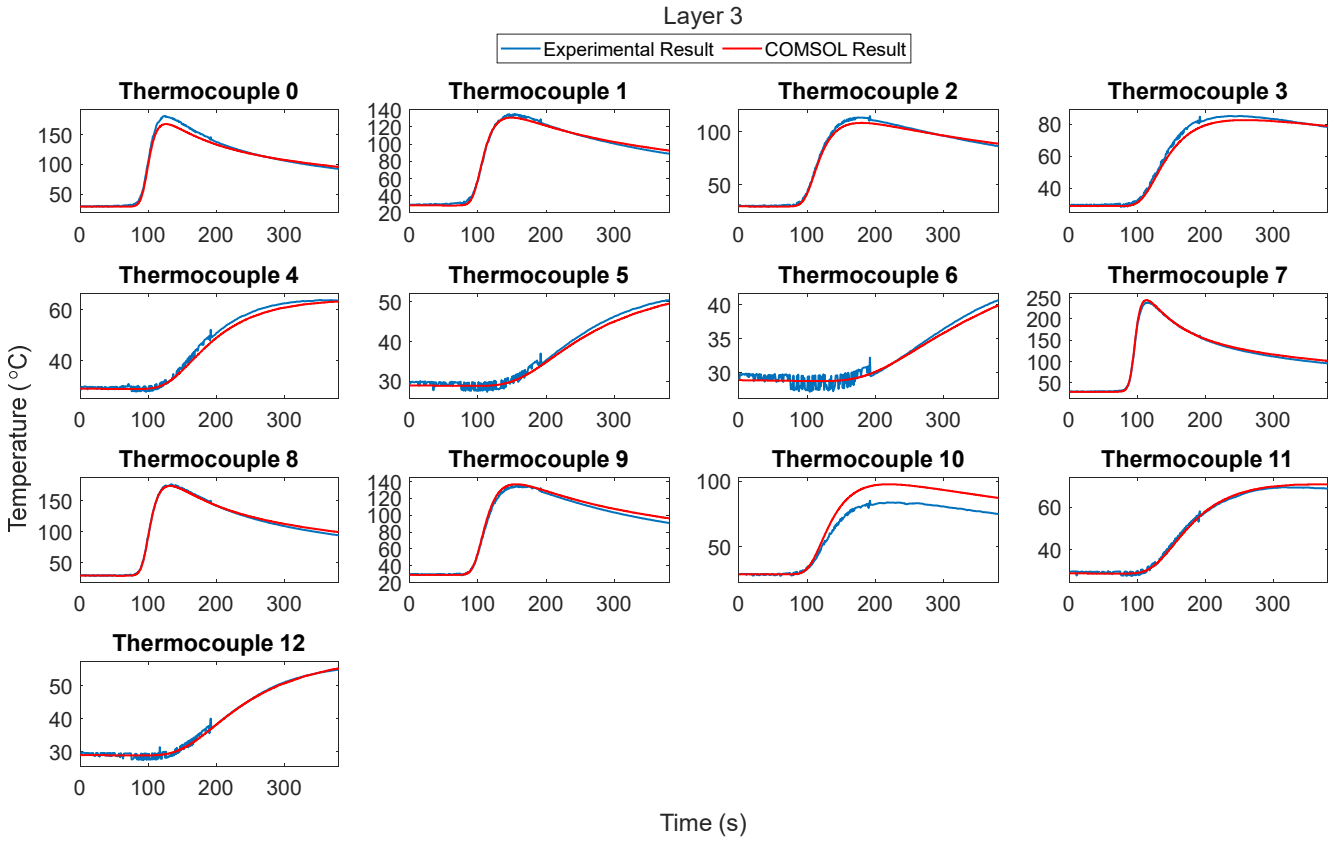

Figure A 1. Comparison of experimental and COMSOL data for layer 3 of welding

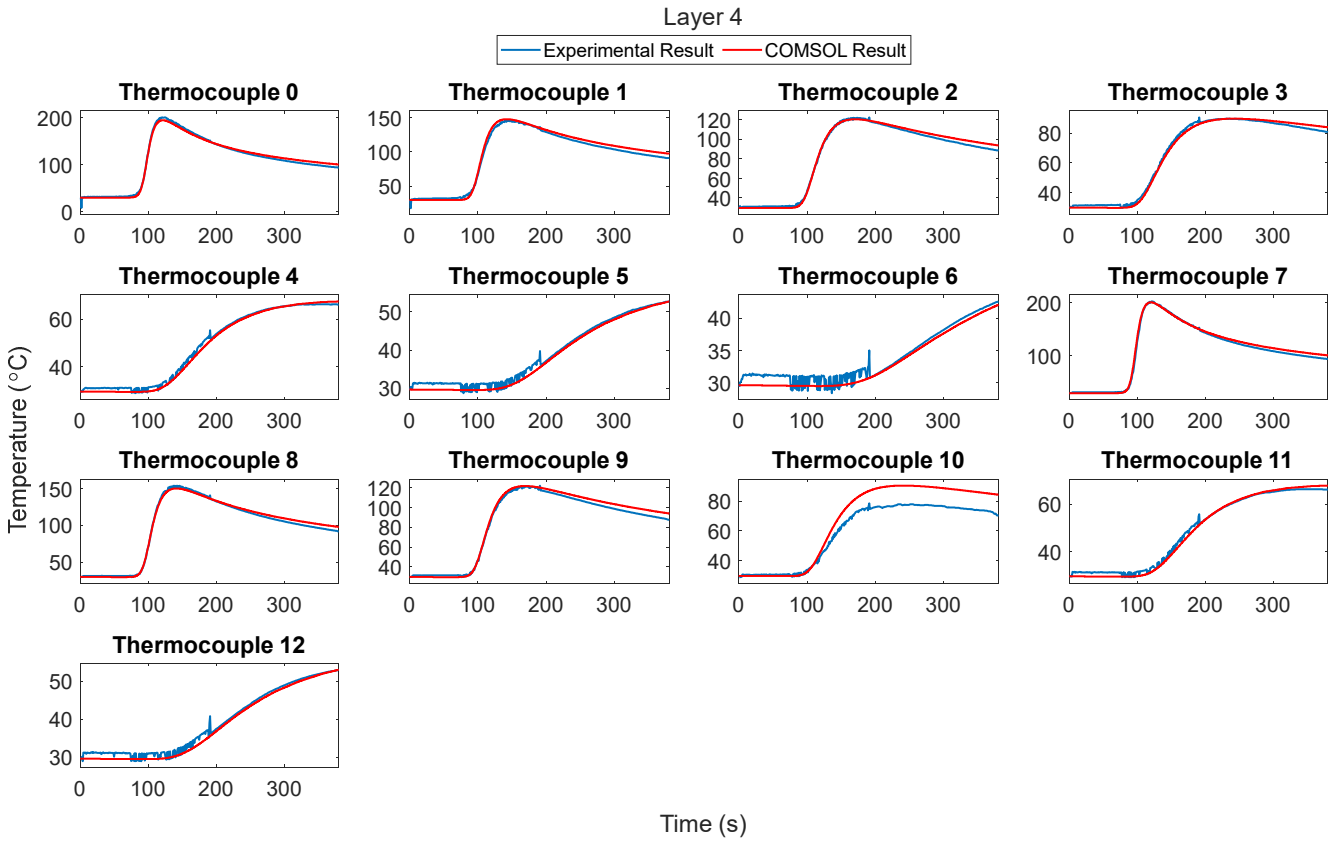

Figure A 2. Comparison of experimental and COMSOL data for layer 4 of welding

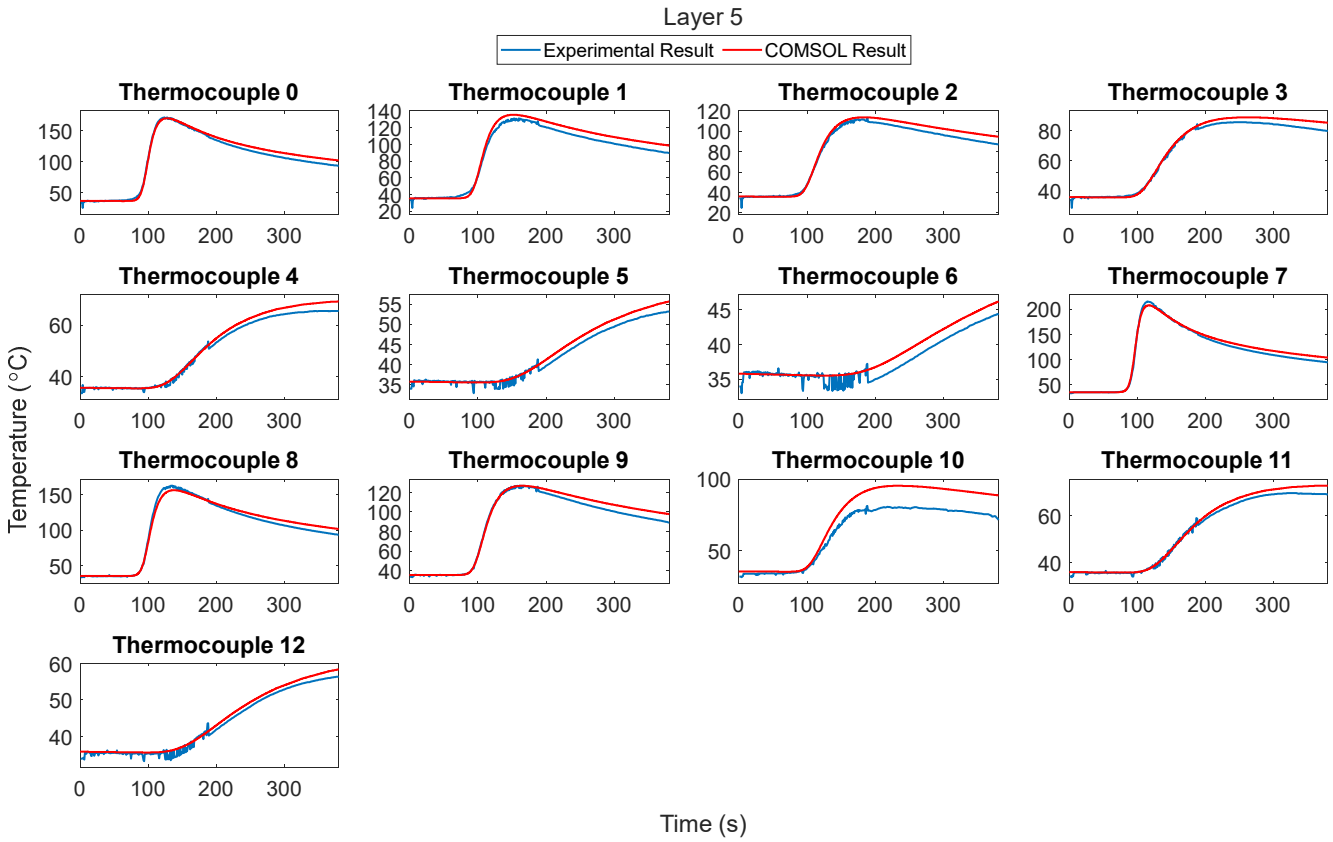

Figure A 3. Comparison of experimental and COMSOL data for layer 5 of welding

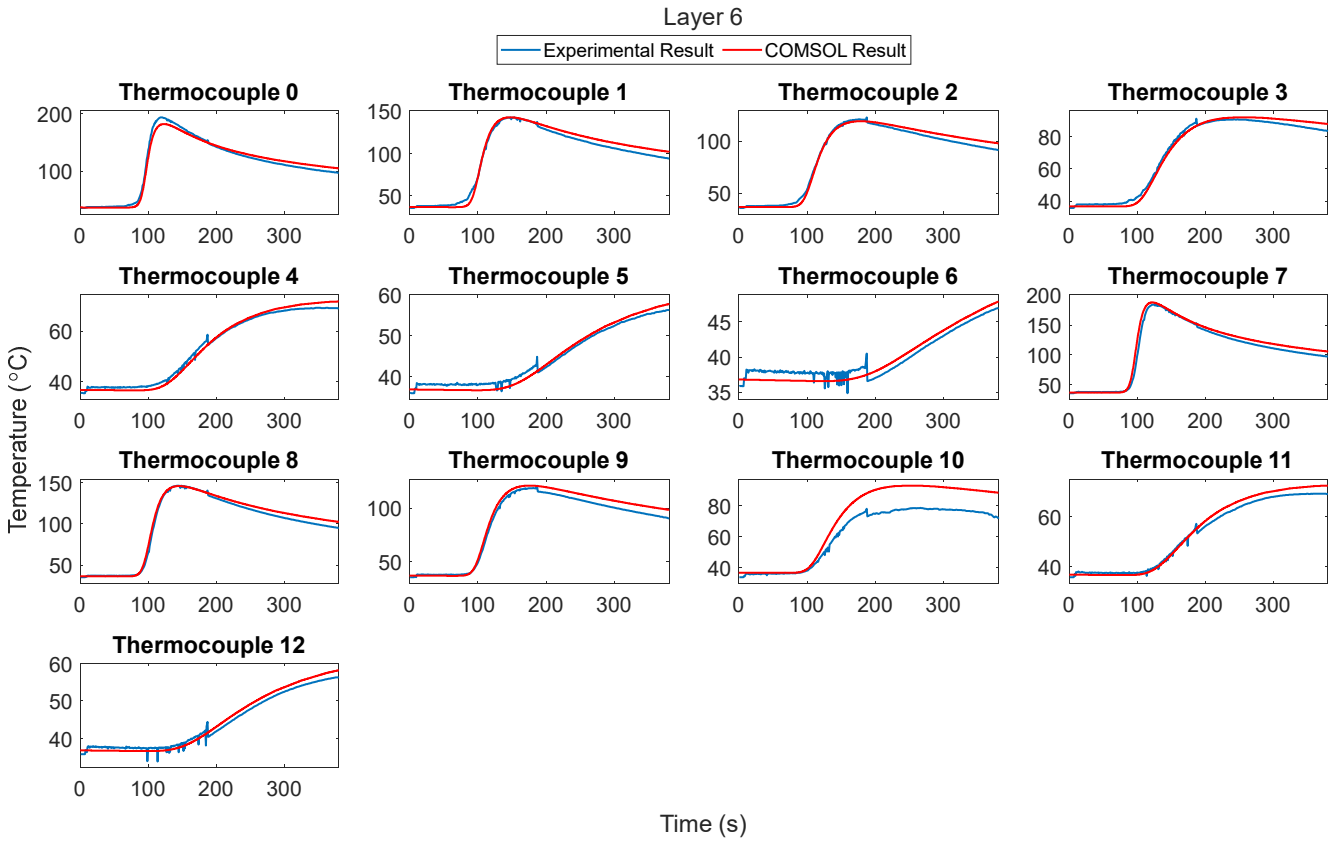

Figure A 4. Comparison of experimental and COMSOL data for layer 6 of welding

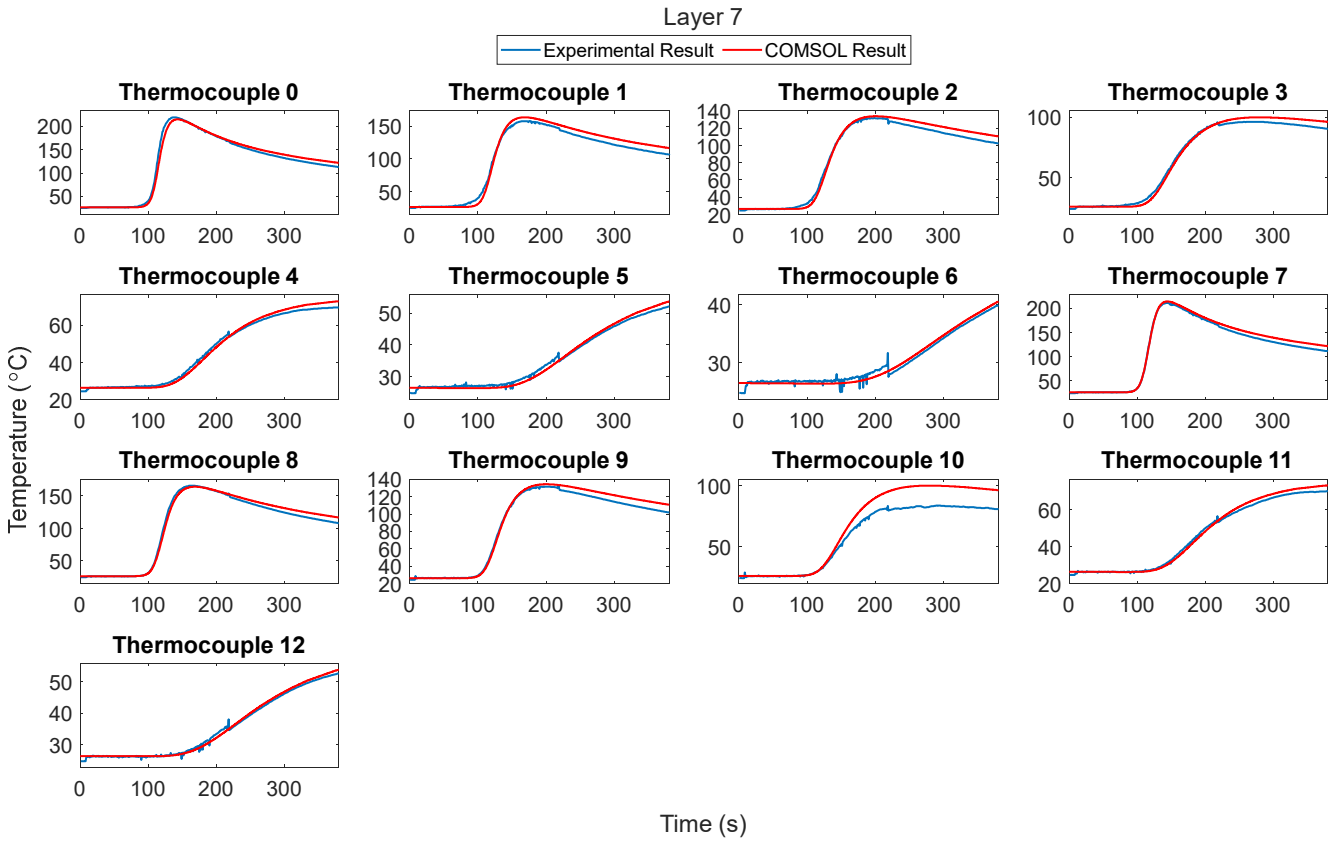

Figure A 5. Comparison of experimental and COMSOL data for layer 7 of welding

Table A 1. Error analysis - layer 3 of welding

Thermocouple Number	Maximum Absolute Error (°C)	Average Absolute Error (°C)	Maximum % Error	Average % Error
0	14.70	4.57	17.71	4.36
1	5.80	1.76	15.47	2.90
2	6.89	2.14	9.50	2.88
3	7.00	2.26	8.60	3.66
4	5.21	1.45	10.00	3.29
5	3.22	0.93	8.70	2.75
6	2.42	0.61	7.52	2.06
7	12.68	2.69	12.98	2.72
8	8.96	1.82	11.50	2.06
9	4.44	2.16	6.91	2.50
11	2.59	0.79	5.40	1.95
12	3.37	0.60	8.43	1.87

Table A 2. Error analysis - layer 4 of welding

Thermocouple Number	Maximum Absolute Error (°C)	Average Absolute Error (°C)	Maximum % Error	Average % Error
0	22.41	3.59	16.54	5.21
1	12.09	3.22	17.14	4.71
2	3.70	1.76	10.75	2.91
3	4.75	1.44	7.63	3.06
4	4.83	1.21	8.71	3.14
5	4.44	1.14	11.18	3.38
6	4.31	0.95	12.31	2.99
7	5.89	2.42	7.54	2.99
8	5.53	2.36	6.27	3.00
9	4.86	2.22	6.47	3.26
11	4.81	1.14	8.62	3.10
12	5.37	1.13	13.16	3.31

Table A 3. Error analysis - layer 5 of welding

Thermocouple Number	Maximum Absolute Error (°C)	Average Absolute Error (°C)	Maximum % Error	Average % Error
0	11.63	3.96	12.52	3.95
1	11.63	4.84	12.39	5.06
2	11.39	2.86	6.67	3.18
3	7.23	1.54	4.81	2.14
4	2.45	0.95	4.79	1.76
5	2.65	0.85	8.06	2.06
6	2.78	0.90	6.86	2.45
7	10.42	3.90	7.70	3.08
8	12.13	3.56	10.28	3.16
9	7.00	2.72	6.96	2.78
11	2.76	0.94	5.43	1.67
12	2.59	0.82	7.74	1.98

Table A 4. Error analysis - layer 6 of welding

Thermocouple Number	Maximum Absolute Error (°C)	Average Absolute Error (°C)	Maximum % Error	Average % Error
0	21.79	5.22	19.28	4.98
1	11.97	3.54	22.01	4.59
2	6.18	2.59	13.38	3.54
3	4.72	1.87	9.18	3.27
4	4.43	1.16	7.55	2.59
5	3.63	1.09	8.10	2.72
6	3.03	1.02	7.50	2.67
7	20.86	4.38	21.01	4.13
8	6.47	2.25	9.76	2.44
9	6.59	3.28	6.56	3.65
11	3.07	1.37	6.36	2.68
12	3.09	1.02	8.24	2.47

Table A 5. Error analysis - layer 7of welding

Thermocouple Number	Maximum Absolute Error (°C)	Average Absolute Error (°C)	Maximum % Error	Average % Error
0	14.74	2.67	9.57	2.46
1	9.71	5.02	21.56	5.81
2	7.75	2.81	13.43	3.70
3	4.11	1.55	9.08	2.87
4	2.15	1.01	7.79	2.49
5	2.54	0.80	6.78	2.58
6	3.14	0.61	9.94	2.20
7	9.73	4.23	8.49	3.29
8	12.22	3.22	13.39	3.21
9	7.63	2.99	9.30	3.34
11	2.91	1.06	6.66	2.40
12	3.25	0.48	8.55	1.52